

# **TRANSACTIONS OF THE INSTITUTE OF AVIATION**

No. 218/2011

**ROTORCRAFT FLIGHT TESTS**

**ROTORCRAFT AERODYNAMICS**

**ROTORCRAFT ARMOUR**

**ROTOR DYNAMICS AND AERODYNAMICS**

**COMPOSITE ROTOR ELEMENTS**

**ROTOR VIBRATION TESTS**

**GYROPLANE AERODYNAMICS**

*Institute of Aviation Editorial Board: Maciej Bossak, Zdobysław Goraj, Marian Jeż,  
Agata Urbanowska (board secretary), Antoni Niepokólczycki, Wojciech Potkański,  
Kazimierz Szumański (chairman), Piotr Wolański, Zbigniew Wołęjsza*

# **PRACE INSTYTUTU LOTNICTWA**

Nr 218/2011

**BADANIA W LOCIE WIROPLATÓW**

**AERODYNAMIKA WIROPLATÓW**

**OPANCERZENIE WIROPLATÓW**

**DYNAMIKA I AERODYNAMIKA WIRNIKA**

**KOMPOZYTOWE ELEMENTY WIRNIKA**

**PRÓBY REZONANSOWE WIRNIKÓW**

**AERODYNAMIKA WIATRAKOWCA**

Publisher: Institute of Aviation Scientific Publications

Al. Krakowska 110/114, 02-256 Warsaw, Poland

tel.: (4822) 846 00 11 ext. 391, fax: (4822) 846 44 32

Edition, revision and computer layout: Agata Urbanowska MA

Printers: ALKOR, ul. Krucza 4, 05-070 Sulejowek

# CONTENTS

<b>E. CHOŁOŻYŃSKI:</b> IMPLEMENTATION OF FLIGHT TESTS IN ORDER TO DEVELOP NEW FLIGHT TECHNIQUES FOR TAKEOFFS AND LANDING IN A LIMITED SPACE FOR HELICOPTER W-3A SOKOL .....	5
<b>A. DZIUBIŃSKI, K. GRZEGORCZYK:</b> STUDY OF THE INFLUENCE OF HELICOPTER'S EXTERNAL COMPONENTS ON THE AERODYNAMIC CHARACTERISTICS .....	11
<b>A. DZIUBIŃSKI, K. GRZEGORCZYK, J. ŻÓŁTAK:</b> CFD ANALYSIS OF EXTERNAL ARMOUR INFLUENCE ON A HELICOPTER AERODYNAMIC CHARACTERISTICS.....	20
<b>F. GEORGIADES, J. WARMIŃSKI:</b> EXCITATION OF A LOCALIZED NONLINEAR NORMAL MODE OF A BLADED DISC ASSEMBLY LUMP MASS NONLINEAR MODEL.....	28
<b>F. GEORGIADES, J. LATALSKI, J. WARMIŃSKI:</b> MODE SHAPES VARIATION OF A COMPOSITE BEAM WITH PIEZOELECTRIC PATCHES .....	36
<b>E. MANOACH, A. MITURA, S. SAMBORSKI, J. WARMIŃSKI:</b> VIBRATION AND DAMAGE DETECTIONS OF COMPOSITE BEAMS WITH DEFECTS.....	44
<b>M. MILLER:</b> ROTOR BLADE SEGMENT WITH PIEZOACTUATED TRAILING-EDGE FLAP FOR DYNAMIC PRESSURE MEASUREMENTS .....	54
<b>M. MILLER, W. STALEWSKI:</b> THE NUMERICAL ANALYSIS OF PROPERTIES OF THE TRAILING-EDGE FLAP ON THE ILH412M-S ROTOR BLADE AIRFOIL .....	63
<b>M. PARAFINIAK, P. SKALSKI:</b> VIBRATION TESTING OF A HELICOPTER MAIN ROTOR COMPOSITE BLADE .....	72
<b>W, STALEWSKI, J. SZNAJDER:</b> POSSIBILITIES OF IMPROVEMENT OF DIRECTIONAL CONTROL EFFECTIVENESS OF LIGHT GYROPLANE AT HIGH-ANGLE-OF-ATTACK FLIGHT CONDITIONS.....	77
<b>J. SZNAJDER:</b> EFFECTIVENESS OF AN INVERTED-V-SHAPED CONTROL SURFACES OF A GYROPLANE AT LOW SPEED AND HIGH-ANGLES-OF-ATTACK.....	86



## IMPLEMENTATION OF FLIGHT TESTS IN ORDER TO DEVELOP NEW FLIGHT TECHNIQUES FOR TAKEOFFS AND LANDINGS IN A LIMITED SPACE FOR HELICOPTER W-3A SOKOL

ERWIN CHOŁOŻYŃSKI

*Flight Line Agusta Westland - PZL Świdnik*

### Summary

*Gradually increasing group of users the W-3A helicopter and a rapid increase in the use of helicopters in urban areas with limited space for takeoffs and landings requires from helicopter manufacturers to develop new piloting techniques which ensure the complete safety of flight.*

*Confirmation of the feasibility of new techniques for takeoffs and landings in the limited space on the helicopter W-3A was carried out during the flight tests which are made by PZL Flight Test Division in the framework of a research project conducted by the Institute of Aviation*

*During the trial carried out:*

- *Assess the size range of a vortex ring and the maneuverability of a helicopter in this state*
- *Minimize the danger area of H-V*
- *Determine the possibility OEI flight*
- *Determine the minimum space for takeoffs and landings, depending on the weight of the helicopter and height of surrounding obstacles*

*This presentation shows how flight tests were conducted since the preparation of a helicopter to trials, through their implementation, and ending on the development of procedures for takeoffs and landings to the Flight Manual and their verification by representatives of the EASA.*

### INTRODUCTION

Gradually increasing user group of W-3A helicopters, and a sharp increase in the use of helicopters in urban areas and in areas with limited space requires from manufacturers to develop new flight techniques for helicopters with ensuring complete safety of flight during takeoff and landing.

W-3A is a twin-engine helicopter, which has the ability to take off and landing in category A, it means that after the failure of one of the engines is ensured continuation of the climbing with OEI (one engine inoperative) flight or landing is possible. Flight technique in the category A helicopter W-3A Sokół did not provide so far the possibility of taking off and landing helicopter where the airfield has a small size (confined heliport) or space is limited by obstacles (restricted helipad).

Knowing the aerodynamic performance and capabilities of W-3A, Flight Test Division performed tests, which aimed to develop such a takeoff and landing techniques that would allow the conduct of air operations from smaller airfields, as well as those which are surrounded by obstacles (eg buildings, trees), and all this with the provision of flight safety and in accordance with the regulations FAR 29 and CS 29.

Tests were conducted in the framework of a research project conducted by the Institute of Aviation. This paper presents the way in which flight tests conducted since the helicopter prepare for trials, through their implementation, and ending on the development of procedures for takeoffs and landings to the Flight Manual and their verification by representatives of EASA.

## 1. PREPARING THE HELICOPTER

Before performing the test W-3A helicopter was equipped with elected in accordance with Test Program set of sensors to enable with the measuring equipment ACRA KAM 500 registration important parameters for the test. The GPS system was built with the antenna on a sampling frequency of 5Hz to the precise trajectory and recording the position of the helicopter over the ground. To determine the zero velocity relative to ambient air, the helicopter was equipped with a special indicator before the windshield.



Figure 1. Measuring equipment ACRA KAM-500



Figure 2. A special indicator mounted in front of the windshield used to maintain near-zero velocity relative to the ambient air

## 2. THE STUDY VORTEX RING

New techniques for takeoffs and landings based on the low speed flight and descending close to vertical so in conditions conducive to vortex ring formation. So important was to learn the range of a vortex ring and the possibility of controlling Sokol helicopter in the state. Attempts to study the phenomenon of ring spinning were carried out at a safe height  $H = 1000\text{m}$  with the weight of the helicopter  $G = 5800\text{kg}$  at speed 30, 20kts and hovering for ever increasing rate of descent. Based on tests carried out found that the speed of 15 to 20kts and descending about  $-6\text{m/s}$  are only increased levels of vibration on the helicopter without deterioration maneuverability, while for the velocity close to zero (10 to  $-5\text{ km/h}$ ) and descending from  $w = -4\text{m/s}$  vortex ring phenomenon was observed but it was easy to leave it through the increasing speed of the helicopter.

## 3. MINIMIZING THE H-V ZONES

Another point is necessary to develop new techniques was to minimize the H-V area after failure of one of the engines. The test was carried out for different weights helicopter for selected points from the previous zone of HV including hover. Based on the results of the tests found that it is possible to a safe landing after engine failure at any hovering height of helicopter with a weight  $G = 5800\text{kg}$ , even after taking 1-second pilot response delay.

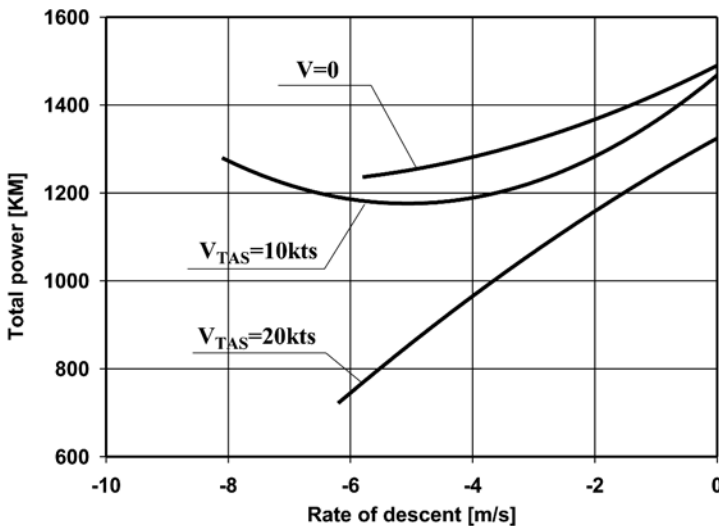


Figure 3. Require power

## 4. PERFORMANCE WITH OEI

Also carried out an attempt to determine OEI performances with speed at which the helicopter reaches a positive rate of climb ( $+0.5\text{ m/s}$ ), it is approximately  $V_{TAS} = 20\text{kts}$ . And for the best climb speed =  $60\text{kts } V_{TAS}$ , the OEI climb with extraordinary power and weight of  $5800\text{kg}$  is  $w = 4.5\text{ m/s}$ .

Due to the limitations of the speed indicator in the very low speeds, as a safe speed during take-off (VTOSS) adopted  $V_{TOSS} = 30\text{kts}$  for which rate of climb was  $2.5\text{ m/s}$ .

## 5. DETERMINATION OF THE MINIMUM SPACE FOR TAKEOFFS AND LANDINGS

The purpose for which it sought in these tests was to develop such technology take-off and landings, which will minimize the space needed to start using the full capabilities of W-3A Sokol. The study was carried out so that the techniques developed takeoffs and landings ensure flight safety at any point on the trajectory of the flight and were in line at the same time the requirements of the aviation regulations. The first stage of testing was to check the possibility of rejected take-off and continued take-off at a safe height ( $H = 1000\text{m}$ ). Profile startup look like that of a fixed hovering (based on the fixed rate before the pilot's window) the pilot began the climbing with a slight movement to the rear. In a fixed climbing co pilot flight caused engine failure by moving power lever in the ground position. Pilot after seeing the failure tried to keep the rotor speed  $NR = 95\%$ , while acceleration began. During these tests initially estimated the loss of height after engine failure. The loss of height depends on the state in which the failure occurs, if a failure occurs during back flight, loss is almost twice higher than during acceleration helicopter.

This is due to the time required to change the angle of inclination of the helicopter to fly forward. The next stage of trials already close the ground was to test emergency procedures at take-off. Faults were simulated on a normal pre-launch trajectory during vertical ascent and the climb with vertical displacement to the rear as well as during acceleration just behind the TDP point.

Figures 4 and 5 shows examples of trajectories of flight after an engine failure during rejected take-off and continued take-off.

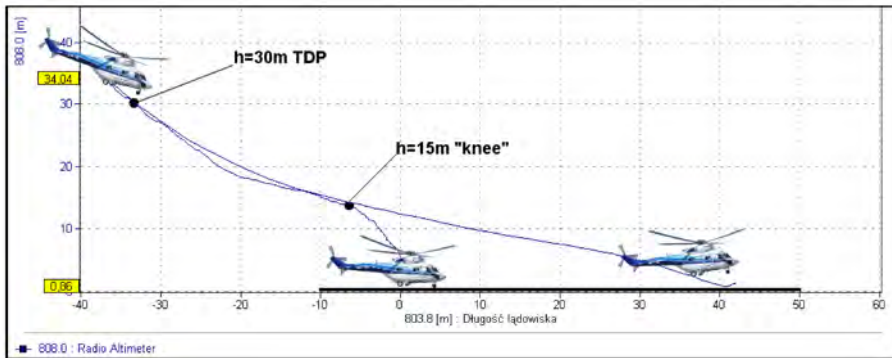


Figure 4. Rejected take off trajectory, engine failure at the height of the TDP point

After many starts with an imitation of an engine failure with different helicopter weights and on the assumption that the landing site is surrounded by obstacles to 15m, a vertical take-off technique was developed by the following procedure:

- 1) hovering 1-2m,
- 2) vertical climb for  $h = 15\text{m}$  with ROC 1-2m/s,
- 3) the "knee" or start reversing the ascent up to the TDP,
- 4) after reaching TDP helicopter acceleration to  $V_{IAS} = 70\text{kts}$  using take-off power fuselage inclination about 10 deg,
- 5) steady climbing with maximum continuous power and airspeed  $V_Y = 70\text{kts}$ .

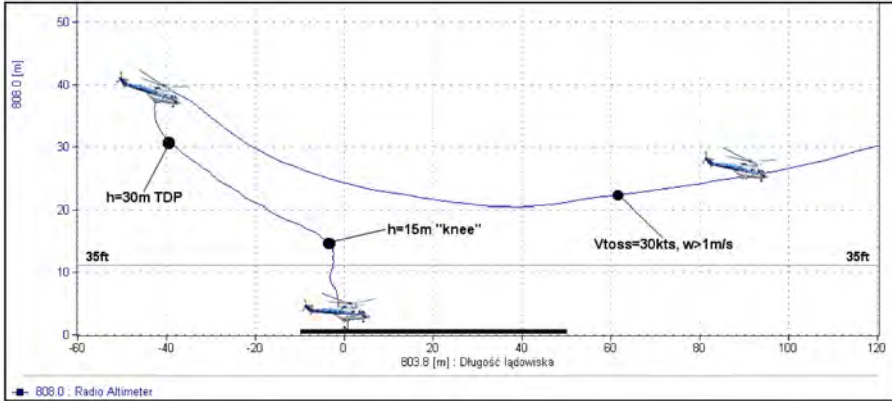


Figure 5. Continued take off, engine failure just behind the TDP point

By analyzing the records of the trials also identified the minimum landing sizes needed to perform such operations.

The last step was to develop techniques for landing. Similarly as for the predicted trajectory starts at a normal landing, initiated one of the engine failure before and after the point LDP. If the failure occurred before the LDP point, pilot interrupting the landing and began climbing with 2.5 OEI power (balked landing). If the failure occurred for the LDP pilot continued the landing single-engine (continued landing).

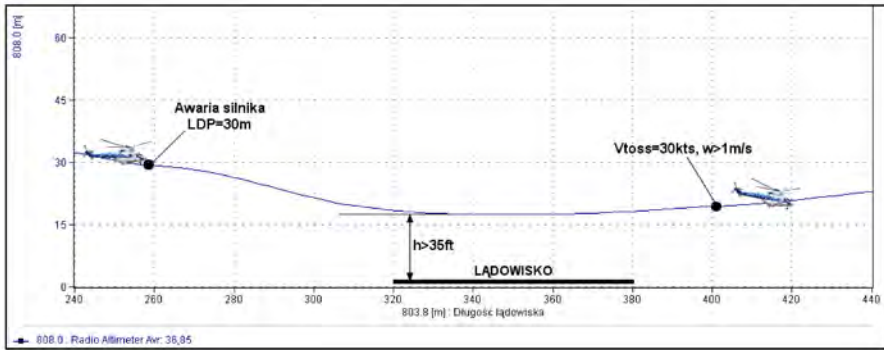


Figure 6. Balked landing trajectory, engine failure before LDP

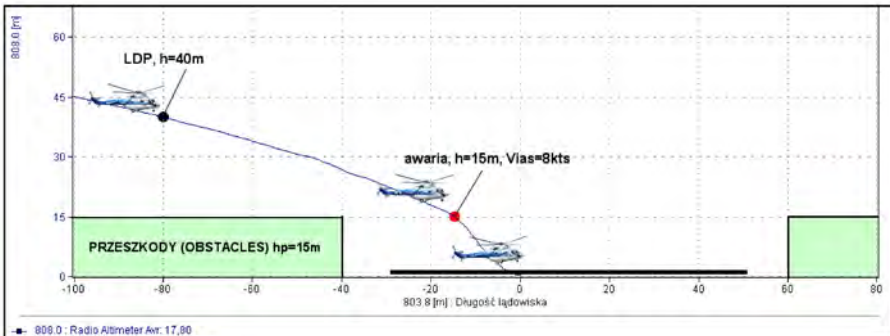


Figure 7. Continued landing trajectory, engine failure at 15m, airfield surrounded by 15m height obstacles

On the basis of completed balked and continued landings the piloting technique was developed according to the following procedure:

- 1) steady descending with airspeed  $V_{IAS} = 30\text{kts}$  and rate of descent  $2-3\text{m/s}$ ,
- 2) from  $50-40\text{m}$  should start braking so that the beginning of the landing at a height  $h = 15\text{m}$  have about  $15\text{kts}$  ground speed,
- 3) go the steep descent to touchdown.

The resulting new take-off and landing techniques have been verified in flight and accepted by representatives of EASA, confirming compliance with FAR29 and CS29 regulations.

ERWIN CHOŁOŻYŃSKI

## **REALIZACJA PRÓB W LOCIE W CELU OPRACOWANIA NOWYCH TECHNIK STARTÓW I LĄDOWAŃ W OGRANICZONEJ PRZESTRZENI NA ŚMIGŁOWCU W-3A SOKÓŁ**

### Streszczenie

*Sukcesywnie zwiększająca się grupa użytkowników śmigłowca W-3A oraz gwałtowny wzrost wykorzystania śmigłowców w aglomeracjach miejskich jak i w obszarach o ograniczonej przestrzeni do startów i lądowań wymaga od producentów śmigłowców wypracowania nowych technik z zapewnieniem pełnego bezpieczeństwa lotu.*

*Potwierdzenie możliwości wykonania nowych technik startów i lądowań w ograniczonej przestrzeni na śmigłowcu W-3A przeprowadzono podczas prób w locie, które wykonał Wydział Prób w Locie*

*PZL Świdnik w ramach projektu badawczego prowadzonego przez Instytut Lotnictwa.*

*Podczas prób należało:*

- *Ocenić wielkość strefy występowania pierścienia wirowego oraz możliwości pilotażowe śmigłowca w tym stanie*
- *Zminimalizować strefy H-V*
- *Określić możliwość wznoszenia w locie jednosilnikowym*
- *Określić minimalną przestrzeń do startów i lądowań w zależności od ciężaru śmigłowca jak i wysokości otaczających przeszkód*

*Niniejszy referat przedstawia sposób w jaki przeprowadzono próby w locie od momentu przygotowania śmigłowca do prób, poprzez ich realizację, a kończąc na wypracowaniu procedur startów i lądowań do Instrukcji Użytkowania w Locie i ich weryfikacji przez przedstawicieli EASA.*

## STUDY OF THE INFLUENCE OF HELICOPTER'S EXTERNAL COMPONENTS ON THE AERODYNAMIC CHARACTERISTICS

ADAM DZIUBIŃSKI, KATARZYNA GRZEGORCZYK

*Institut Lotnictwa*

### Summary

*The paper presents a numerical analysis of flow around a helicopter in various configurations. All the configurations were simulated using FLUENT, Computational Fluid Dynamics code. The calculations were based on a three-dimensional, steady-state solver. The results have been obtained for the rotorcraft operating in forward flight with selected angles of attack ( $\alpha$ ). The main goal of this work was to calculate the steady aerodynamic characteristics of the helicopter and research on the effects of components on the aerodynamic characteristics.*

### INTRODUCTION

Modern helicopters need to be designed to perform multiple tasks. One of the methods of extending the range of their application is adding external components to the hull [2]. This is the reason of using additional components i.e. cameras (Figure 1), bays (Figure 2), wings and pylons (Figure 3). All external elements of a helicopter affect the total aerodynamic properties.



Figure 1 Examples of external components on the modern helicopters (camera) (c) Adam Dziubiński



Figure 2 Examples of external components on the modern helicopters (bays) (c) Adam Dziubiński



Figure 3 Example of external components on the modern helicopters (wings, pylons, tanks) (c) Adam Dziubiński

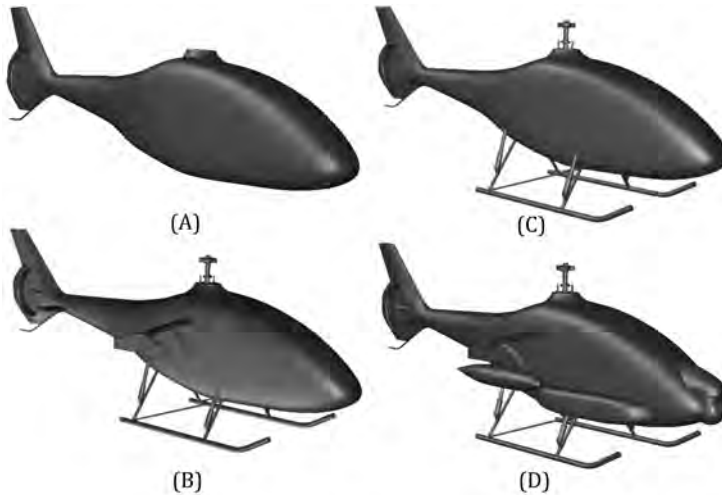


Figure 4 Geometry of helicopter configurations tested

This paper contains the simulation results the influence of selected external components. Four configurations were tested – Figure 4:

- (A) base consisting of fuselage, tail boom, tail skid, tail fin equipped with ducted fan,
- (B) configuration A with added landing gear, elevator, tail rotor gearbox, simplified main rotor head,
- (C) configuration B with added wings and pylons,
- (D) configuration C with added bays, fuel tanks and camera.

The aerodynamic properties strongly depend on the geometric parameters of the rotorcraft as well as flight conditions. Components of the configuration have an effect on the aerodynamic characteristics and performance. Size and shape of each part influences on flow field around the helicopter.

This study contains a numerical simulation of the flow around the light helicopter. All analyses have been done using CFD software (Fluent code). The calculations have been performed for the rotorcraft operating in forward flight with various angles of attack  $\alpha$ . The computational results of the flow field around the helicopter were used to determinate the performance characteristics of the examined configuration. This allowed an estimate influence additional configuration items on changes the aerodynamic characteristics of helicopter.

## NUMERICAL TESTS CONDITIONS

The numerical calculations are based on FLUENT software, part of ANSYS CFD package [6], widely recognized as industry standard. This numerical algorithm uses the finite-volume method. In present paper the fluid was simulated as an incompressible with the Spalart-Allmaras turbulence model. Geometric model was created using CATIA. All model's geometry modifications and computational grids have been made using ICFM CFD code [5]. The cubical domain was generated with the unstructured grid consisted of tetrahedral cells. Boundary layer mesh has been created as several layers of prisms. In Figure 5 grid around a helicopter (version (B)/gear) is illustrated and three-dimensional domain is presented in Figure 6.

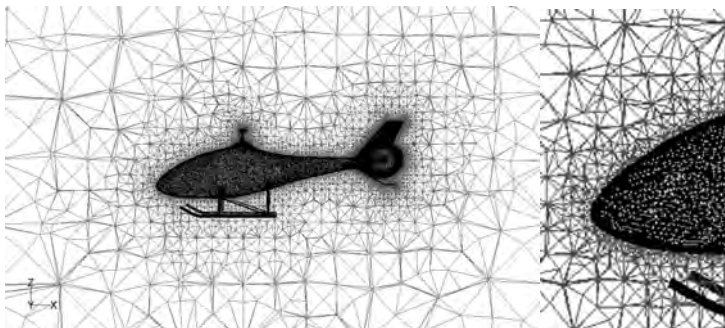


Figure 5 Mesh around the basic version helicopter (left) and around the fuselage nose (right)

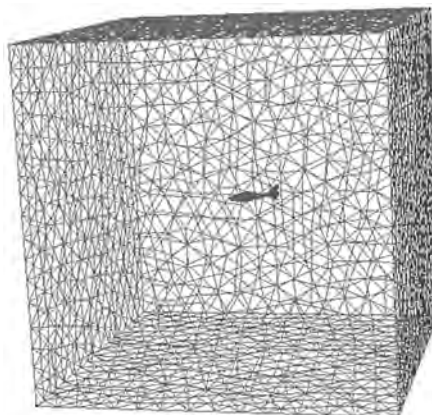


Figure 6 Computational domain meshed with tetrahedral elements

Information about total mesh's sizes is shown in Table 1.

Table 1 Mesh size for various helicopter configurations

Configuration	Number of cells
(A)/base	1 310 996
(B)/gear	2 824 811
(C)/wings	3 572 210
(D)/stores	4 361 478

All configurations were tested for the various angles of attack. Results of research are presented in XYZ coordinate system (related with direction of undisturbed flow) – Figure 7.

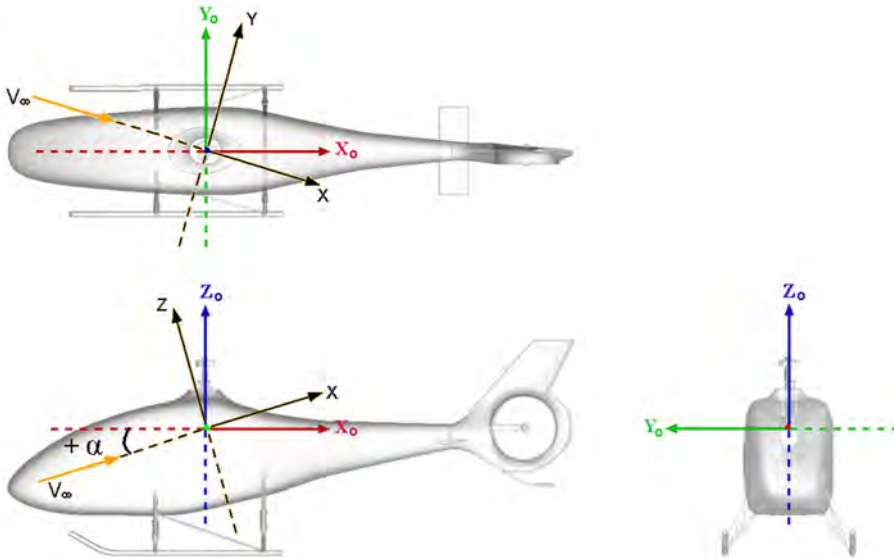


Figure 7 Coordinate systems used in calculation: XYZ – the flow coordinate system,  $X_0Y_0Z_0$  – the local coordinate system

All calculations were done for forward flight.

Aerodynamic coefficients are referenced to:

- main rotor diameter  $D$  as linear characteristic dimension to calculate moment coefficient,
- rotor surface  $S = \pi \cdot R^2$  as surface characteristic value.

## RESULTS

Computational method allows obtaining information hardly available with experimental methods. Among other things, information about load distribution on the specified surfaces of a model and the flow field structure around model is available.

At the outset, sample images of flow field and pathlines around a helicopter are presented using visualization tools that are offered by FLUENT software. The flow around the basic version of the helicopter in forward flight is shown in Figure 8. The separation at the back of main

rotor hub and reattachment of flow at sidewalls of fuselage are clearly visible. Influence of external stores (wings, pylons, bays, tanks and camera) on the flow around helicopter is presented in Figure 9.

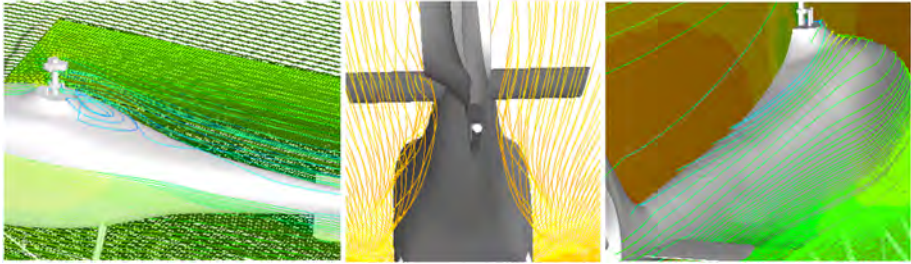


Figure 8 Visualization of pathlines around the (B) configuration of helicopter in forward flight

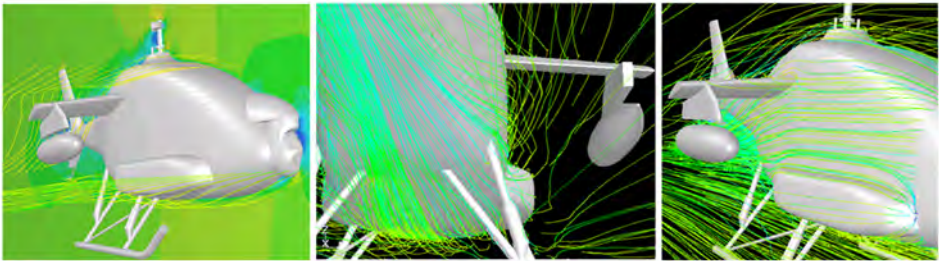


Figure 9 Visualization of pathlines around the (D) configuration of helicopter in forward flight

Basing on the result of flowfield analysis, forces and moments values were calculated for all configurations. In the graph below (Figure 10.) and Table 2 the comparison total drag for various versions of the helicopter operating in forward flight for three selected angles of attack ( $\alpha = -10^\circ, 0^\circ, 10^\circ$ ) are presented.

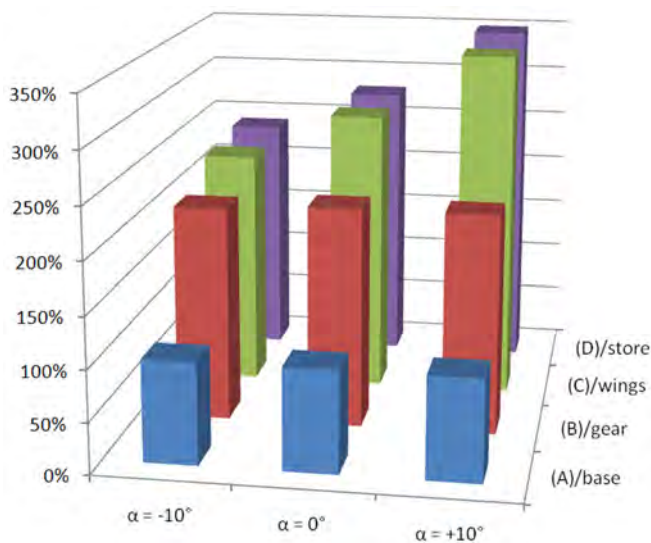


Figure 10 Comparison of tested configuration drag for three selected angle of attack

Table 2 Comparison of configuration tested drag for three selected angle of attack

Configuration	$\alpha = -10^\circ$	$\alpha = 0^\circ$	$\alpha = +10^\circ$
(A)/base	100%	100%	100%
(B)/gear	211%	216%	216%
(C)/wings	234%	279%	344%
(D)/store	239%	279%	349%

Analysis of presented data shows, that additional external components are causing an increment of helicopter fuselage drag. The drag for configuration (A)/base and (B)/gear weakly depend on value of angle of attack. For last two configurations: (C)/wings, (D)/stores situation is quite different. Drag increases with increase of angle of attack.

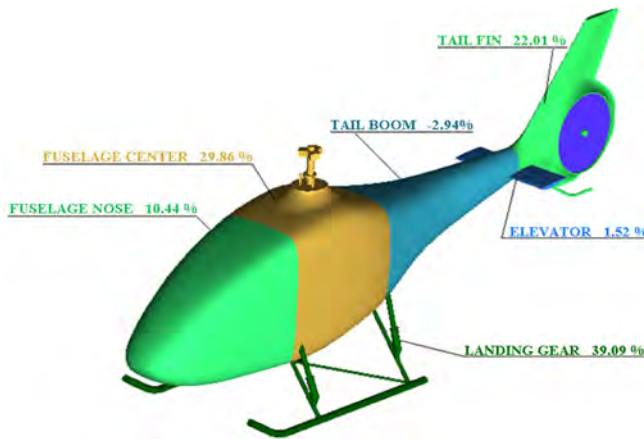


Figure 11 Percentage of particular components of total drag for (B)/gear configuration

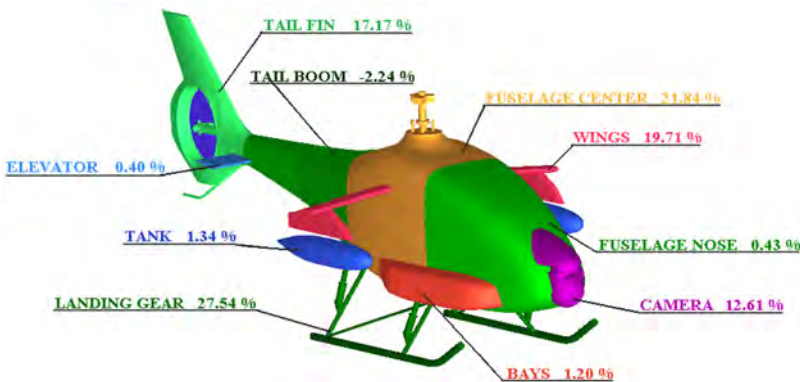


Figure 12 Percentage of particular components of total drag for (D)/stores configuration

For more detailed drag analysis of the computational model and determination of the percentage of particular components in total drag, the computational model is split into several parts as in Figure 11 (configuration (B)/gear) and Figure 12 (configuration (D)/gear). The fol-

lowing images are the simulation results for two versions of helicopter in forward flight condition ( $V=180 \text{ km/h}$ ,  $\alpha=0^\circ$ ). In these figures percentage value of drag generated by each part is presented. It is also collected in Table 3. The landing gear is an element which causes the largest increase in the drag force in both cases. The next elements lead to the increase of drag value, but its influence of the total drag force is less significant.

Table 3 Comparison of percentage of particular components of total drag for configuration (B)/gear and (D)/stores for angle of attack  $\alpha=0^\circ$

Configuration	Tail Fin	Tail Boom	Elevator	Leanding Gear	Fuselage Center	Wings	Tanks	Fuselage Noce	Camera	Bays
(B)/gear	22,01	-2,94	1,52	39,09	29,86	----	----	10,44	----	----
(D)/store	17,17	-2,24	0,40	27,54	21,84	19,71	1,34	4,30	8,79	1,20

The influence of external components is defined as change (D) of the aerodynamic coefficient value for configuration (B), (C) and (D) compared to value of aerodynamic coefficient for configuration (A)

$$DC_k = C_k(Q) - C_k(A),$$

Where indices: Q = B, C, D are symbols of configuration, k=X, Y, Z, mx, my, mz

The results are shown in Figure 13.

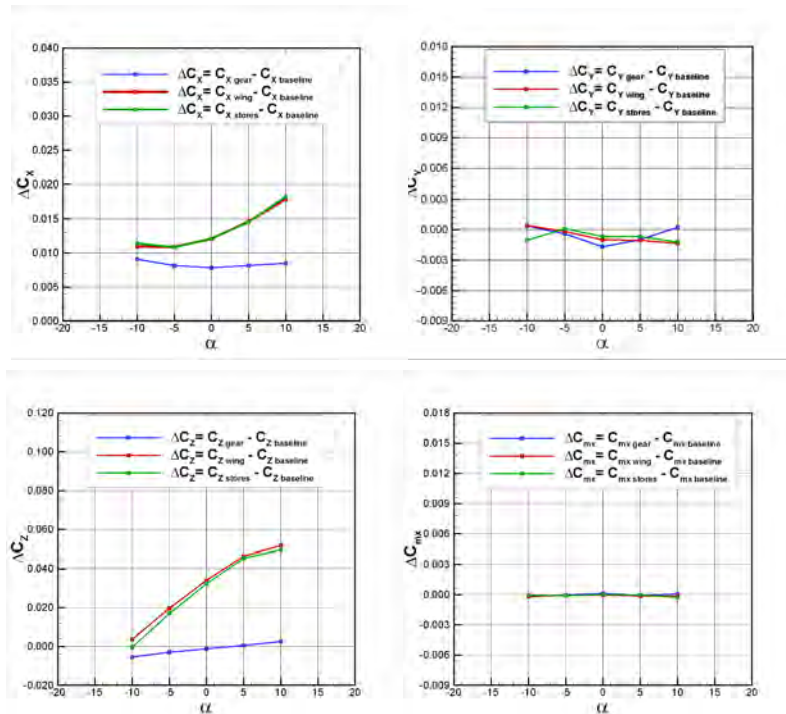


Figure 13 Influence of external components of helicopter on aerodynamic characteristics, configuration (A)/base as reverence

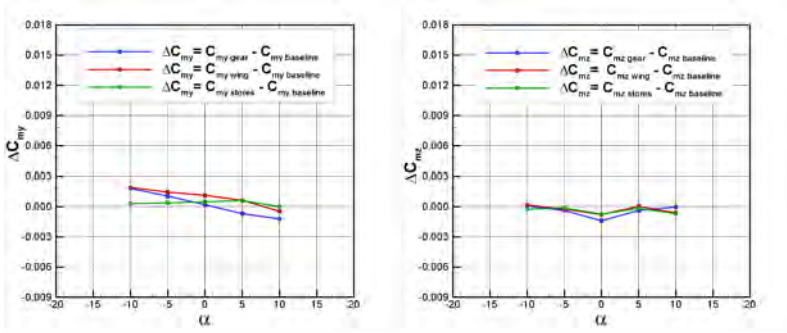


Figure 13 Influence of external components of helicopter on aerodynamic characteristics, configuration (A)/base as reference

The results of conducted calculations showed that in the case of configuration (B) the drag coefficient depends weakly on the angle of attack. However the strong dependence of drag coefficient on the angle of attack was observed in the cases (C) and (D). Values of drag coefficient in both cases (C and D) are similar. In the case of lift coefficient an increase in derivative  $dC_Z/d\alpha$  for all configurations was detected. The highest values of lift coefficient have been obtained for the case C/wing. On the basis of characteristics can be concluded, that in comparison with configuration C/wing adding external stores causes the reduction of lift coefficient. In terms of moment coefficient's changes, it is seen that they all fluctuate around zero value.

## CONCLUSIONS

The research on the influence of selected external components on the steady aerodynamic characteristics of a helicopter was studied. From the analysis of the results, it can be concluded that adding wings to helicopter baseline in forward flight conditions leads to improvement of the lift coefficient. It happens at the expense of aerodynamic drag. On the other hand adding external stores to helicopter baseline with wings practically does not have influence on the aerodynamic characteristics.

## REFERENCES

- [1] CZECHYRA T.: Sprawozdanie nr 2/RA/81/B: Pomiar współczynników aerodynamicznych na modelu kadłuba śmigłowca z nadmuchem wirnika. Warszawa 1981 r.
- [2] GRZEGORCZYK K., BRONOWICZ J.: Projekt aerodynamiczny śmigłowca bezzałogowego o udźwigu 15 kg. / Prace Instytutu Lotnictwa Nr 3-4 (194-195), s.264-271 / Warszawa 2008r.
- [3] GRZEGORCZYK K., DZIUBIŃSKI A., ŻÓŁTAK J.: Instytut Lotnictwa. Sprawozdanie wewnętrzne nr 30/BA-A2/P/10.
- [4] WITKOWSKI R.: Wprowadzenie do wiedzy o śmigłowcach / Biblioteka Naukowa Instytutu Lotnictwa / Warszawa 2003 r.
- [5] ANSYS ICEM CFD 11.0 Tutorial Manual. 2007.
- [6] FLUENT 6.1 User's Guide. Fluent Inc. February 2003.

## ACKNOWLEDGMENTS

This research was supported by project founded by Polish Ministry of Science and Higher Education, Contract no O R00 0048 08

ADAM DZIUBIŃSKI, KATARZYNA GRZEGORCZYK

## **ANALIZA NUMERYCZNA WPŁYWU ZEWNĘTRZNYCH PODWIESZEŃ ŚMIGŁOWCA NA JEGO CHARAKTERYSTYKI AERODYNAMICZNE**

### Streszczenie

*W opracowaniu przedstawiono wyniki obliczeniowej analizy opływu modelu kadłuba śmigłowca w różnych konfiguracjach. Symulacje wykonano wykorzystując metody Obliczeniowej Mechaniki Płynów (CFD). Zaprezentowano rozwiązanie trójwymiarowego zagadnienia stacjonarnego opływu śmigłowca w warunkach lotu z prędkością postępową dla wybranych kątów natarcia. Głównym celem pracy było uzyskanie stacjonarnych charakterystyk aerodynamicznych oraz zbadanie wpływu zewnętrznych podwieszeń śmigłowca na jego charakterystyki aerodynamiczne.*

## CFD ANALYSIS OF EXTERNAL ARMOUR INFLUENCE ON A HELICOPTER AERODYNAMIC CHARACTERISTICS

ADAM DZIUBIŃSKI, KATARZYNA GRZEGORCZYK, JERZY ŻÓŁTAK

*Instytut Lotnictwa*

### Abstract

*The article contains results of the analysis for the influence of external armour on aerodynamic characteristics of a helicopter fuselage. The flowfield for both configurations: with and without armour has been obtained for operational range of angle of attack and sideslip angle, using Fluent software. The results were used to calculate the aerodynamic forces and moments. Finally the influence of armour on aerodynamic characteristics was analysed.*

### INTRODUCTION

Adding an armour to a helicopter demands some compromises. Such armour must provide proper protection level for crew and helicopter components, and has to be as light as possible due to mass requirements. At the same time it is expected, that flight and aerodynamic performance will be saved for the widest possible range of velocities and angles of attack. In some helicopters [2], [3], armour is made as integral element of their fuselage structure.

The others may be armoured optionally. In those cases an armour is mounted as external and/or internal additional elements (shields). In [2] and [3] the concept of armour for large, over 5 700 kg (12 500 lbs) maximum certificated takeoff weight[6], multipurpose helicopter was presented. It based on experience and test methodology recommended in [5] for light armoured vehicles. Report [2] presents also the results of mass analysis for different material used for shields. Part of armour is mounted outside the helicopter fuselage. The external shields change helicopter's aerodynamic characteristics.

The presented paper focuses on the analysis of aerodynamic influence of armour according to presented in [2] concept of armoured helicopter. The study has been done using numerical methods.

The issues will be discussed as follows: modeling the helicopter fuselage with and without armor, preparing meshes and methods used in numerical calculations and setting the test conditions. Finally, selected results will be presented.

## OBJECT OF RESEARCH

The object of research is large (6 000 kg of certified MTOW) multipurpose helicopter [6]. The initial geometry[7] - Figure 2 - contains many details, unnecessary from this specific CFD analysis point of view. Therefore, while preparing the geometry of model used in the calculation, the main rotor and tail rotor have been omitted and shape of landing gear and fuselage have been simplified – Figure 3a. Influence of engine’s inlets and outlets has not been considered – Figure 3b. Other elements, which have influence on drag or lift, has been included in model in simplified form, if necessary. This geometry was used as a base for all external shield surfaces installation. The final geometry of helicopter fuselage, with and without armour, is shown in Figure 4 left and right respectively.



Figure 1. Armour concept for 6-ton take-off weight multipurpose helicopter



Figure 2. Base geometry of 6-ton take-off weight multipurpose helicopter

For both cases mentioned above, the tetrahedral meshes have been created, because of shape complexity. Boundary layer around helicopter shape has been modelled using prism elements, with pyramid elements transition layer. Size of baseline mesh is around 696 000 cells, and armoured - 1 566 702 cells. Mesh density increased in proximity of fuselage, especially on detailed areas with high curvature, as elevator, landing gear and armour edges. The grids were generated using ICEM software [8,1]. In the Figure 5 the mesh densities on surface of helicopter are presented. Volumetric mesh density have been shown using the symmetry plane.

## CFD METHODS

Calculations were done using FLUENT [1,4] code. It allows to analyse the steady and unsteady flowfield around any complex geometry. Motion of fluid is described by the Reynolds Averaged Navier-Stokes equations. The finite volume method is used to obtain numerical solution of these equations. A set of turbulent models is implemented in the software. Several types of boundary conditions can be used.

In the presented analysis following parameters and settings were used:

- 3 dimensional steady calculation
- flux calculation – Semi-Implicit Method for Pressure Linked Equations (SIMPLE)[9]
- turbulent model –Spalart Allmaras [9]
- external boundary condition – on all external faces of domain except the backward one (outlet) a pressure far field boundary condition has been set, at outlet a pressure outlet with equal to farfield pressure has been used,
- at the surfaces of fuselage and armour – a wall boundary condition has been set.

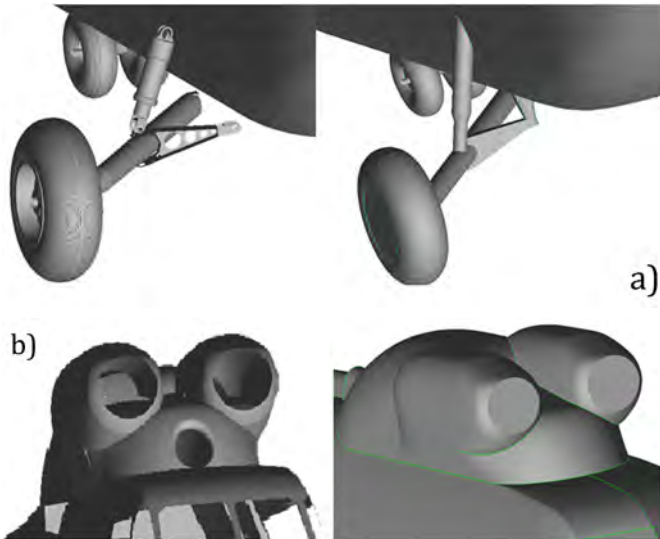


Figure 3. Simplifications on CFD geometry in landing gear and engine nacelles

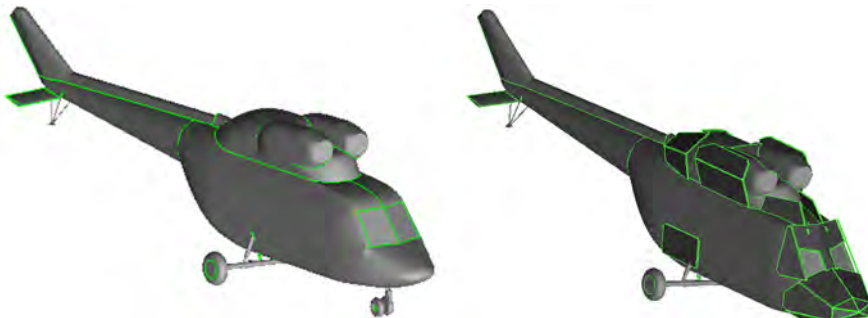


Figure 4. CFD helicopter fuselage geometry without (left) and with armour (right)

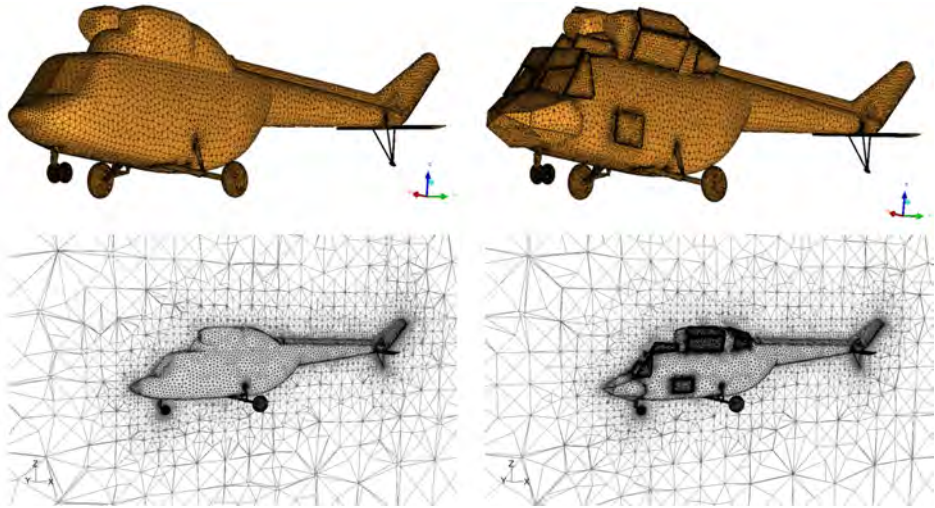


Figure 5. Mesh comparison between baseline (left side) and armoured (right side) versions

## TEST CONDITIONS

Both configurations: without and with armour were tested. The schedule of tests – Table 1 – consisted of one set of calculation scanning angles of attack from  $\alpha = -10^\circ$  to  $16^\circ$ , with assumed sideslip angle  $\beta = 0^\circ$  for both of configurations. Then, for chosen angles of attack set:  $\alpha = -10^\circ, -5^\circ, 0^\circ, 5^\circ, 10^\circ$ , sideslip angle has been also scanned from  $\beta = -10^\circ$  to  $10^\circ$  with step equal  $5^\circ$ . Coordinate system has been chosen in the way, that positive angle of attack corresponded with nose down inclination – Figure 6 – (as in forward flight of helicopter). Positive sideslip was assumed as when nose of helicopter, observed from pilot point of view, moves right. All calculations were done for flight velocity  $V \approx 120$  km/h ( $M = 0.1$ ).

Aerodynamic coefficients are referenced to:

- main rotor radius  $R$  as linear characteristic dimension to calculate moment coefficient,
- rotor surface  $S = \pi \cdot R^2$  as surface characteristic value.

Table 1. Tests schedule

Case	Sideslip angle	Angle of attack $\alpha$ [°]													
		-	-6	-5	-4	-2	0	2	4	5	8	10	12	15	16
Baseline	$\beta$ [°]	10	-6	-5	-4	-2	0	2	4	5	8	10	12	15	16
	-10	X	--	X	--	--	X	--	--	X	--	X	--	--	--
	-5	X	--	X	--	--	X	--	--	X	--	X	--	--	--
	0	X	X	X	X	X	X	X	X	X	X	X	X	X	X
	5	X	--	X	--	--	X	--	--	X	--	X	--	--	--
Armored	-10	X	--	X	--	--	X	--	--	X	--	X	--	--	--
	-5	X	--	X	--	--	X	--	--	X	--	X	--	--	--
	0	X	X	X	X	X	X	X	X	X	X	X	X	X	X
	5	X	--	X	--	--	X	--	--	X	--	X	--	--	--
	10	X	--	X	--	--	X	--	--	X	--	X	--	--	--

## TEST RESULTS

The result of calculation was a flowfield over tested configuration for different combination of angles of attack and sideslip angles. The influence of armour, for angle of attack  $\alpha = 0$  deg. and sideslip angle  $\beta = 0$  deg., on static pressure and wall shear stress distribution on fuselage are presented in Figure 6 and Figure 7, respectively. An area with increased static pressure is clearly visible on flat shields in front of fuselage as well as in proximity of sideway shields of fuselage and those for engine nacelles.

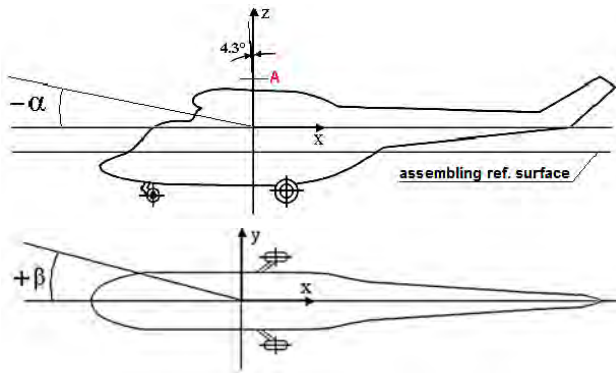


Figure 6. Coordinate system used in calculation

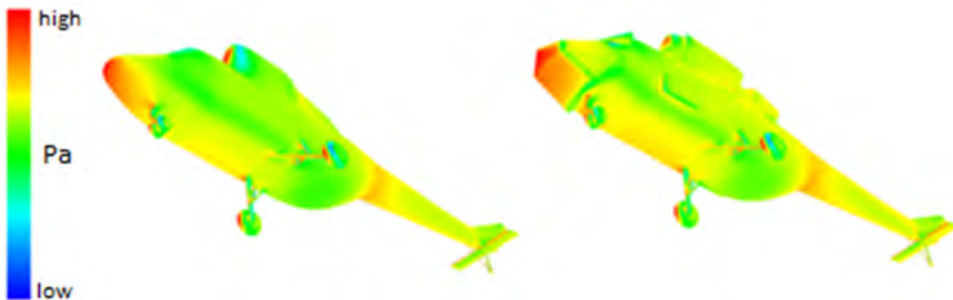


Figure 7. Static pressure distribution for fuselage without (left side) and with (right side) armour at  $\alpha=10^\circ$ ,  $\beta=10^\circ$

Basing on the result of flowfield analysis, forces and moments have been calculated. These data was used in analysis of armour influence on aerodynamic characteristics. First the tendency of changes for case without sideslip angle (symmetric case) was obtained. The influence was defined as change (D) of the aerodynamic coefficient between the configurations of fuselage with and without armour (base):

$$DC_k = C_k(\text{armoured}) - C_k(\text{base}),$$

where index  $k = L, D, M_y$  for lift, drag and pitching moment respectively.

The results are shown in Figure 8. The armour causes increase of lift when nose of a helicopter is pointed upwards, and decrease when nose is downward. This function is roughly linear from  $-4^\circ$  to  $12^\circ$ . Below  $-4^\circ$  the influence does not change as elements of upper armour surfaces are shadowed by cockpit roof, then above 6 deg. the influence increases as increase angle of attack causes influence of, extended with armour, lifting surface of fuselage.

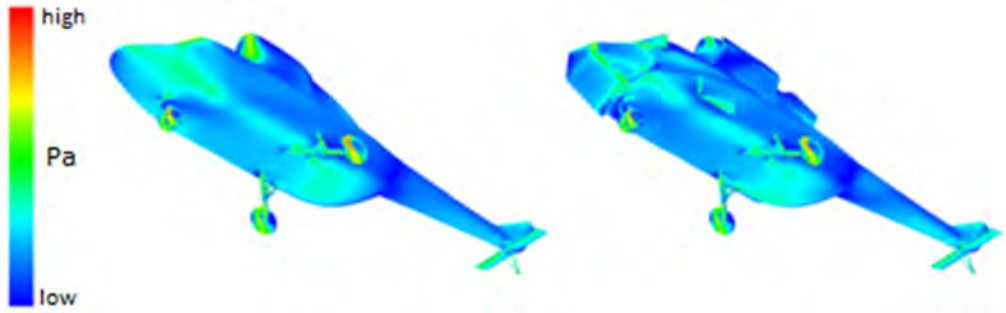


Figure 8. Wall shear stress pressure distribution for fuselage without (left side) and with (right side) armour at  $\alpha=10^\circ$ ,  $\beta=10^\circ$

Drag influence is nonlinear, and changes slowly with maximum near  $-4^\circ$ , at  $-10$  decreases by half and at  $+12$  decreases by 3. The size of influence is one dragpoint, referenced to surface of main rotor. Moment coefficient influence causes decrease of moment and increase of nose down tendency of a helicopter. This tendency is non linearly decreasing as increases the angle of attack (nose moves down).

In next step armour influence on sideslip characteristics at different angles of attack was analysed.

Appears, that armour shields are strongly decreasing drag coefficient with increase of sideslip angle, more than they do with angle of attack change – Figure 9a. This characteristic decreases with negative angle of attack (nose up), as fuselage shadows (aerodynamically) the upper part of armour.

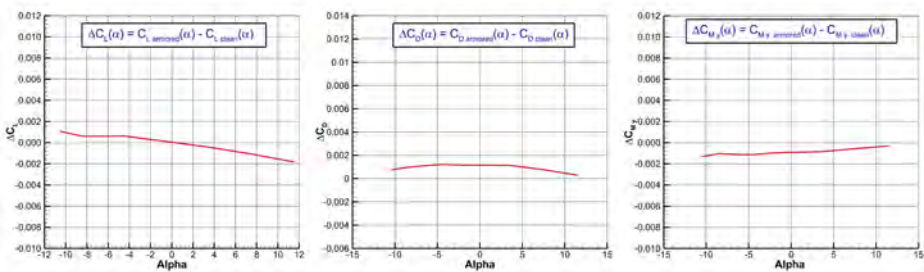


Figure 9. Influence of armour on fuselage lift drag and moment coefficients versus angle of attack

The armour influence on side force or moment coefficient are not significant – Figure 9b,c. Misleading could be a sign change in  $\alpha=-5^\circ$ , but parts of the armour are working as additional lifting surfaces, so this causes such unexpected behaviour. As a main factor of similar characteristics of moment could be front armour, which moves forward the pressure force centre (decreases stability). On the other hand the armour around transmission and engines is also generating such displacement if it is not in aerodynamic shadow of a fuselage, as for positive  $\alpha$ . That's because the influence on yaw moment changes its sign when it comes to angle of attack around  $\alpha=3^\circ$ .

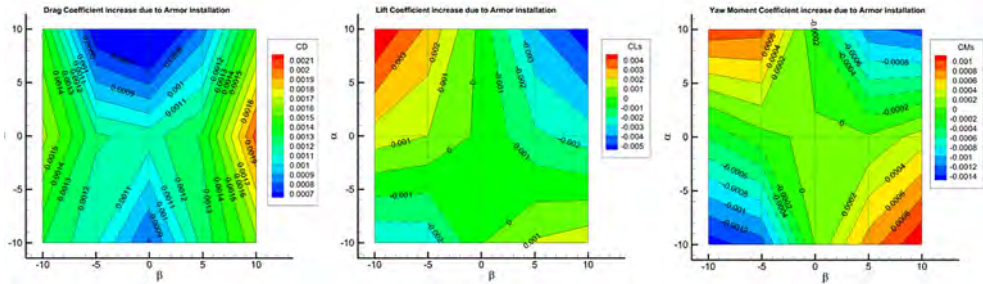


Figure 10. Armour influence on fuselage aerodynamic parameters – colour maps for Drag Coefficient (a), Side Force Coefficient (b), Yaw Moment Coefficient (c).

## CONCLUSIONS

The aerodynamic characteristics of an armoured helicopter have been obtained using CFD methods. For comparison purposes the clean fuselage of the same helicopter has been also analysed. The results are consistent with suspected tendencies, that the armour external shields will decrease aerodynamic efficiency of considered helicopter's fuselage. Decrease of lift force at  $\alpha \geq 0^\circ$ , higher drag for all configurations of angles of attack and sideslip, increase in absolute size of pitching moment, all these are expected effect of using external armour.

The CFD methods, especially finite volume method, are a good tool for evaluating the tendencies of externally mounted devices influence, without using expensive wind tunnel or real flight tests. This concerns both design and upgrade of existing helicopter. As for wind tunnel tests, the scaling issues can be avoided, but only a validated CFD method should be considered.

## ACKNOWLEDGMENTS

This research was supported by project founded by Polish Ministry of Science and Higher Education, Contract No. 0056/R/T00/2009/07

## REFERENCES

- [1] Dziubiński A., "Generacja siatek obliczeniowych w symulacjach CFD" MIWL 2010, Bezmiechowa.
- [2] Gnarowski W., Kajka R., Żółtak J., "Flying Object Armour Concept Analysis Based on Helicopter", ECMS, Simulation meets global challenges, June 2010, p. 126- 130.
- [3] Gnarowski W. „Opracowanie konstrukcji mocowania paneli opancerzenia- pojazd lub śmigłowiec”, Instytut Lotnictwa Internal Report No. 182/BP1-SR/10.
- [4] Grzegorzczak K. „Wykorzystanie metod obliczeniowej mechaniki płynów do modelowania szczególnego przypadku zniżania śmigłowca (VRS)” - MECHANIKA W LOTNICTWIE MLXIV 2010, Polskie Towarzystwo Mechaniki Teoretycznej i Stosowanej.
- [5] Standardization Agreement (STANAG) – 4569, NATO, January2004
- [6] FAA FARs, 14 CFR 1.1, general definitions.
- [7] PZL Świdnik design centre
- [8] "ANSYS ICFM CFD 11.0 Tutorial Manual". 2007.
- [9] "FLUENT 6.1 User's Guide. Fluent Inc". February 2003.

ADAM DZIUBIŃSKI, KATARZYNA GRZEGORCZYK, JERZY ŻÓŁTAK

## **BADANIA NUMERYCZNE WPŁYWU OPANCERZENIA NA CHARAKTERYSTYKI AERODYNAMICZNE ŚMIGŁOWCA**

### Streszczenie

Artykuł dotyczy analizy numerycznej wpływu zewnętrznego opancerzenia na charakterystyki aerodynamiczne śmigłowca. Dla dwu konfiguracji śmigłowca: opancerzonej i wyjściowej (bez pancerza) otrzymano obrazy pola przepływu dla wybranych z użytkowego zakresu kątów natarcia i ślizgu. Wykorzystano komercyjny pakiet oprogramowania Fluent. Rezultaty zostały wykorzystane do obliczenia sił i momentów działających na kadłub śmigłowca. Pracę zakończono analizą wpływu opancerzenia na charakterystyki aerodynamiczne.

## EXCITATION OF A LOCALIZED NONLINEAR NORMAL MODE OF A BLADED DISK ASSEMBLY LUMP MASS NONLINEAR MODEL

FOTIOS GEORGIADES, JERZY WARMIŃSKI

*Lublin University of Technology*

### Abstract

*This article examines a lump mass model of a perfectly symmetric bladed disk assembly of five sectors with nonlinearities in blades. Nonlinear modal analysis and the existence of localized Nonlinear Normal Modes (NNMs) has been shown in previous work [1]. In this article, we demonstrate numerically that it is possible to excite the localized NNMs using travelling waves excitation. Practically this is very important, in case of operation of the assembly in nonlinear regime, then the localized modes must be taken into account, for the proper life-assessment of the assembly. Also this work will be continued with the determination of Nonlinear 'Cambell's' diagram of helicopter blades assemblies, with final aim to control their nonlinear dynamics.*

### INTRODUCTION

In the literature, of linear bladed disk assemblies, localized modes (whereas the energy is spatially confined) is only characteristic of mistuned assemblies and not of perfectly cyclic [2]. Localization of energy in perfectly symmetric cyclic structures, due to nonlinearities, can be found in nonlinear systems [1,9,14]. Taking into account nonlinearities, we must use the theory of NNMs in order to determine the dynamics. Going back to 60's, a pioneer in this field was Rosenberg who defined Normal Modes (similar and nonsimilar), the *vibrations in unison of admissible systems* [6]. Expansion of this work in forced vibrations has been done by Manevitch [7], Mikhlin [8] and Szemplinska-Stupnicka [9], and in 1990's analytically by Caughey and Vakakis [10], Shaw and Pierre [11], Vakakis et al [12], also by Warminski [13-15], and numerically by Kerschen et al. [16], Georgiades [17], Peeters [18,19], and many others. Since Rosenberg, the definition of Nonlinear Normal Modes is extended nowadays to *the periodic motions* of a dynamical system which include the cases of internal resonances with subharmonic NNMs and travelling waves NNMs [16]. We study a model by taking into account only five blades which correspond to helicopter bladed disk assembly. In design of a helicopter bladed disc with geometric nonlinearities, localized NNMs must be taken into account [5].

SYSTEM DEFINITION-EXCITATION FORCES

In case of inextensional beam, the equation of motion in bending vibration, excluding linear and nonlinear inertia terms (which in many cases are very small – they are higher order terms than the order of equation of motion), the nonlinear part is of cubic geometric nonlinearity, for both cases of isotropic and also for symmetric composite beam with orthotropic lamina [20,21]. We construct our cyclic linear viscous model considering cubic nonlinearities in blades. The system is dissipative and it is presented in Figure 1. Modal analysis of the corresponding conservative system (without dissipation) has been examined in paper [1] which showed the existence of localized Nonlinear Normal Modes. The equations of motion of this model are given by,

$$\begin{aligned}
 \text{(blades)} \quad & m\ddot{x}_i + k(x_i - X_i) + k_{nl}(x_i - X_i)^3 + d_s(\dot{x}_i - \dot{X}_i) = F_i(t) \\
 \text{(disks)} \quad & M\ddot{X}_i + k(X_i - x_i) + k_{nl}(X_i - x_i)^3 + d_s(\dot{X}_i - \dot{x}_i) + K(X_i - X_{i-1}) + \\
 & + K(X_i - X_{i+1}) + d_s(\dot{X}_i - \dot{X}_{i-1}) + d_s(\dot{X}_i - \dot{X}_{i+1}) + d_m\dot{X}_i = 0
 \end{aligned}
 \tag{1}$$

whereas,  $x, \dot{x}, \ddot{x}$  are the displacements, velocities and accelerations of blades and  $X, \dot{X}, \ddot{X}$  are the displacements, velocities and accelerations of disks respectively.  $F_i(t)$  is the excitation force which is applied only in blades and also  $i=1, \dots, 5$  and  $X_6=X_1, X_0=X_5, \dot{X}_6=\dot{X}_1, \dot{X}_0=\dot{X}_5$  (the cyclic conditions).

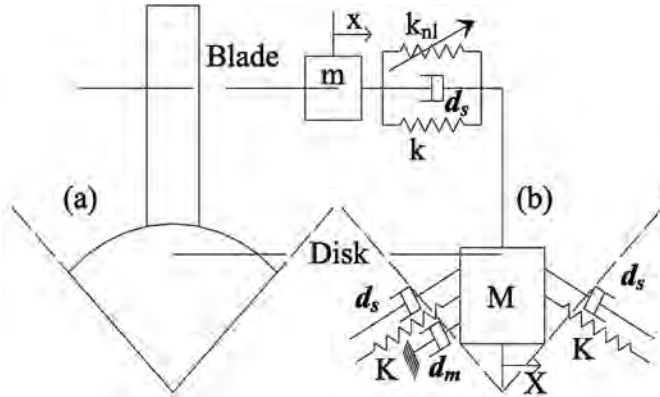


Figure 1. One sector of the model a) continuous model, b) discrete model.

The excitation force is applied only in blades of this system and it is standard travelling waves excitation given by [4],

$$F_i(t) = A \cos(\omega t \pm (i-1) \varphi)
 \tag{2}$$

With  $i=1, \dots, 5$ , the positive sign defines forward travelling waves and the negative sign backwards travelling waves, and  $\varphi$  is the phase difference or spatial frequency (rad/sector) between adjacent blades and is given by,

$$\varphi = \frac{2 \times \pi \times EO}{5}
 \tag{3}$$

whereas EO is the selected Engine Order excitation. Typical case of travelling waves excitation is depicted in Figure 2.

The values of the parameters of the system are given by,

$$M=1, m=0.3, K=1, k=1, k_{nl}=0.1, d_s=0.015, d_m=0.015 \quad (4)$$

The natural frequencies of the corresponding conservative system (without damping) are presented in Table 1. There are 8 modes in pairs and 2 single modes. The first mode with 0 frequency is the rigid body mode whereas the addition of grounded viscous dampers in disks affect to extremely high critical damping ratio in this mode, without influence in our studies. Also in Table 1 are indicated the characteristics of the modes in terms of nodal circles and nodal diameters. In the case of 0 (1) Nodal Circles of normal modes means that at each sector the blade mass is in phase with disk mass (the blade mass is out of phase with disk mass). The case of 0, 1 or 2 nodal diameters corresponds to circumferential examination of amplitudes of mode shapes and we count how many circumferential points of adjacent sectors have opposite sign in amplitudes e.g. for 1 nodal diameter 2 points etc. [1]. This is very important because it is indicating which EO of travelling waves excitation should be used for the excitation of the corresponding mode.

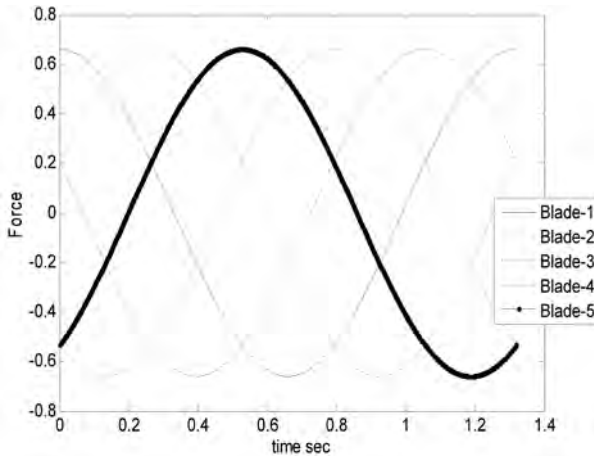


Figure 2. Travelling waves excitation with  $\omega=4.76$  rad/sec

Table 1

Mode	Frequency of conservative system (rad/sec)	Critical Damping Ratio (%)	Nodal Circles	Nodal Diameters
1	0	$8.74 \cdot 10^7$	0	0
2,3	0.99	1.22	0	1
4,5	1.43	1.25	0	2
6	2.08	1.64	1	0
7,8	2.18	1.76	1	1
9,10	2.43	2.03	1	2

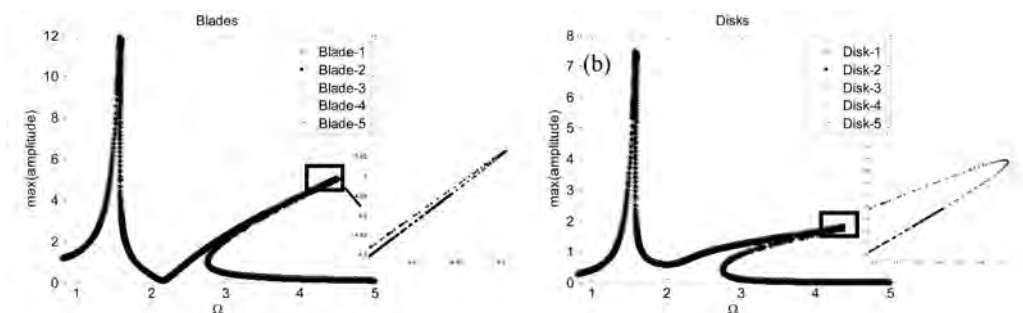
## EXCITATION OF NNMS

In case of non-autonomous systems we determine the steady states (which are periodic motions of  $k$  – periods which corresponds to  $j$  – periods of the excitation frequency e.g. for  $k=j=1$ , there is 1 – 1 steady states on the system) and we examine the resonance points ( $k - j$ , NNMs) in nonlinear Frequency Response Functions (FRFs- maximum amplitudes of displacements or Frequency-Mechanical Energy plots) which, in relative small damping, are very close to curves of maximum amplitudes of displacements with variation of frequency or frequency-energy plot curves of autonomous systems [6,12,16].

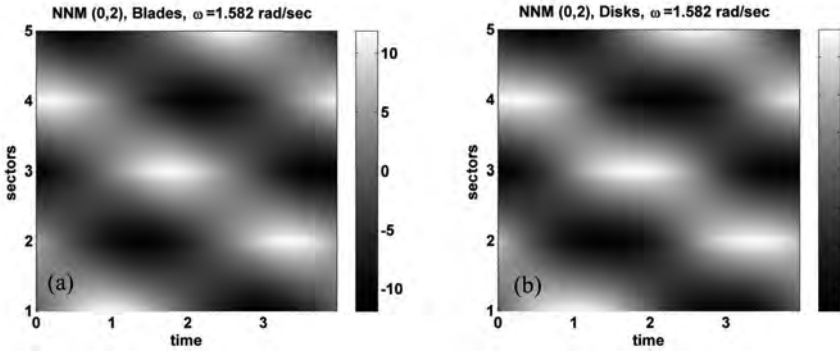
In order to determine numerically the resonance point of the system (NNM) with variation of frequency we use pseudo-arclength and also sequential continuation technique with codes written in Matlab which initially has been developed at University of Liege [15, 16] and has been modified significantly at University of Lublin to meet the requirements of our research.

The travelling waves excitation is applied only in blades. This one used in this article is of  $E_0=2$  with amplitude  $A=0.66$  and it is depicted in Figure 2, in case of  $\omega=4.76$  rad/sec. By application of this excitation, with variation of frequency at periodic motions, we can find the corresponding Nonlinear FRF which is the variation of maximum amplitudes of Blades and Disks at each excitation frequency.

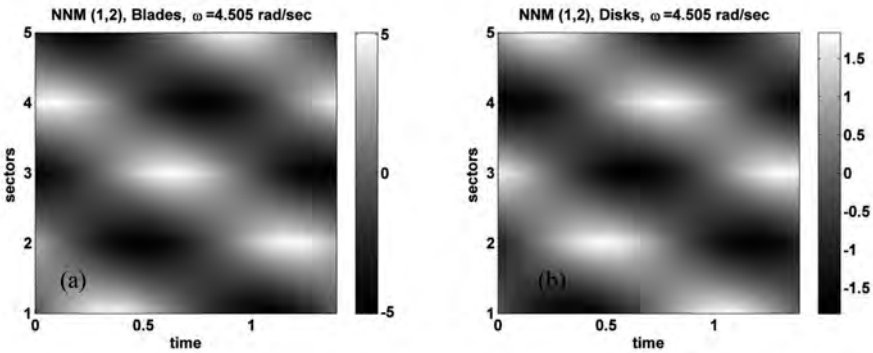
In Figures 3 (a, b), are depicted the Nonlinear Frequency Response Function for blade maximum responses (disks maximum responses). There are 2 resonance points in these Nonlinear FRF's the first one at  $\omega=1.582$  rad/sec, and the second at  $\omega=4.5$  rad/sec. Since it is used  $E_0=2$ , it is expected to be the “evolution” with energy of linear modes (4,5) and (9,10), respectively. Indeed, this is true, which confirms detailed examination at resonance points, as depicted in Figures 4a,b and 5a,b. More precisely, Figure 4a(b) depicts the displacements of blades (disks) for each sector, in time, for the resonance point at  $\omega=1.582$  rad/sec, whereas one can observe that the motions are no “synchronous”. They are in travelling waves form which corresponds to 1:1 internal resonance as shown in [17]. It can be noted that in Figures 4a,b there are 4 inclined ‘lines’ which follows the zero crossings or the maximum absolute amplitudes of the displacements. They correspond to 4 circumferential nodes in pairs of “anti-diametrical” positions and therefore in 2 nodal diameters. Comparison of Figures 4a with 4b, by means of the displacements of blades, with disks for the same sector, shows that they are in phase therefore correspond to 0 zero nodal circle modes. Therefore this mode corresponds to (4,5) linear modes. In Figure 5a(b) are depicted the displacements of blades (disks), for each sector in time, for resonance point at  $\omega=4.5$  rad/sec. Similarly we can see that they correspond to 2 nodal diameters and also 1 nodal circle, therefore to (9,10) linear modes.



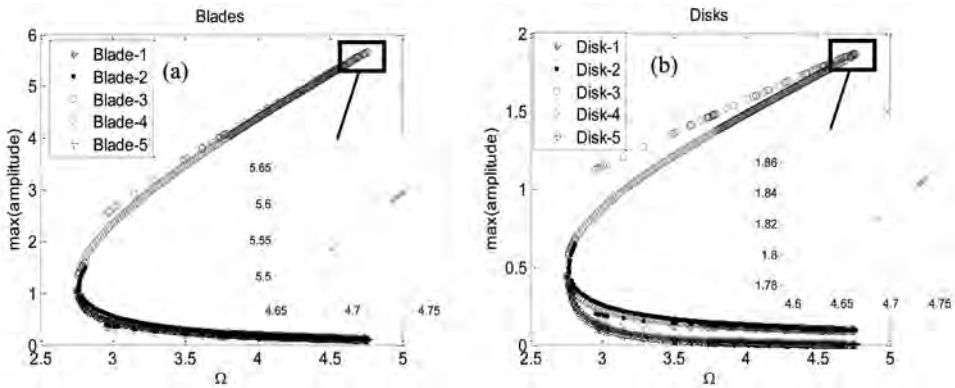
Figures 3. Nonlinear FRF's of a) blades, b) disks



Figures 4. Responses at resonance  $\omega=1.582$  rad/sec, of a) blades b) disks.



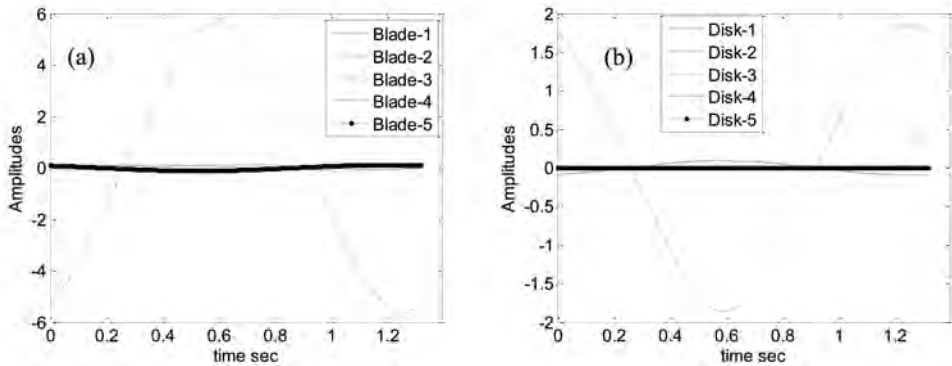
Figures 5. Responses at resonance  $\omega=4.5$  rad/sec, of a) blades b) disks.



Figures 6. Nonlinear FRF's of a) blades, b) disks

We continued the examination of Nonlinear FRF's and we found also another one Nonlinear FRF curve. In Figures 6a,b we may observe the Nonlinear FRF's for a curve which corresponds to a bifurcated curve of the autonomous system. This Nonlinear FRF is rather significant for the assembly since it is related with a localized Nonlinear Normal Mode only in one sector (blade-"3", disk-"3", the system is cyclic so there is no circumferential origin which means no sense in sector 3). In Figure 7 a,b are depicted the displacement of blades (disks) in time, for

this excited mode which corresponds to resonance point with  $\omega=4.76$  rad/sec. It is clear that it represents 1-nodal circle, since the blades are in opposite phase with disks. The nodal diameters are no longer clear that are still 2 due to the almost zero amplitudes of all the other sectors apart the 3<sup>rd</sup> one. The excitation of the assembly of this NNM has been done with the travelling waves applied only in blades (Figure 7).



Figures 7. Responses at resonance of a) blades, b) disks

## CONCLUSIONS AND FUTURE WORK

We showed numerically, that using travelling waves excitation we can excite a localized Non-linear Normal Mode. This phenomenon may play essential role in design of bladed disk assemblies. We will continue our research taking into account rotation of the assembly (centrifugal and Coriolis forces) and construct the Nonlinear ‘Campbell’ diagram using Non-linear Normal Modes techniques. The final aim is to control the dynamics of helicopter blades with active elements e.g. avoiding the excitation of localized Nonlinear Normal Modes.

## ACKNOWLEDGEMENT

The research leading to these results has received funding from the European Union Seventh Framework Programme (FP7/2007-2013), FP7 - REGPOT - 2009 - 1, under grant agreement No:245479.

## REFERENCES

- [1] Georgiades F, Peeters M., Kerschen G., Golinval J.C., Ruzzene M., 2007, “Localization of Energy in a Perfectly Symmetric Bladed Disk Assembly Due to Nonlinearities”, ASME Int. Mechanical Engineering Congress and Exposition, Seattle USA, IMECE2007-41649.
- [2] Ewins, D. J. and Han, Z. S., 1984, ‘Resonant Vibration Levels of a Mistuned Bladed Disk,’ Journal of Vibration and Acoustics, Stress and Reliability in Design 106, pp. 211-217.
- [3] Wei, S.T. and Pierre, C., 1988, ‘Localization Phenomena in Mistuned Assemblies with Cyclic Symmetry, Part I: Free Vibrations,’ Journal of Vibration and Acoustics, Stress and Reliability in Design 110, pp. 429-438.
- [4] Judge, J., Pierre, C., Mehmed O., 2001, ‘Experimental Investigation of Mode Localization and Forced Response Amplitude Magnification for a Mistuned Bladed Disk,’ Journal of Engineering for Gas Turbines and Power 123, pp. 940-950.

- [5] Crespo Da Silva, M.R.M., *Comprehensive Analysis of the Dynamics of a Helicopter Rotor Blade*, *Int. Journal of Solids Structures*, 35, pp.619-635.
- [6] Rosenberg R.M., "On Nonlinear Vibrations of Systems with Many Degrees of Freedom," *Advances in Applied Mechanics* 9, 1966, pp. 155-242.
- [7] Manevitch, L.I., and Cherevatzky, B.P. (1972). Investigation of resonance regimes in nonlinear systems with two degrees of freedom, *Prikl. Mech.*, 9 (12), 74-80 (in Russian).
- [8] Mikhlin, Yu.V., 1974, "Resonance Modes of Near-Conservative Nonlinear Systems," *Prikl. Matem. Mekhan.*, 38, pp. 459-464.
- [9] W. Szemplinska-Stupnicka, Non-linear normal modes and the generalized Ritz method in the problems of vibrations of non-linear elastic continuous systems, *International Journal of Non-linear Mechanics* 18 (1983) 149-165.
- [10] Caughey, T.K., Vakakis, A.F., 1991, "A Method for Examining Steady State Solutions of Forced Discrete Systems with Strong Nonlinearities," *Int. J. Nonlinear Mech.*, 26, pp. 89-103.
- [11] S.W. Shaw, C. Pierre, Non-linear normal modes and invariant manifolds, *Journal of Sound and Vibration* 150 (1991) 170-173.
- [12] Vakakis A.F., Manevitch L.I., Mikhlin Y.V., Pilipchuk V.N., Zevin A.A., *Normal Modes and Localization in Nonlinear Systems*, Copyright by Wiley series in Nonlinear Science 1996.
- [13] Warminski, J., 2008, *Nonlinear Vibration Modes of Parametrically Coupled Self-Excited Oscillators*, *Machine Dynamics Problems*, 32, 4, 107-118.
- [14] Warminski, J., 2008, Nonlinear normal modes of coupled self-excited oscillators in regular and chaotic vibration regimes, *Journal of Theoretical and Applied Mechanics*, 46, No.3, 693-714.
- [15] Warminski J., 2010, Nonlinear Normal Modes of a Self-Excited System Driven by Parametric and External Excitations, *Nonlinear Dynamics*, 61, pp. 677-689 .
- [16] Kerschen G., Peeters M., Golinval J.C., Vakakis A.F., 2009, Nonlinear Normal Modes, Part 1: A useful framework for the structural dynamicist, *Mechanical Systems and Signal Processing*, 23, pp.170-194.
- [17] Georgiades F., Peeters M., Kerschen G., Golinval J.C., Ruzzene M., 2009, "Modal Analysis of a Nonlinear Periodic Structure with Cyclic Symmetry" *American Institute of Aeronautics and Astronautics* 47, pp.1014-1025.
- [18] Peeters M., Georgiades F., Viguie R., Kerschen G., Golinval J.C., 2008, "Development of Numerical Algorithms for Practical Computation of Nonlinear Normal Modes", *Biennial ISMA Conference on Noise and Vibration Engineering*, Leuven Belgium, ISMA2008-0083.
- [19] Peeters, M., Viguie, R., Sérandour, G., Kerschen, G., and Golinval, J. C., 2009, "Nonlinear Normal Modes, Part II: Practical Computation Using Numerical Continuation Techniques," *Mechanical Systems and Signal Processing*, 23, pp. 195-216.
- [20] Nayfeh, A.H., Pai, P.F., *Linear and Nonlinear Structural Mechanics*, Copyright by John Wiley & Sons 2004, Inc.
- [21] Arafat, H.N., 1999, *Nonlinear Response of Cantilever Beams*, PhD Thesis Virginia Polytechnic Institute, USA.

FOTIOS GEORGIADES, JERZY WARMIŃSKI

## LOKALIZACJA NIELINIOWYCH POSTACI DRGAŃ DYSKRETNEGO MODELU UKŁADU WIRNIKOWEGO

### *Streszczenie*

*W pracy przedstawiono analizę drgań dyskretnego, idealnie symetrycznego, modelu struktury składającej się z dysku wraz z dołączonymi pięcioma nieliniowymi sektorami, reprezentującymi nieliniowe łopaty wirnika. Szczegółową nieliniową analizę modalną, jak również możliwość lokalizacji nieliniowych postaci drgań (NNM) zawarto w artykule [1]. W bieżącej pracy przedstawiono numeryczną analizę nieliniowych postaci drgań wzbudzonych za pomocą poruszającej się fali. W przypadku gdy badany układ jest nieliniowy możliwe jest wystąpienie tzw. lokalizacji postaci drgań. Zjawisko to ma istotne znaczenie praktyczne. Powinno być wzięte pod uwagę w celu prawidłowej eksploatacji struktury wielołopatowej oraz zwiększenia jej czasu "życia". Przedstawione badania będą wykorzystane do wyznaczenia diagramu Cambell'a dla wirnika śmigłowca i w konsekwencji posłużą do opracowania strategii sterowania jego nieliniową dynamiką.*

## MODE SHAPES VARIATION OF A COMPOSITE BEAM WITH PIEZOELECTRIC PATCHES

FOTIOS GEORGIADIS, JAROSŁAW LATALSKI, JERZY WARMIŃSKI

*Lublin University of Technology*

### Summary

*In this paper the modal shapes of a light, thin laminate beam with active elements were evaluated. Cases with one or two Macro Fiber Composite (MFC) active elements adhered onto a glass-epoxy cantilever beam were analyzed. The systems under consideration were modeled in ABAQUS finite element software to derive mode shapes numerically. Next, the modes were compared to each other to estimate the influence of PZT patches. First 20 modes of natural vibrations were examined including bending, torsion and axial ones. The comparisons of mode shapes were performed according to Modal Assurance Criterion (MAC) analysis. The examination of changes of mode shapes of the original beam with placement of active elements is the starting point in prior of optimal placements of PZTs with final goal the control of dynamics of helicopter blades.*

### INTRODUCTION

Composite laminate materials are widespread in the fields of aircraft and spacecraft constructions and are continuously increasing within other fields of application. However, high demands to the modern structures tend to combine these composite materials with other ones. One of the most promising perspectives is embedding of piezoelectric actuators because of their advantages of fast response, no magnetic fields, no wear etc. This smart structures technology has the potential to significantly influence aerospace, wind energy etc. industries in e.g. vibration control (induce vibration, vibration mitigation, energy harvesting, adaptronics etc.) and also in structural health monitoring tasks.

The aim of the current study was to examine numerically the mode shapes of a thin multilayer composite cantilever beam. At the second stage of research the effects related to adding PZT patches to the master beam were investigated. The mode shapes for modified systems were compared to the modes of the initial design by means of MAC analysis. Four distinct PZT configurations were checked – one or two symmetric actuators at the clamping or alternatively, at the free end. An exemplary configuration with one patch is shown in Figure 1 (dimensions in mm).

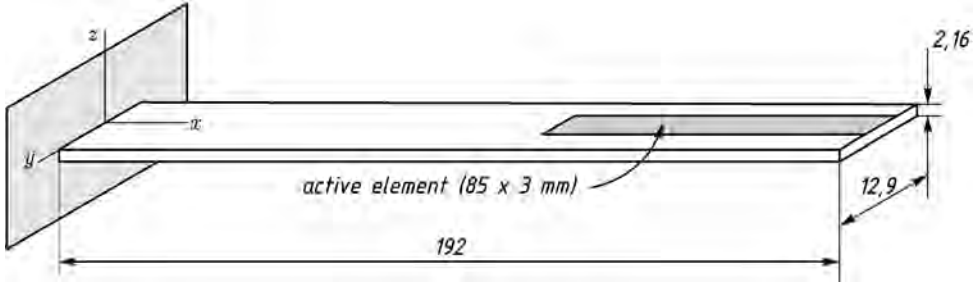


Figure 1. Composite beam under consideration; one PZT element at the free end

## ANALYTICAL MODEL

The system under consideration was described according to Euler-Bernoulli beam theory, where rotary inertia terms were neglected [3, 4, 6]:

$$\frac{\partial N_{xx}}{\partial x} = I_0 \frac{\partial^2 u}{\partial t^2}$$

$$\frac{\partial^2 M_{zz}}{\partial x^2} = I_0 \frac{\partial^2 v}{\partial t^2}$$

$$\frac{\partial^2 M_{yy}}{\partial x^2} = I_0 \frac{\partial^2 w}{\partial t^2}$$

$$\frac{\partial M_{xx}}{\partial x} = J_{xx} \frac{\partial^2 \varphi}{\partial t^2}$$

where  $u$ ,  $v$ ,  $w$  were displacements in  $x$ ,  $y$ , and  $z$  directions respectively and the rotation with respect to  $x$ -axis,

$N_{xx}$  in-plane force resultants and  $M_{xx}$ ,  $M_{yy}$ ,  $M_{zz}$  the moment resultants with respect to  $x$ ,  $y$ , and  $z$  axis respectively,

$$I_0 = \int_{h_{\min}}^{h_{\max}} \rho dz - \text{mass inertia term and } J_{xx} = \int_{h_{\min}}^{h_{\max}} \rho (y^2 + z^2) dy dz .$$

The boundary conditions for the above equations were defined at free end (no shear force and bending moment):

$$\frac{\partial M_{xx}(l,t)}{\partial x} = 0, M_{xx}(l,t) = 0, \frac{\partial M_{yy}(l,t)}{\partial x} = 0, M_{yy}(l,t) = 0$$

$$\frac{\partial M_{zz}(l,t)}{\partial x} = 0, M_{zz}(l,t) = 0$$

and at clamping (no displacement and rotation):

$$u(0,t) = 0, \frac{du(0,t)}{dx} = 0, v(0,t) = 0, \frac{dv(0,t)}{dx} = 0, w(0,t) = 0, \frac{dw(0,t)}{dx} = 0$$

$$\varphi(0,t) = 0, \frac{d\varphi(0,t)}{dx} = 0$$

NUMERICAL MODEL

The master beam was made of unidirectional glass fibers tape and epoxy Prime 20 (Sicomin 8100 + hardener 8824, fibers ratio 50±2%,  $E_f = 69\ 000$  MPa,  $E_m = 3\ 500$  MPa,  $\nu_f = 0.2$ ,  $\nu_m = 0.37$ ,  $\rho_f = 2.56$  g/cm<sup>3</sup>,  $\rho_m = 1.2$  g/cm<sup>3</sup> – all data by manufacturer of a specimen). Based on this the equivalent material properties of a single lamina layer were calculated by rule of mixtures [5]: averaged density  $\rho_{av} = 1.85$  g/cm<sup>3</sup>, Young modulus along fibers  $E_1 = 36\ 250$  MPa, transversal Young modulus  $E_2 = 6662$  MPa, shear moduli  $G_{12} = G_{13} = G_{23} = 2446$  MPa and Poisson’s ratio  $\nu_{12} = 0.285$ . The subsequent layers of the composite were set in the following order: 0°/90°/+45°/-45°/+45°/90°/0° (according to  $Ox$  axis pointing side edgewise).

The MFC patch material data used in the analysis was sourced from Smart Systems Inc. For the simulation the following electric and elastic properties were used: isotropic ferroelectric material with constant permittivity  $\xi = 8 \cdot 10^9$  F/m and mean value of piezoelectric coefficient  $d_{33} = 59 \cdot 10^{-9}$  m/V; elastic orthotropic material having Young moduli  $E_1 = E_2 = 15\ 857$  MPa,  $E_3 = 30\ 336$  MPa, shear moduli  $G_{12} = G_{13} = G_{23} = 5\ 515$  MPa and Poisson ratios  $\nu_{12} = \nu_{13} = \nu_{23} = 0.30$ .

The numerical model of a beam was developed in ABAQUS software. Specimen was defined as a lamina type; and this approach enabled modeling the composite as a set of orthotropic layers in plane-stress state by a Layup-Ply technique [1]. For beam meshing shell elements S4R were used – i.e. linear ones with reduced integration. The actuator was defined by means of second order continuum elements – C3D20RE ones. The final FEM model consisted of 1517/1534 elements and 1873/2085 nodes in total (depending on the number of PZT patches).

The composite material data, electrical properties of PZTs and specimen dimensions used for the numerical tests correspond to the actual beam installed in Laboratory of Dynamics and Strength of Materials at Lublin University of Technology to be used later for experimental validation.

RESULTS

Within the framework of research program first 20 modes of natural vibrations were examined. These included bending, torsion and axial ones as reported in Table 1. The analysis was run for five different cases: composite beam without any active elements, one active element at the free end and next at the clamping and finally, two PZTs at free end and two PZTs at clamping.

Table 1. Modes of natural vibrations of the composite beam under consideration (in bold the ‘mixed’ modes), superscripts “c” and “f” denote the case with actuator(s) at clamped and free end respectively

Mode shape	Beam without PZT/PZTs			
Bending xy plane	2, 6, 11, 17			
Bending xz plane	1, 3, 5, 7, 9, 12, 15, 18, 20			
Torsion	4, 8, 10, 13, 16, 19			
Axial	14			
Mode shape	1-PZT <sup>f</sup>	2-PZT <sup>f</sup>	1-PZT <sup>c</sup>	2-PZT <sup>c</sup>
Bending xy plane	2, 6, <b>10, 11, 16, 17</b>	2, 6, 10, 16	2, 6, <b>10, 11, 16, 17</b>	2, 6, 10, 16
Bending xz plane	1, 3, 5, 7, 9, 12, 15, <b>18, 20</b>	1, 3, 5, 7, 9, 12, 15, <b>18, 20</b>	1, 3, 5, 7, 9, 12, <b>15, 18, 20</b>	1, 3, 5, 7, 9, 12, <b>15, 18, 20</b>
Torsion	4, 8, <b>10, 11, 14, 16, 17</b>	4, 8, 11, 14, 17, 19	4, 8, <b>10, 11, 13, 16, 17, 19</b>	4, 8, 11, 14, 17, 19
Axial	13	13	14	13

For each of the modes the corresponding frequency of natural vibration was calculated. Results for the discussed cases are presented in Table 2. It was shown, that the shift in natural frequencies is more prominent for lower modes; especially for the case of torsion and for bending in the plane of lower stiffness.

Table 2. Comparison of natural frequencies of analyzed systems; superscript “c” denotes the case with actuator(s) at clamped end, superscript “f” denotes the case with actuator(s) at free end

	1	2	3	4	5	6	7	8	9	10
0 PZT	35.48	170.21	221.94	532.29	619.69	1042.74	1209.47	1607.75	1989.17	2715.06
1 PZT <sup>c</sup>	37.73	170.15	228.90	563.63	635.10	1022.55	1232.93	1642.59	2037.79	2740.66
1 PZT <sup>f</sup>	33.55	160.62	221.27	534.19	625.15	1014.30	1225.40	1675.37	2041.40	2739.27
2 PZT <sup>c</sup>	39.99	170.09	234.86	588.24	651.50	1003.73	1255.59	1669.65	2084.50	2674.75
2 PZT <sup>f</sup>	31.91	152.50	220.46	533.74	631.92	988.43	1240.10	1725.00	2091.23	2678.46
	11	12	13	14	15	16	17	18	19	20
0 PZT	2822.39	2953.38	3873.55	3955.32	4095.54	5100.37	5288.94	5407.68	6408.99	6881.82
1 PZT <sup>c</sup>	2796.26	3013.87	3980.84	4006.48	4177.73	5165.97	5220.38	5510.26	6572.24	6992.87
1 PZT <sup>f</sup>	2800.10	3023.93	3785.21	3999.76	4183.66	5172.28	5256.98	5515.80	6584.17	7005.49
2 PZT <sup>c</sup>	2849.05	3079.07	4055.56	4068.55	4253.81	5061.58	5301.40	5619.22	6699.88	7097.54
2 PZT <sup>f</sup>	2857.90	3103.50	3636.89	4088.01	4270.59	5072.88	5379.62	5634.68	6709.93	7125.84

For the description of calculated mode shapes 71 nodes along the length and width of a sample structure were selected (see Figure 2). Translational and rotational degrees of freedom in each node were recorded resulting in configuration space vector having 426 elements in total.

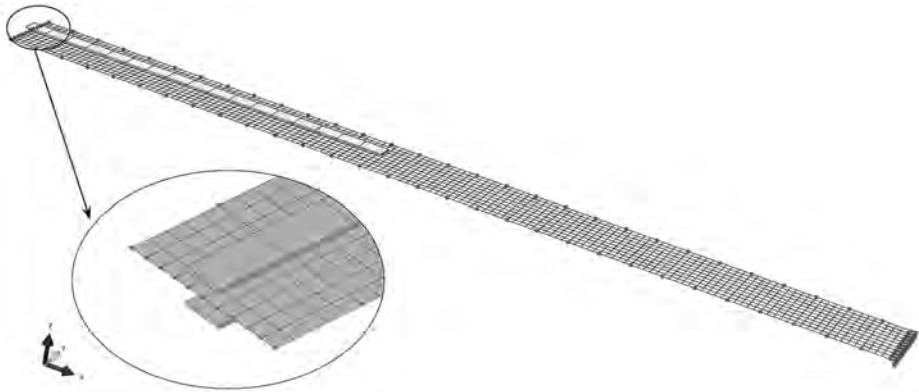


Figure 2. Nodes to describe the beam mode shape

Mode shapes of the beam with PZT patch/patches were compared to the shape of the reference specimen (i.e. the same beam without any PZTs). For quantifying the degree of compatibility between modes Modal Assurance Criterion (MAC, also referred to as Mode Shape Correlation Coefficient) was applied. This provided a measure of the least-squares deviation of the points from the straight line correlation defined by:

$$MAC(A,B) = \frac{\left| \sum_{j=1}^n \varphi_{Aj} \varphi_{Bj} \right|^2}{\left| \sum_{j=1}^n \varphi_{Aj} \varphi_{Aj}^* \right| \left| \sum_{j=1}^n \varphi_{Bj} \varphi_{Bj}^* \right|}$$

where  $\varphi_A, \varphi_B$  – configuration vectors to be compared and  $n$  – their dimension (\* denotes the transpose). According to the literature, it was assumed that MAC value in excess of 0.9 corresponded to well-correlated modes [2].

To estimate the influence of PZT on mode shapes four MAC tests were performed: the reference beam was compared to the system with one PZT (placed at free end or at clamping) and next to the system with 2 PZTs (placed symmetrically both at free end or both at clamping). Results of comparison tests are presented graphically in Figure 3. Next, four additional tests were run to evaluate the effects related to the change in number of PZTs used (beam with 1 PZT at free end vs system with 2 PZTs at free end and beam with 1 PZT at clamping vs system with 2 PZTs at clamping) or to the change of PZT/PZTs position (beam with 1 PZT at clamping vs beam with 1 PZT at free end and 2 PZTs at clamping vs 2 PZTs at free end). Results of these tests are presented graphically in Figure 4.

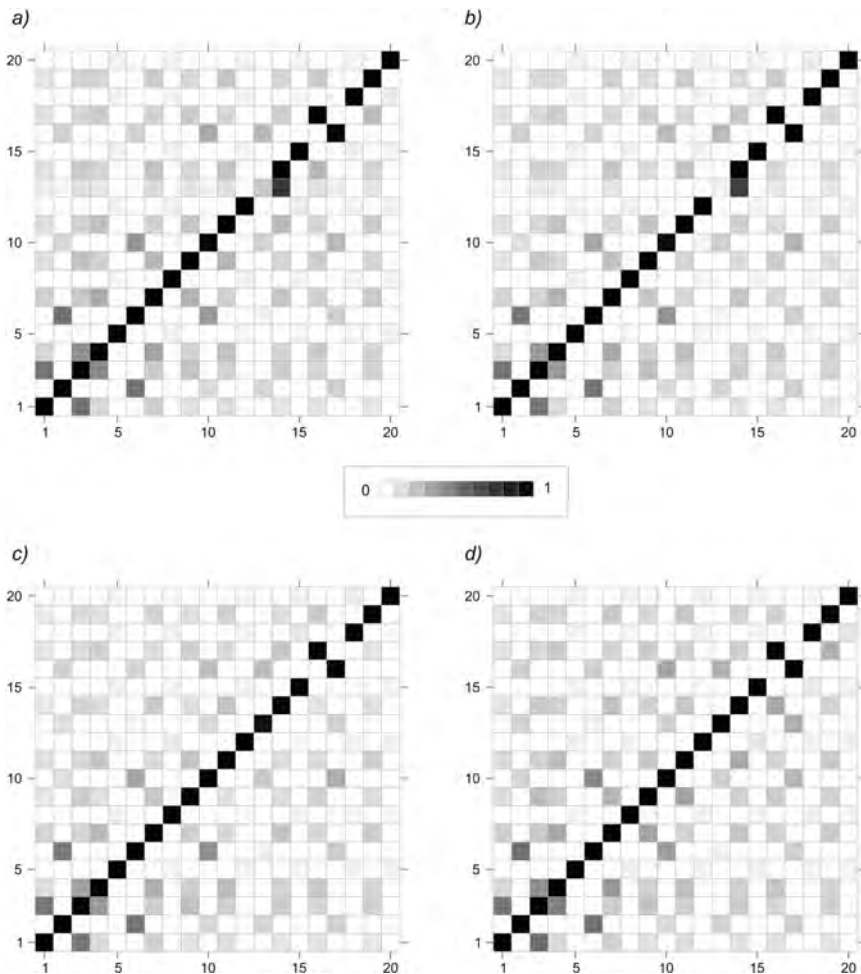


Figure 3. Graphical results of MAC analysis:  
 a) reference beam vs system with 1 PZT at free end,  
 b) reference beam vs system with 1 PZT at clamping,  
 c) reference beam vs system with 2 PZTs at free end,  
 d) reference beam vs system with 2 PZT at clamping

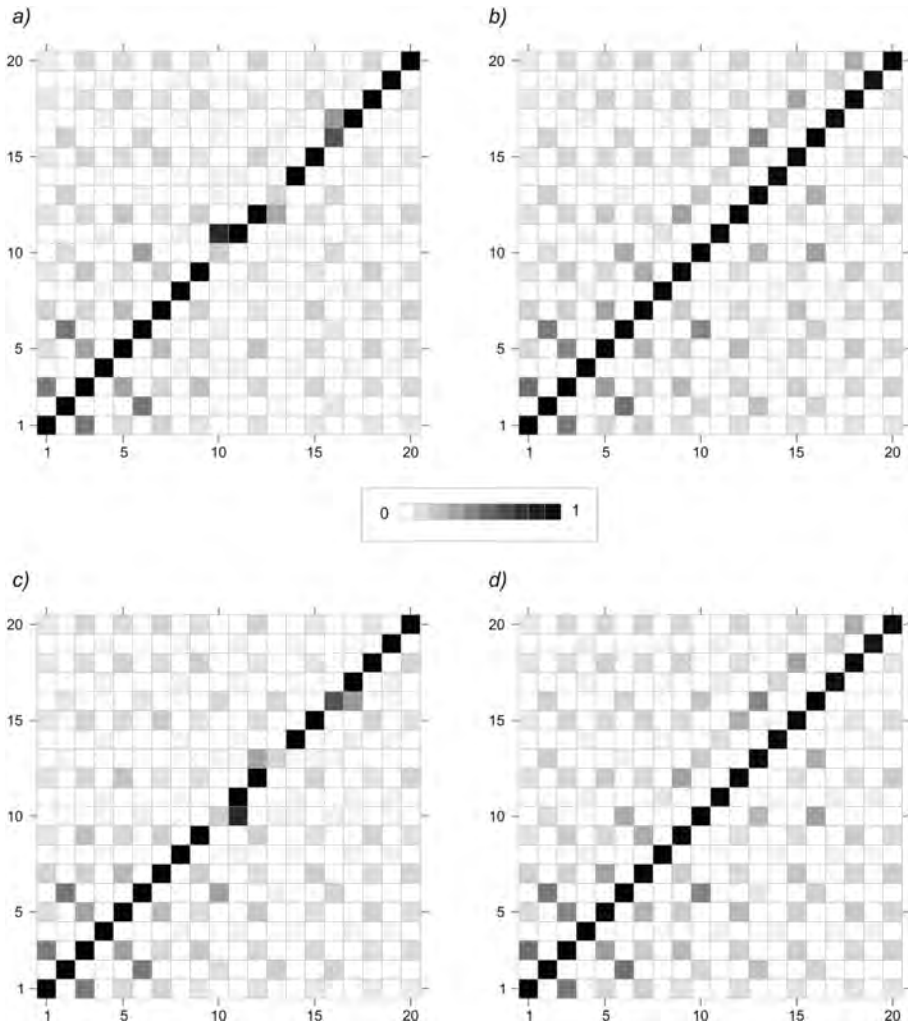


Figure 4. Graphical results of MAC analysis cont.:

- a) beam with 1 PZT at free end vs system with 2 PZTs at free end,
- b) beam with 1 PZT at clamping vs system with 2 PZTs at clamping,
- c) beam with 1 PZT at clamping vs system with 1 PZT at free end,
- d) 2 PZTs at clamping vs 2 PZTs at free end

As a supplement to the above figure the accurate values of MAC diagonal – which is the comparison between the same mode shapes – are tabulated in Table 3.

Table 3. Diagonal of MAC analysis for the discussed cases; indices “c” and “f” denote the case with actuator(s) at clamped and free end. The cases where the mode agreement was not achieved are distinguished by bold typeface

	1	2	3	4	5	6	7	8	9	10
0 - 1 <sup>f</sup>	1.000	0.994	1.000	1.000	0.998	0.999	0.997	0.997	0.995	<b>0.773</b>
0 - 1 <sup>c</sup>	1.000	0.999	0.999	1.000	0.995	0.998	0.998	0.999	0.997	<b>0.557</b>
0 - 2 <sup>f</sup>	1.000	1.000	0.998	0.999	0.994	1.000	0.990	0.991	0.979	<b>0.000</b>
0 - 2 <sup>c</sup>	0.999	1.000	0.996	0.998	0.982	1.000	0.993	0.998	0.987	<b>0.000</b>
1 <sup>f</sup> - 2 <sup>f</sup>	1.000	0.994	1.000	1.000	0.999	0.999	0.998	0.998	0.994	<b>0.226</b>
1 <sup>c</sup> - 2 <sup>c</sup>	1.000	0.999	0.999	1.000	0.996	0.998	0.999	1.000	0.997	<b>0.435</b>
2 <sup>f</sup> - 2 <sup>c</sup>	0.998	1.000	0.990	0.996	0.959	0.999	0.970	0.981	0.935	0.990

	11	12	13	14	15	16	17	18	19	20
0 - 1 <sup>f</sup>	<b>0.003</b>	0.996	<b>0.053</b>	<b>0.000</b>	0.993	<b>0.397</b>	<b>0.002</b>	0.995	0.986	0.993
0 - 1 <sup>c</sup>	<b>0.001</b>	0.997	0.995	<b>0.013</b>	0.996	<b>0.537</b>	<b>0.003</b>	0.996	0.991	0.996
0 - 2 <sup>f</sup>	<b>0.000</b>	0.983	<b>0.000</b>	<b>0.000</b>	0.977	<b>0.000</b>	<b>0.000</b>	0.979	0.959	0.974
0 - 2 <sup>c</sup>	<b>0.000</b>	0.988	<b>0.000</b>	<b>0.000</b>	0.985	<b>0.000</b>	<b>0.000</b>	0.984	0.972	0.985
1 <sup>f</sup> - 2 <sup>f</sup>	0.995	0.996	<b>0.193</b>	0.995	0.994	<b>0.601</b>	0.993	0.995	0.992	0.994
1 <sup>c</sup> - 2 <sup>c</sup>	0.997	0.997	<b>0.000</b>	0.962	0.996	<b>0.459</b>	0.994	0.996	0.995	0.997
2 <sup>f</sup> - 2 <sup>c</sup>	0.956	0.948	0.931	0.920	0.928	0.984	0.900	0.930	0.868	0.924

## CONCLUSIONS

- PZTs added to the reference beam resulted in values of natural frequencies to get shifted – see Table 2. This effect might be both of inertial type (decreasing frequency) and stiffening type (increasing frequency) as well. The observed frequency shifting is more prominent for lower modes; especially for the case of torsion and for bending in the plane of lower stiffness.
- There was no significant difference in mode shapes for placement of 2 PZTs at clamped end or at free end.
- Adding 2 PZTs there was a swap in frequencies of 10, 11, 13 and 14 modes, e.g. order of these bending and torsion modes got reversed.
- Placement of 1 PZT caused the system to be asymmetric. This resulted in modes 10, 11, 16, 17 to have been mixed motion between torsion and xy-bending.
- It is expected that significant differences to the reported ones might happen in cases with PZT exposed to voltage. The series of the appropriate tests will be run during further research.
- We intend to perform a series of similar laboratory tests and to compare the results to the outcomes of these numerical simulations.
- The mode shapes variation of the original beam with placement of PZT patches, is the starting point of our research for optimal position of PZT since as we showed in Table 1 there are structural changes of the mode shapes. As next steps will also be examined the effect of mode shapes variation of a rotating beam. Final goal of our research is a control of dynamics of helicopter blades with active elements.

## ACKNOWLEDGEMENT

The research leading to these results has received funding from the European Union Seventh Framework Programme (FP7/2007-2013), FP7 - REGPOT - 2009 - 1, under grant agreement No:245479.

The financial support of the Structural Funds in the Operational Program Innovative Economy (IE OP) financed from the European Regional Development Fund – research project “Modern material technologies in aerospace industry” number POIG.0101.02-00015/08 is gratefully acknowledged by the first and third author.

## REFERENCES

- [1] --: ABAQUS User's Manual (6.10), Dassault Systèmes, 2010.
- [2] Ewins D.J.: Modal Testing – Theory, Practice and Applications. Research Institute Press Ltd, Philadelphia 2000.
- [3] Kollar, P.L., Springer, G.S., Mechanics of Composite Structures, Cambridge, Cambridge University Press 2003.
- [4] Reddy J.N.: Mechanics of Laminated Composite Plates and Shells – Theory and Analysis. CRC Press, Boca Raton (FL) 2004.
- [5] Staab G.H.: Laminar Composites. Butterworth-Heinemann, Boston, 1999.
- [6] Nayfeh, A.H., Pai, P.F.: Linear and Nonlinear Structural Mechanics, John Wiley & Sons, Hoboken, New Jersey, 2004.

FOTIOS GEORGIADIS, JAROSŁAW LATALSKI, JERZY WARMIŃSKI

## POSTACIE DRGAŃ BELKI KOMPOZYTOWEJ Z ELEMENTAMI PIOZOELEKTRYCZNYMI

### Streszczenie

*W pracy przedstawiono wyniki analizy modalnej lekkiej, cienkiej belki kompozytowej, jednostronnie utwierdzonej, z osadzonymi elementami aktywnymi. Na wstępie przeanalizowano belkę wzorcową – tj. wykonaną z laminatu żywiczno-szklanego bez elementów aktywnych. Następnie zbadano tę samą belkę z dodanym jednym, a w dalszej kolejności także z dwoma kompozytowymi elementami aktywnymi typu MFC (Macro Fiber Composite). Częstości i postacie drgań własnych badanych układów określono numerycznie za pomocą metody elementów skończonych – wykorzystano w tym celu oprogramowanie ABAQUS. Wyznaczono i zbadano 20 pierwszych postaci drgań zawierających zarówno mody giętne oraz skrętne, jak i jedną modę wzdłużną. Do oceny wpływu elementów aktywnych na uzyskane postacie drgań badanej belki wykorzystano kryterium dopasowania modalnego (ang. Modal Assurance Criterion, MAC). Zaprezentowana praca stanowi wstępny etap badań, których celem jest wyznaczenie optymalnego położenia elementów aktywnych sterujących dynamiką łopaty wirnika śmigłowca.*

## VIBRATION AND DAMAGE DETECTIONS OF COMPOSITE BEAMS WITH DEFECTS

EMIL MANOACH\*, \*\*, ANDRZEJ MITURA\*, SYLWESTER SAMBORSKI\*, JERZY WARMINSKI\*

*Lublin University of Technology\*, Institute of Mechanics Bulgarian Academy of Sciences\*\**

### Abstract

*In this work, the geometrically nonlinear vibrations of composite beams subjected to harmonic loading and thermal changes are used to study the sensitivity of selected vibration response parameters to the presence of damage (delamination). The damage detection criterion formulated earlier for non-heated plates, based on analysing the points in the Poincaré sections of the damaged and healthy plate, is modified and tested for the case of beams additionally subjected to elevated temperatures. The importance of the actual temperature in the process of damage detection is shown.*

Key words: *beams, nonlinear vibrations, delamination detections, numerical simulations, Poincaré maps.*

### INTRODUCTION

Structures made of advanced composites are widely used in many modern branches of industry due to advantageous balance among their weight, stiffness and strength. However, the mechanical properties of composite laminates can be significantly reduced by damage, which can occur due to fibre rupture, matrix cracking, debonding, transverse-ply cracking and delamination. Delamination, in particular, is a major problem in multilayer composite structures and may be difficult to detect experimentally using existing methods.

Vibration-based structural health monitoring (VSHM) methods are widely used for damage detection. They are based on the fact that damage will alter the stiffness, mass or energy dissipation properties of the structure which in turn will alter its measured vibration response.

Most of the previous efforts of researchers on VSHM were directed towards methods based on linear modal analysis [1-3]. One of the main problems with these methods comes from the fact that in general damage starts as a local phenomenon and does not necessarily affect significantly the modal characteristics of the structure. Frequency shifts and mode shape changes due to damage (delamination) have been found [4] and are an indicator of damage or structural changes that might be taken into account. However, it seems that the lower order resonance frequencies and mode shapes are not always very sensitive to damage, except for cases with very large damage [3,5,6]. To address some of the above mentioned problems, some authors started to study recently the possibility to employ measured time series of the structure

response and non-linear dynamics theory. Most of the studies in this field are devoted to the extraction of damage sensitive features from the structural vibration response. In [7] the authors use the beating phenomenon for damage detection purposes. In [8] new attractor-based metrics are introduced as damage sensitive features.

In authors' previous works [9 and 10] a numerical approach to study the geometrically non-linear vibrations of rectangular plates with and without damage was developed. A damage index and a method for damage detection and location, based on the Poincaré map of the response, have been proposed. The suggested damage assessment method shows good capability to detect and localize damage in plates. The main objectives of this study are twofold: (i) to study the influence of defects on the dynamic characteristics of the laminated composite beams and on their geometrically nonlinear dynamic response; (ii) to test the criteria for identification of defect (delamination) in composite beams proposed in [9] and [10] by analysing the Poincaré map of the vibration response. The influence of the temperature on the damage detection process will be also briefly commented.

### 1. THEORETICAL MODEL

The object of investigation is a symmetrically laminated beam with length  $l$  and width  $b$ , having  $N_l$  number of layers, symmetrically disposed around the mid-axis (Fig. 1).

The thickness of  $k$ -th layer is  $h^{(k)}$  (located at  $z^{(k)}$  distance from the mid-axis), its Young's modulus  $E^{(k)}$ , Poisson's ratio  $\nu^{(k)}$ , density  $\rho^{(k)}$  and the coefficients of thermal expansion  $\alpha_T^{(k)}$ . The beam is subjected to transverse load  $p(x,t)$  and to temperature variation  $\Delta T$  (with respect to a reference temperature) leading to large amplitude vibrations. In general, the distribution of  $\Delta T$  can be assumed as non-uniform along beam's thickness. The geometrically nonlinear version of the Timoshenko beam theory is used to model the beam behaviour, so that the shear deformation and rotary inertia are taken into account. At each point of the mid-axis of the beam, the displacements in the  $x$  and  $z$  directions are denoted by  $u$  and  $w$ , respectively.  $\psi_x(x,t)$  is the angle of rotation of the normal of the cross-section to the beam mid-axes.

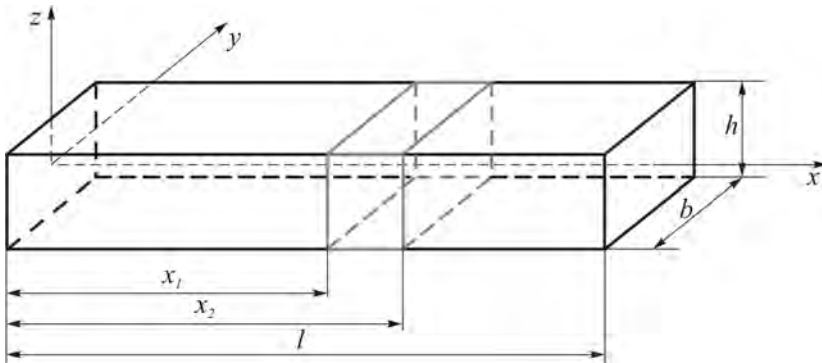


Figure 1. Geometry of the beam.  $x_1$  and  $x_2$  denote the beginning and the end of damaged area

The governing equations for a beam with symmetric lay-ups subjected to mechanical and thermal loading can be written in the following form [11, 12]:

$$\frac{\partial}{\partial x} \left\{ A_{11} \left[ \frac{\partial u}{\partial x} + \frac{1}{2} \left( \frac{\partial w}{\partial x} \right)^2 - \alpha_T \Delta T \right] \right\} = 0 \tag{1}$$

$$\begin{aligned}
& -\frac{\partial}{\partial x} \left( D_{11} \frac{\partial \psi}{\partial x} \right) + k^s A_{55} \left( \frac{\partial w}{\partial x} - \psi \right) - RI \frac{\partial^2 \psi}{\partial t^2} = 0 \\
& k^s \frac{\partial}{\partial x} \left[ A_{55} \left( \frac{\partial w}{\partial x} - \psi \right) \right] + A_{11} \left[ \frac{\partial u}{\partial x} + \frac{1}{2} \left( \frac{\partial w}{\partial x} \right)^2 \right] \frac{\partial^2 w}{\partial x^2} - A_{11} \alpha_T \Delta T \frac{\partial^2 w}{\partial x^2} - RH \frac{\partial^2 w}{\partial t^2} = -p
\end{aligned} \tag{1}$$

Here by  $A_{11}$ ,  $A_{55}$  and  $D_{11}$  are denoted the well know laminate stiffness coefficients (see for example [11]):

$$\begin{aligned}
A_{11} &= b \sum_{k=1}^{N_l} E^{(k)} (z^{(k)} - z^{(k-1)}) = b \sum_{k=1}^{N_l} E^{(k)} h^{(k)} \\
A_{55} &= b \sum_{k=1}^{N_l} G^{(k)} (z^{(k)} - z^{(k-1)}) = b \sum_{k=1}^{N_l} G^{(k)} h^{(k)} \\
D_{11} &= \frac{b}{3} \sum_{k=1}^{N_l} E^{(k)} (z^{(k)3} - z^{(k-1)3}), \quad \alpha_T = \sum_{k=1}^{N_l} \alpha_T^{(k)} \\
RI &= b / 3 \sum_{i=1}^{N_l} \rho^{(i)} (z^{(i)3} - z^{(i-1)3}) \\
RH &= b \sum_{i=1}^{N_l} \rho^{(i)} h^{(i)},
\end{aligned} \tag{2}$$

In Eqns (1) the well know assumption that the longitudinal inertia forces can be neglected is accepted.

The solution of the problem is based on the numerical approach which is similar to the one developed in [9 and 13].

## 2. DAMAGE IDENTIFICATION TECHNIQUE

The identification of damage is based on the criterion suggested in [9] and [10]. Based on these works the following damage index is suggested:

$$I_i^d = \frac{|S_i^u - S_i^d|}{S_i^u}, \quad S_i^u = \sum_{j=1}^{N_p-1} \sqrt{(w_{i,j+1}^u - w_{i,j}^u)^2 + (\dot{w}_{i,j+1}^u - \dot{w}_{i,j}^u)^2}, \quad S_i^d = \sum_{j=1}^{N_p-1} \sqrt{(w_{i,j+1}^d - w_{i,j}^d)^2 + (\dot{w}_{i,j+1}^d - \dot{w}_{i,j}^d)^2} \tag{3}$$

In the above equations  $i=1,2,\dots,N$ , where  $N$  is the number of nodes,  $N_p$  is the number of points in the Poincaré map for each node and  $(w_{ij}^u, \dot{w}_{ij}^u)$  and  $(w_{ij}^d, \dot{w}_{ij}^d)$  denote the  $j^{\text{th}}$  point on the Poincaré maps of the undamaged and the damaged states, respectively. Damage index described above depends on the location of the point on the beam's  $x$ -axis and consequently it is a function of the beam coordinate  $x$ . One can expect that the maxima of the curve  $I^d(x)$  will represent the locations of the damage, i.e.  $I_{\max}^d(x_d) = \max_i \{I_i^d\}$ . The damage criterion based on this index presumes setting a threshold value  $T^d$  for the damage index.

Thus, if the following criterion is fulfilled:

$$I^d(x, \Delta T) > T^d \tag{4}$$

one can conclude that the beam is damaged. Moreover, the sets of points ( $x$ ) for which Eq. (3) is fulfilled, form the damaged area (areas). It is important to note that the temperature changes should also be taken into account. For this reason the damage index defined by Eqs. (3) is calculated at equal values of  $\Delta T$  for the healthy and damaged beams.

### 3. RESULTS AND DISCUSSIONS

The study focuses on delamination of a symmetric cross-ply laminated beam composed of 10 orthotropic layers, each 0.25 mm thick. On the basis of real composite material characteristics effective properties were calculated:  $E_{ef}=41.92$  GPa,  $\nu_{ef}=0.32991$ . The defect was modelled by prescribing to a small part of the beam (10 % of the beam length) reduced rigidity =25.15 GPa. The beam was discretized by 40 linear beam finite elements. The aim of the following examples is to study the dynamic response of composite beams with and without defects, to test numerically the capability of the procedure for damage detection to detect and localize damage (delamination) and then to check it experimentally. Numerical test were performed for fully clamped and cantilever beams. The numerical results shown here concern clamped beams. For cantilevers the results were similar.

The numerical modal analysis of the beams performed by FE method shows, that the introduced defect causes very small changes in the natural frequencies (0.45% decreasing of the first natural frequency in the case of clamped beam). The influence of the defect on eigen frequency was a little higher for the case of the cantilever beam. Obviously such small changes cannot be used as an indicator for damage.

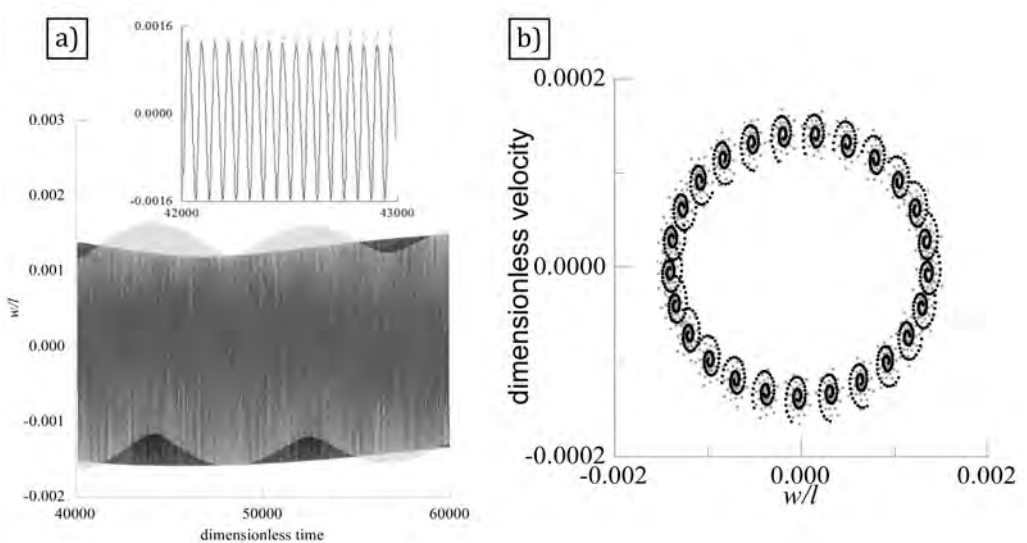


Figure 2. Time-history diagram (a) and Poincaré map (b) of the response of the beam centre of healthy (black colour) and damaged (grey colour) beam.  $\omega_e=5665$  rad/s

Then the forced response of the beam subjected to a harmonic loading is tested. The beam is subjected to two kind of loadings: (a) excitation with frequency of excitation equal (or very close) to the first natural frequency of the beams  $\omega_e=\omega_1$  and (b) excitation equal to the half of the first natural frequency, i.e.  $\omega_e=\omega_1/2$ .

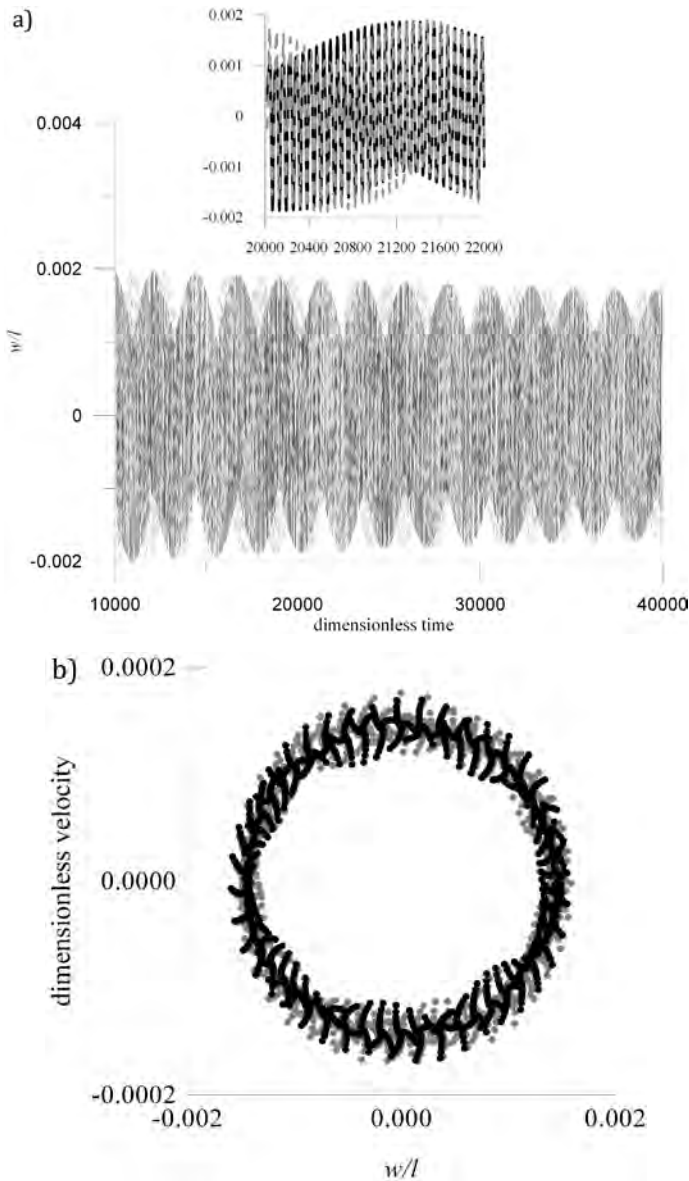


Fig. 3. Time-history diagram (a) and Poincaré map (b) of the response of the beam centre of healthy (black colour) and damaged (grey colour) beam.  $\omega_e = 5665$  rad/s.  $\Delta T = 10$  K

In the cases when the excitation frequency is close to the first natural frequency of the beam a beating phenomenon occurs. From the time-history diagrams (see Fig. 2a) it can be observed that the considered damage leads to some changes in the period of beating and small changes in the amplitude of responses. The influence of damage on the Poincaré maps can be seen in Fig. 2b.

Then the same computations were performed but the beams were additionally subjected to a thermal loading  $\Delta T = 10$  K. The thermal loading lead to changes in the time-history diagrams and Poincaré maps of the healthy and damaged beams as it can be seen in Fig. 3.

In Figs 4 a-b time history diagrams at excitation frequency almost equals to the first natural frequency of the healthy beam ( $\omega_e = 11330$  rad/s) are shown. From these time-history diagrams it can be concluded that the considered damage leads to small changes in the amplitude of responses but the time histories undergo significant changes in the period of beating. It can be seen that at the very beginning ( $t=0$ ) the responses almost coincide. Then the phase shifts and the differences between the responses increase (see small figures inserted in the main figures where the time histories are shown for a very short period of time).

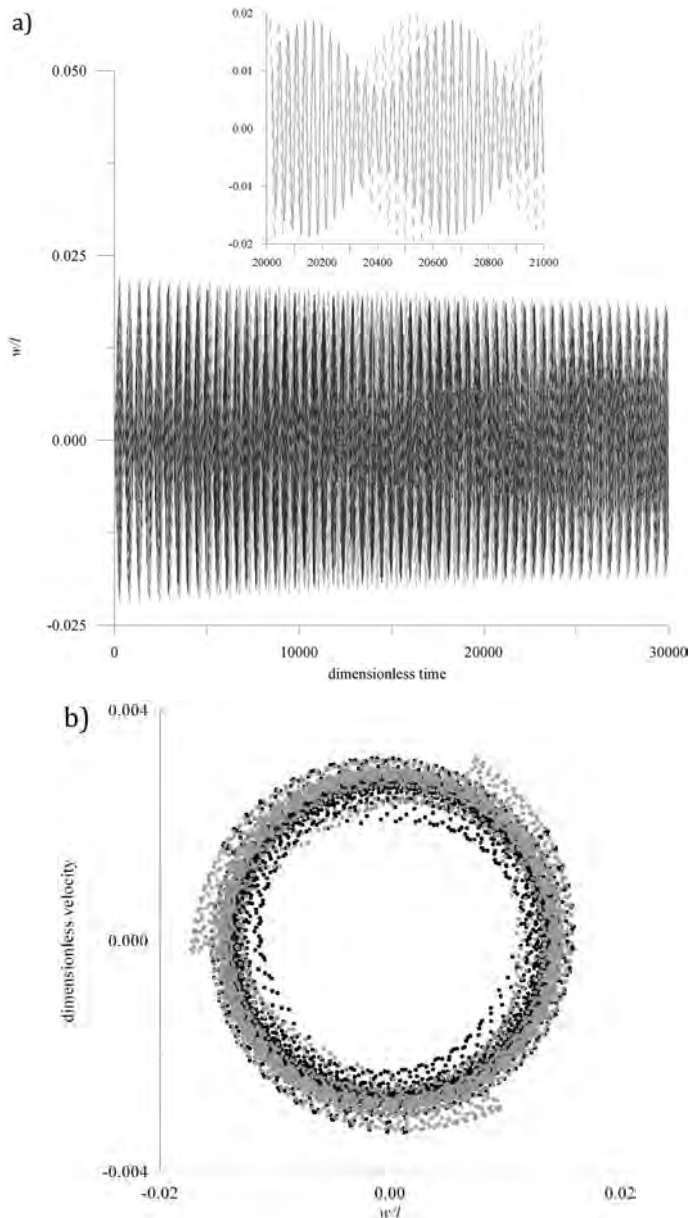


Figure 4. Time history diagrams (a) and Poincaré maps (b) for the response of the beam centre.  $p=50$  N,  $\omega_e = 11330$  rad/s. Black line – healthy beam; gray line – damaged beam

For all cases the damage indexes were computed by using formulas (3). The damage index for the considered cases of damage show very precisely the location of the damage. The elevated temperature in the considered case increase the influence of damage and the values of the damage index.

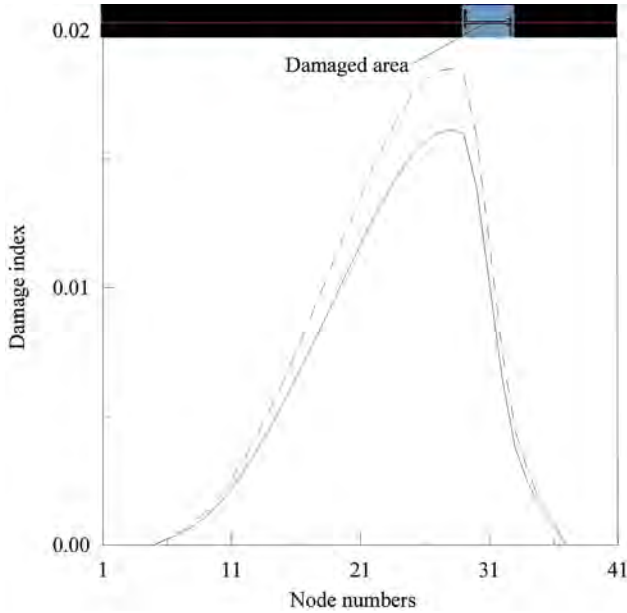


Figure 5. Damage index for a beam subjected to harmonic mechanical loading with an amplitude  $p=50$  N, excitation frequency  $\omega_e= 5665$  rad/s for two different temperatures. Solid line  $\Delta T=0$  K, dashed line  $\Delta T=10$  K.

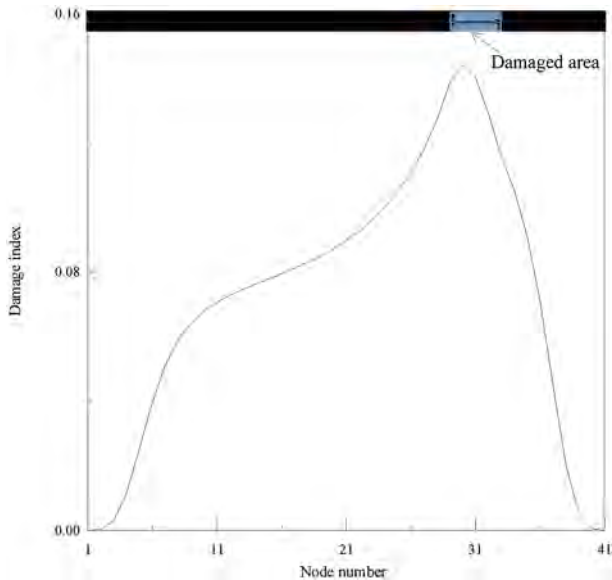


Figure 6 Damage index for a beam subjected to harmonic mechanical loading with an amplitude  $p=50$  N, excitation frequency  $11330$  rad/s

#### 4. EXPERIMENTAL TEST

The preliminary tests for the applicability of the suggested damage detection criterion were performed.

Laminate composite beams were considered. Two different cantilever beams were fixed at one end in a shaker clamp. A special clamp was designed in order to model precisely the clamped boundary conditions. By using this clamp the first three measured and computed natural frequencies were practically identical. The length of the samples was 93mm counting from the clamp. The sequence of glass-epoxy plies was the following:  $[+45^\circ/-45^\circ/+45^\circ/-45^\circ/0^\circ]_s$  (10 layers). The laminates were fabricated by a “prepreg” technology. Single preimpregnated ply had a thickness of 0.255mm. Fiberglass had a form of roving tapes. One composite beam was called healthy as it had no delaminated area. The damaged beam had a delaminated area located at 40mm from the clamp. The length of the delamination (along the beam axis) was 10 mm. Delamination (damage) was artificially introduced in the mid-plane of the laminate by a PTFE foil (0.02mm thick) on the whole width of the beams. It was found by three point bending test that this delamination leads to reduction of the Young’s modulus in the damaged area by 40 %. Vision Research’s Phantom v9.1 high speed camera was used for observation and measurement of the composite beams responses. The camera provides 14-bit image depth and 1016 frames per second at full resolution (1632x1200 pixels). The camera is controlled by a PC with a special software “TEMA”.

Each composite beam was clamped at one of its ends (cantilever beam) and was subjected to harmonic kinematic excitation with frequency 123 Hz by “TiraVib” TV 50101 shaker. The vibration isolators of the shaker frame save the camera from undesired vibration of the laboratory foundation.

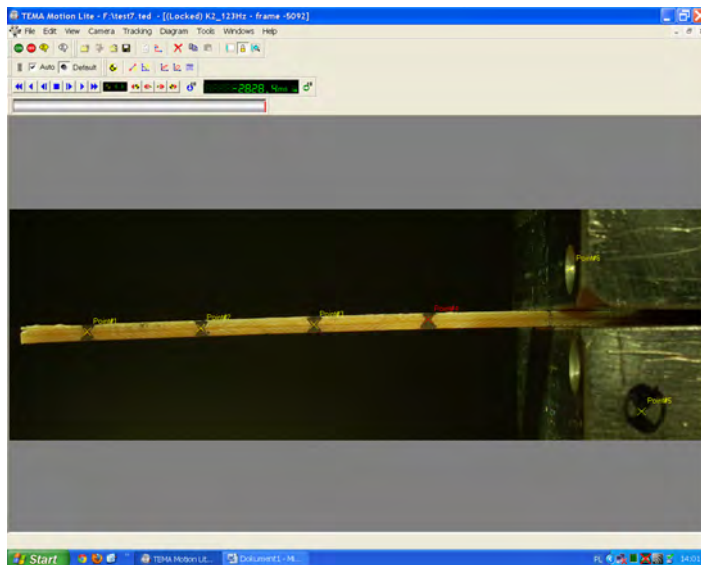


Figure 7. A picture taken by the high-speed camera during the beam vibrations

In Figure 7 a picture from the high speed camera is shown. The recorded values of the displacements and the velocity were proceeded in order to obtain the Poincaré maps for healthy and damaged beams and then the damage index was computed. The results are plotted in Figure 8.

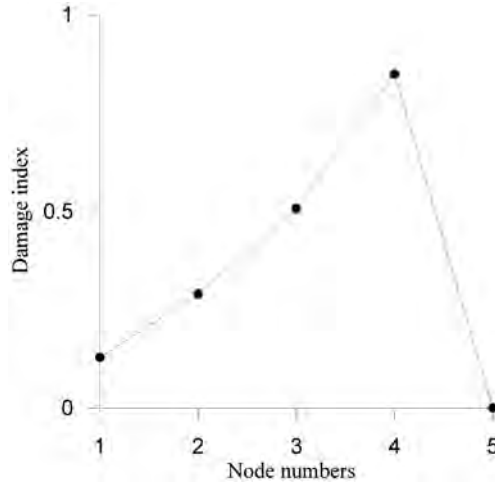


Figure 8. Damage index along the beam length obtained experimentally.

The vibration response was measured in four points only (see Fig. 7) but the results show a good prediction of the damage. These experimental results should be considered as a preliminary and we don't make a general conclusions only on the base of these results. A new tests with an improved experimental set up will be performed and more results for composite structures with different damages will be tested in order to estimate the sensitivity and applicability of the method.

## CONCLUSIONS

Computed time-domain responses have been used to analyse the behaviour of either intact or damaged beams. Based on these analyses a conception of damage index developed previously was adapted and applied for damage detection and location. It was demonstrated that damage can influence substantially the time-domain response of a beam despite its very small influence on the beam natural frequencies.

The preliminary experiments confirmed the applicability of the method.

## ACKNOWLEDGMENTS

The research leading to these results has received funding from the European Union Seventh Framework Programme (FP7/2007-2013), FP7 - REGPOT - 2009 - 1, under grant agreement No:245479. The first author wishes to acknowledge the partial support received through Bulgarian NSF Grant DCVP 02/1.

## REFERENCES

- [1] Zou, Y., Tong, L., Steven, G. P., 2000, Vibration based model- dependent damage (delamination) identification and health monitoring for composite structures – a review. *Journal of Sound and Vibration* 230(2), 357-378.
- [2] Verboven, P., Parloo, E., Guillaume, P., Overmeire, M. Van, 2002, Autonomous structural health monitoring—part I: modal parameter estimation and tracking. *Mechanical Systems and Signal Processing*, 16, 637–657.

- [3] Doebling, S.W., Farrar, C.R., Prime, M.B., Shevitz, D.W., 1996, Damage identification and health monitoring of structural systems from changes in their vibration characteristics: A Literature Review, Report LA- 12767-MS, Los Alamos National Laboratory, NM, USA.
- [4] Shen, M.H., Grady, J. E., 1992, Free Vibrations of Delaminated Beams. AIAA Journal 30 (5), 1361- 1370.
- [5] Banks, H.T., Inman, D.J., Leo, D.J., Wang, Y., 1996, An experimentally validated damage detection theory in smart structures. Journal of Sound and Vibration 191, 859-880.
- [6] Reddy, A.D., Rehfield, L.W., Haag, R.S., 1984, Influence of prescribed delaminations of stiffness-controlled behaviour of composite laminates, Effects of Defects in Composite Materials, ASTM STP 836, American Society for Testing and Materials, 71-83.
- [7] Cattarius, J., Inman, D.J., 1997, Time domain analysis for damage detection in smart structures. Mechanical Systems and Signal Processing 11, 409-423.
- [8] Todd, M., Nichols, J. M., Pecora, L. M., Virgin, L., 2001, Vibration-based damage assessment utilizing state space geometry changes: local attractor variance ratio. Smart Materials and Structures, 10, 1000-1008.
- [9] Manoach, E. Trendafilova, I. Large Amplitude Vibrations and damage detection of rectangular plates J. Sound & Vibrations, 315 (3), pp. 591-606 (2008).
- [10] Trendafilova, I., Manoach, E. Vibration Based Damage Detection in Plates by Using Time Series Analysis. Mech. Systems and Signal Processing 22 (2008) 1092-1106.
- [11] Altenbach, H., Altenbach, J., Kissing, W., 2001, Structural Analysis of Laminate and Sandwich Beams and Plates. An introduction into the mechanics of composites. Lubelskie Towarzystwo Naukowe, Lublin.
- [12] Reddy, J.N., 2003, Mechanics of Laminated Composite Plates and Shells: Theory and Analysis. (second edition) CRC press.
- [13] Manoach, E., Ribeiro P., 2004, Coupled, thermoelastic, large amplitude vibrations of Timoshenko beams. International Journal of Mechanical Sciences, 46, 1589-1606.

EMIL MANOACH, ANDRZEJ MITURA, SYLWESTER SAMBORSKI, JERZY WARMIŃSKI

## **DRGANIA A WYKRYWANIE USZKODZENIA W BELKACH KOMPOZYTOWYCH**

### Streszczenie

*W niniejszej pracy omówiono wykorzystanie drgań nieliniowych belek kompozytowych, podanych wymuszeniom harmonicznym i obciążeniom cieplnym, do celów wykrywania uszkodzenia (delaminacji). Przystudowano czułość wybranych parametrów opisujących dynamiczną odpowiedź układu na obecność wady w strukturze. Kryterium uszkodzenia, sformułowane we wcześniejszych pracach autorów dla niepodgrzewanych płyt, oparte na porównywaniu map Poincaré dla płyty zdrowej oraz uszkodzonej, zostało zmodyfikowane i przetestowane na strukturach belkowych. W modelach numerycznych belek zastosowano dodatkowo działanie podwyższonej temperatury. Pokazano w ten sposób istotne znaczenie temperatury na proces wykrywania uszkodzenia. Zaprezentowano także pierwsze wyniki badań doświadczalnych.*

## ROTOR BLADE SEGMENT WITH PIEZOACTUATED TRAILING-EDGE FLAP FOR DYNAMIC PRESSURE MEASUREMENTS

MAREK MILLER

*Institute of Aviation*

### Abstract

*This paper summarise the entirety of previous activities concerning the design of the segment of rotor blade with a trailing-edge flap actuated by Amplified Piezo Actuator used in dynamic pressure measurements in T-1 low-speed wind tunnel of the Institute of Aviation. The designed rotor blade segment, based on the ILH412M-S profile, will be used to derive aerodynamic loads in a two-dimensional flow according to assumptions of the research project "Research on the active control of the airflow of helicopter rotor blade with the use of a flap oscillation and a microflap to improve aerodynamic performance of a helicopter".*

### INTRODUCTION

The main part of the project "Research on the active control of the airflow of helicopter rotor blade with the use of a flap oscillation and a microflap to improve aerodynamic performance of a helicopter" (grant No. N 509 003 31/0251) is focused on the helicopter rotor blade segment with active control system used to deflections of the trailing-edge flap (TEF). The ILH412M-S profile, designed in the Institute of Aviation, was chosen for that segment of 480 mm of chord and 1000 mm of span, and a pitching axis in an aerodynamic centre in 25% of chord. The deflection of TEF modifies the airflow around the blade which cause changes of the aerodynamic performance of the rotor and the whole helicopter. The TEF deflection is achieved as the result of the deformation of Amplified Piezo Actuator (APA) which is connected with TEF by the mechanical system of lever and tappet. APA1000XL-SG piezo actuator by CEDRAT TECHNOLOGIES was chosen not only as the source of force and strain but also as the source of information about a strain (and the TEF deflection after calculations) [1]. On both surfaces of the blade segment 73 pressure measurement points were prepared for the connection to three ESP-32HD pressure scanners of DTC Initium pressure measurement system by Pressure Systems Inc.

### NUMERICAL ANALYSIS FOR TEF PROPERTIES

The first step in the designing of a helicopter rotor blade segment with active control system used to deflections of the TEF were numerical calculations in ANSYS FLUENT flow modelling software.

As a base ILH412M-S profile was chosen (Fig. 1) which was designed for a new rotor blade for Sokol-2 helicopter. Numerical calculations made in FLUENT were aimed on the choice of the most effective size of TEF. The 2-dimensional analysis was made for the segment of 440 mm of chord and the pitching axis in the aerodynamic centre in 25% of chord. In the 3-dimensional analysis loads acting on the segment and the TER actuation mechanism, for the segment of span of 600 mm, were made. Three amounts of TEF were taken into consideration: 10%, 15% and 20% of chord. In numerical calculations small influence of 10% chord TEF was noticed. Both, 15% and 20% chord TEF, showed their bigger and similar influence on aerodynamic lift coefficients, but 20% chord TEF generated bigger aerodynamic pitching moment. After comparison with available papers and applied TEF-blade configurations (e.g. RPA blades on BK-117 by Eurocopter), 15% TEF was chosen for further consideration and design (Fig. 1). According to further modifications concerning a real rotor blade of Sokol-2 helicopter, the blade chord was lengthened up to 480 mm and the span of the segment up to 1000 mm. Both, 2- and 3-dimensional analysis was repeated.



Fig. 1. ILH412M-S airfoil with 15% TEF

PIEZOELECTRIC TEF ACTUATOR

It was assumed that 15% TEF will be actuated by Amplified Piezo Actuator (APA) designed by CEDRAT TECHNOLOGIES.

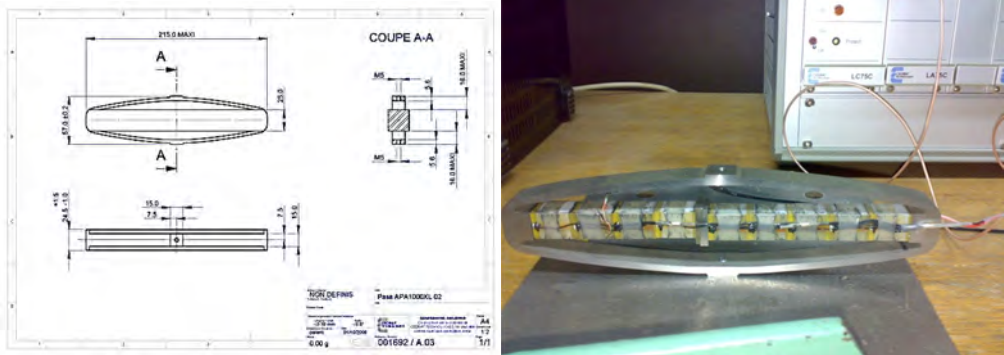


Fig. 2. APA1000XL-SG by CEDRAT

APA1000XL-SG model (Fig. 2) was chosen because its large displacement up to 1250  $\mu\text{m}$  and big blocking-force of 745 N. APA with strain gauge (-SG) option was chosen because the possibility of the measurement of its displacement (that is connected with the angle of a TEF deflection). Similar, but smaller APA750 actuator was used in the test rotor of BK-117 by Eurocopter (Fig. 3), which also influenced on the decision of the choice of a tested solution using in a helicopter industry.



Fig. 3. BK-117 with RPA blades

APA1000XL-SG is driven by the set of electronic equipment (signal controller, power amplifier, etc.) by CEDRAT TECHNOLOGIES (Fig. 4). A control signal is given to an input of LC75C signal controller which takes care of the quality and range of input voltage to prevent the APA piezo actuator against a damage. Conditioned signal is given to the input of LA75C linear power amplifier with the voltage amplification of 20. SG75-1 1-channel strain gauge conditioner is used for the reading of signal emitted by the strain gauge mounted on the APA actuator (-SG option) and for a power supply for a strain gauge bridge. All above-mentioned elements are mounted in RK63F-4U rack.



Fig. 4. RK63F-4U/LC75C/LA75C/SG75-1

#### ILH412M-S ROTOR BLADE SEGMENT

The necessity of oscillations and the possibility of the appearance of inertial loads resulting from it caused the design of the light composite model of the ILH412M-S rotor blade segment. It was assumed that the tested blade segment would be based on a new helicopter rotor blade designed for Sokol-2 helicopter. The ILH412M-S profile, designed in the Institute of Aviation, was chosen for that purpose. Rotor blade segment based on the real helicopter rotor blade had 480 mm of chord and 1000 mm of span. It was assumed that the pitching axis is in the aerodynamic centre in 25% of chord. The segment was equipped with TEF which chord is the result of earlier analysis. The length of TEF was established as 15% of profile chord.

Drawings of a whole segment with the TEF oscillation mechanism, three ESP-32HD pressure scanners and 73 pressure measurement points are presented in Fig. 5 and 6.

In the beginning moulding plates for ILH412M-S airfoil were prepared. A few layers of composite were arranged on them to make a lower and an upper surface of the profile.

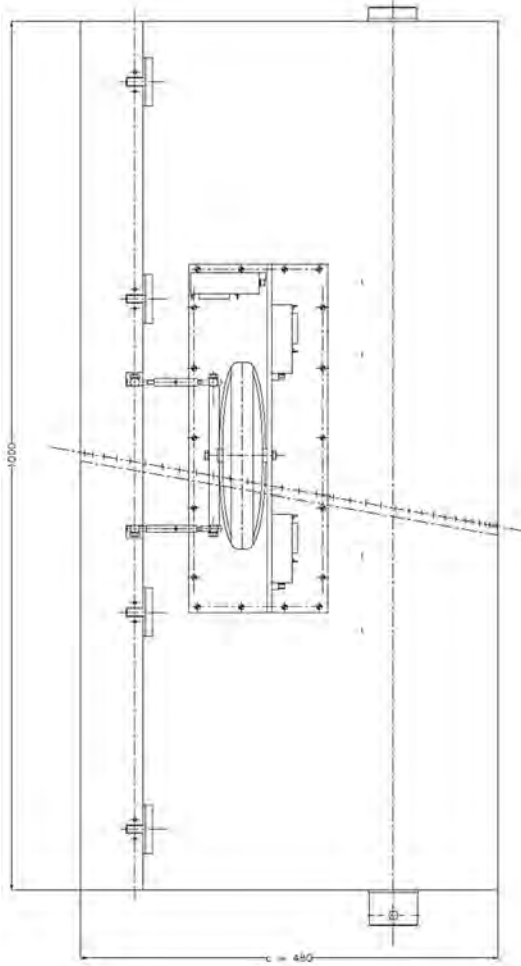


Fig. 5. The drawing of ILH412M-S airfoil with TEF oscillation mechanism

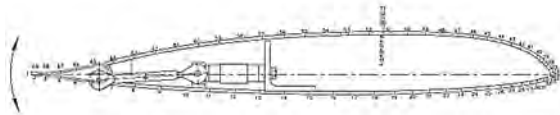


Fig. 6. The cross section of ILH412M-S airfoil with TEF oscillation mechanism and pressure measurement points

Additional composite, wooden and steel stiffening (Fig. 7) was added to the rotor blade segment, especially around the area where the TEF oscillation mechanism actuated by APA1000XL-SG piezo actuator and three ESP-32HD pressure scanners by Pressure Systems Inc. were mounted.

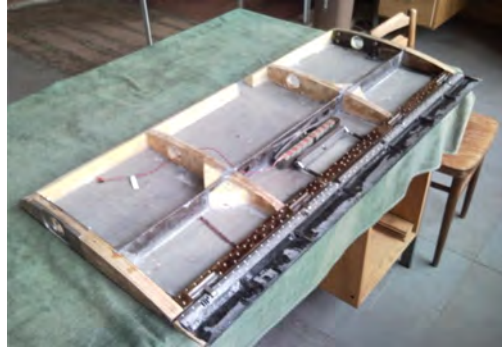


Fig. 7. The stiffening of ILH412M-S segment

### DTC INITIUM PRESSURE MEASUREMENT SYSTEM

DTC Initium pressure measurement system by Pressure Systems Inc. was used for pressure acquisition. It is a pressure measurement and data acquisition system (Fig. 8) made of DTC Initium central unit (Fig. 9) connected to a computer and up to eight pressure scanners, of 16, 32 or 64 channels each. Pressure measurements and data acquisition were made in all channels with frequency of 650 Hz in case of use of 32-channel scanners.

Three 32-channel ESP-32HD pressure scanners by Pressure Systems Inc. were elements of that system which were mounted into the rotor blade segment. All of them have its pressure measurement range up to 10 inWC. They were connected to 73 pressure measurement points by silicon tubes of equal length.

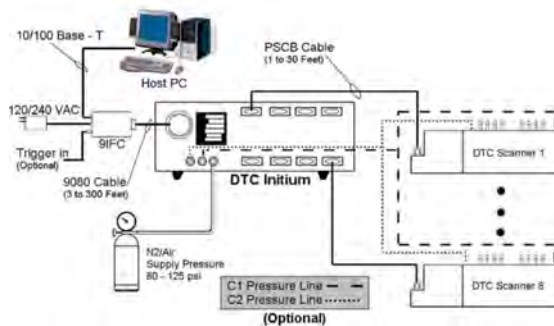


Fig. 8. The scheme of DTC Initium system



Fig. 9. DTC Initium with ESP scanners

## TESTS OF PIEZO ACTUATED TEF

In the beginning general tests were made to check the correct action of CEDRAT APA1000XL-SG piezo actuator (Fig. 10). Tests were focused on the proper deflection of TEF, its amplitude according to the given voltage. The TEF oscillation mechanism was calibrated and the neutral deflection of TEF was set according to the range of supply voltage of APA1000XL-SG piezo actuator.



Fig. 10. Tests of CEDRAT APA piezo actuator

Deflections of TEF, of different flap oscillation frequencies, were registered by a high speed video camera Centurio C100 by Citius Imaging (Fig. 11). The side view of the ILH412M-S airfoil was covered by a mask on which a chord line and the hinge axis of TEF were marked (Fig. 12). After recording, single “photographs” of the deflected TEF in its minimal and maximal positions, were taken for different oscillation frequencies. And amplitudes were calculated.



Fig. 11. High speed video camera Centurio C100 by Citius Imaging

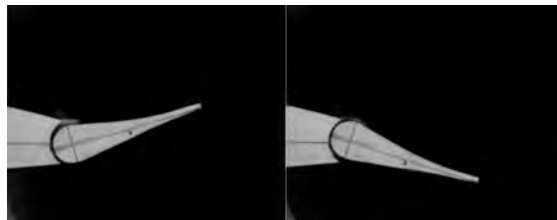


Fig. 12. Extreme TEF deflections at 20 Hz

As it is presented in Figures 13 and 14 the increase of TEF oscillation frequency causes the increase of TEF oscillation amplitude. Measured values of TEF amplitude do not grow linearly

but are almost constant for two ranges of frequencies: from 1 to 7 Hz and from 9 to 15 Hz. Further increase of TEF oscillation frequency implies stronger increase of TEF oscillation amplitude.

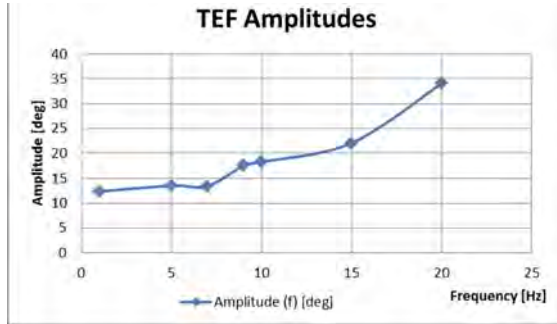


Fig. 13. Amplitudes of TEF oscillations

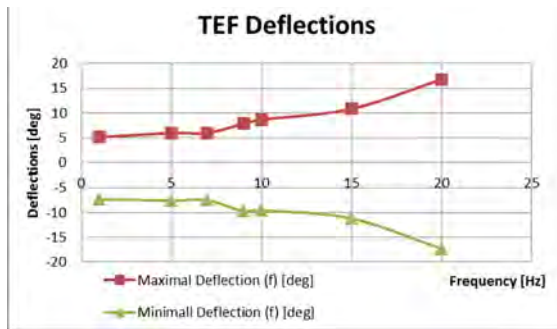


Fig. 14. Extremes of TEF oscillations

### TESTS OF PRESSURE MEASUREMENT SYSTEM

Tests of pressure measurement system based on DTC Initium were made in Utility Software (Fig. 15). Each channel of three ESP-32HD scanners used in tests were checked if they measure a proper, earlier defined pressure. This test allowed to avoid further problems with the leakiness of pressure tubes, badly connected scanners, mistakes in pressure measurements.

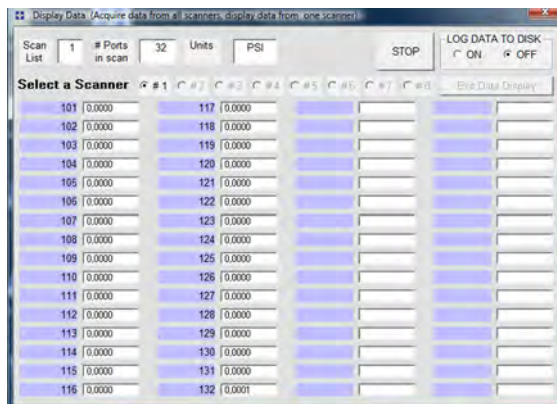


Fig. 15. DTC Initium Utility Software in "Display Data" mode

## ILH412M-S SEGMENT IN T-1 WIND TUNNEL

Our rotor blade ILH412M-S segment was mounted in the test chamber of the T-1 low speed wind tunnel in a position presented in Fig. 16 and 17. It was positioned between two side plates. The lower side wall was mounted on the frame and the upper side wall was hanged on wires (Fig. 16). The pitch angle of the rotor blade segment and TEF oscillations were also monitored by CCTV set. Behind the segment a rake was installed (Fig. 17).

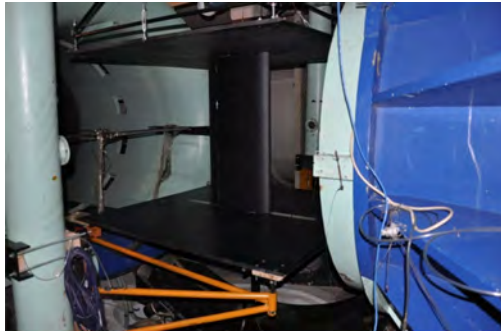


Fig. 16. The blade segment between side walls

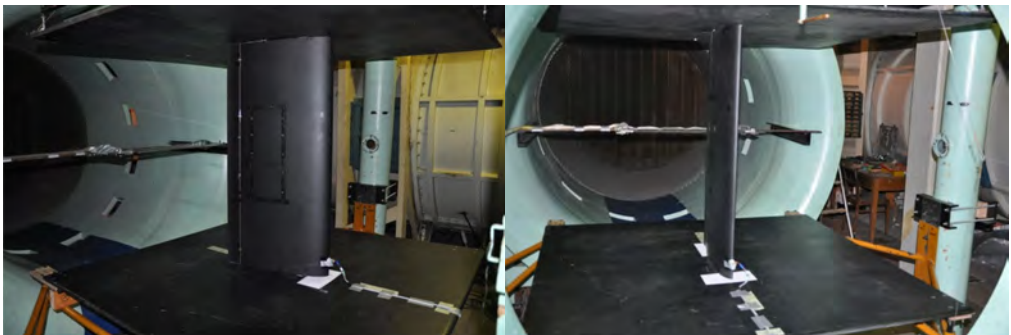


Fig. 17. The blade segment in T-1 wind tunnel

## CONCLUSIONS

The designed rotor blade segment, based on the ILH412M-S profile, presented in this paper, will be used to derive aerodynamic loads in a two-dimensional flow in the T-1 low speed wind tunnel, for further numerical analysis of the aerodynamic performance of a helicopter.

## ACKNOWLEDGEMENT

This paper is the result of activities which have been carried out in the research project "Research on the active control of the airflow of helicopter rotor blade with the use of a flap oscillation and a microflap to improve aerodynamic performance of a helicopter" (grant No. N 509 003 31/0251) funded by Polish Ministry of Science and Higher Education.

## REFERENCES

- [1] Miller M., Narkiewicz J., Kania W., Czechyra T., "The Application of Helicopter Rotor Blade Active Control Systems for Noise and Vibration Reduction and Performance Improvement", „Transactions of the Institute of Aviation”, Vol. 184 - 185, pp. 164 – 180, Warsaw 2006.

MAREK MILLER

**SEGMENT ŁOPATY Z KLAPKĄ NA KRAWĘDZI SPŁYWU  
STEROWANĄ PIEZOSIŁOWNIKIEM W DYNAMICZNYCH  
POMIARACH CIŚNIENIOWYCH**

*Streszczenie*

Artykuł podsumowuje całość dotychczasowych działań w zakresie projektowania segmentu łopaty wirnika z klapką na krawędzi spływu, sterowaną przez siłownik piezoceramiczny, używanego w dynamicznych pomiarach ciśnienia w tunelu aerodynamicznym T-1 Instytutu Lotnictwa. Zaprojektowany w oparciu o profil ILH412M-S segment łopaty wirnika będzie wykorzystywany w celu wyznaczenia obciążeń aerodynamicznych w przepływie dwuwymiarowym zgodnie z założeniami projektu badawczego "Badania aktywnego sterowania opływem łopaty wirnika nośnego przy pomocy oscylacji kłapy i mikroklapki w celu poprawy osiągnięć aeromechanicznych śmigłowca".

## THE NUMERICAL ANALYSIS OF PROPERTIES OF THE TRAILING-EDGE FLAP ON THE ILH412M-S ROTOR BLADE AIRFOIL

MAREK MILLER, WIĘCZYŚŁAW STALEWSKI

*Institute of Aviation*

### Abstract

*This paper summarise initial activities concerning the design of the segment of rotor blade with a trailing-edge flap actuated by Amplified Piezo Actuator used in dynamic pressure measurements in T-1 low-speed wind tunnel of the Institute of Aviation.*

*This paper is focused on the design process of the shape of the trailing-edge flap on a rotor blade segment, based on the ILH412M-S profile.*

*After this initial step in design of the rotor blade segment it will be used to derive aerodynamic loads in a two-dimensional flow according to assumptions of the research project "Research on the active control of the airflow of helicopter rotor blade with the use of a flap oscillation and a microflap to improve aerodynamic performance of a helicopter" [1].*

### INTRODUCTION

The main part of the project "Research on the active control of the airflow of helicopter rotor blade with the use of a flap oscillation and a microflap to improve aerodynamic performance of a helicopter" (grant No. N 509 003 31/0251) is focused on the helicopter rotor blade segment with active control system used to deflections of the trailing-edge flap (TEF). The ILH412M-S profile, designed in the Institute of Aviation, was chosen for that segment of 480 mm (initially 440 mm) of chord and 1000 mm of span. The deflection of TEF modifies the airflow around the blade which cause changes of the aerodynamic performance of the rotor and the whole helicopter. The TEF deflection is achieved as the result of the deformation of Amplified Piezo Actuator (APA) which is connected with TEF by the mechanical system of lever and tappet. APA1000XL-SG piezo actuator by CEDRAT was chosen not only as the source of force and strain but also as the source of information about a strain (and the TEF deflection after calculations) [2, 3].

### 1. DESIGN PROCESS OF THE ILH412M-S AIRFOIL

Before the designing process in which properties of the TEF had been chosen, the initial analysis of aerodynamic properties of the ILH412M-S airfoil has been done in the Institute of Aviation.

This analysis was connected with another project carried out by the Institute of Aviation and PZL Świdnik to design new rotor blades for helicopter main rotor for W-3 Sokół helicopter.

One of airfoils calculated numerically in that project was ILH412M-S. It was later chosen for rotor blades of helicopter main rotor. Because one of assumptions of this project was to use the airfoil of the real W-3 main rotor blade, it was chosen as the basis for further analysis and modifications.

In the initial stage [4] the numerical analysis of ILH412M-S was made and aerodynamic characteristics were derived using AMI MSES and ANSYS FLUENT CFD software. Aerodynamic characteristics of ILH412M-S for various Mach numbers are presented in Figures 1 and 2.

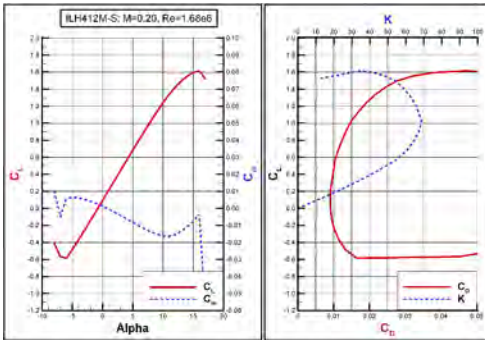


Fig. 1a. Aerodynamic characteristics of ILH412M-S for M = 0.20 (from CFD)

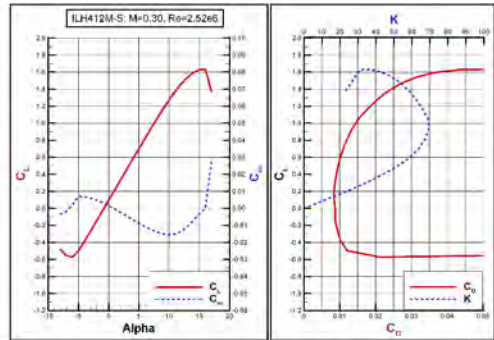


Fig. 1b. Aerodynamic characteristics of ILH412M-S for M = 0.30 (from CFD)

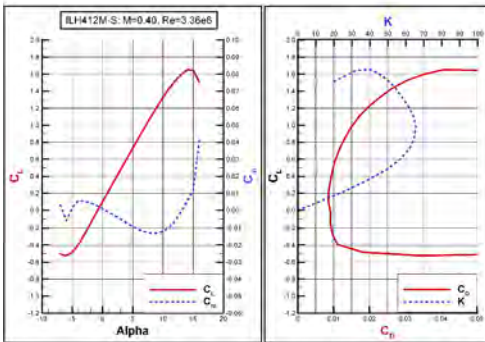


Fig. 1c. Aerodynamic characteristics of ILH412M-S for M = 0.40 (from CFD)

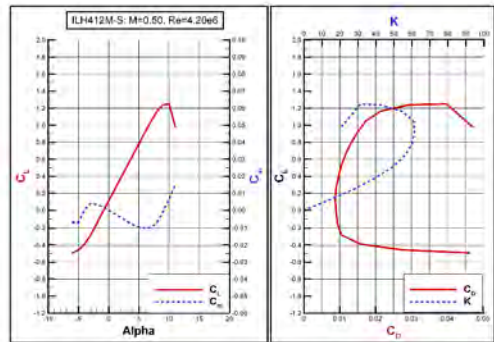


Fig. 1d. Aerodynamic characteristics of ILH412M-S for M = 0.50 (from CFD)

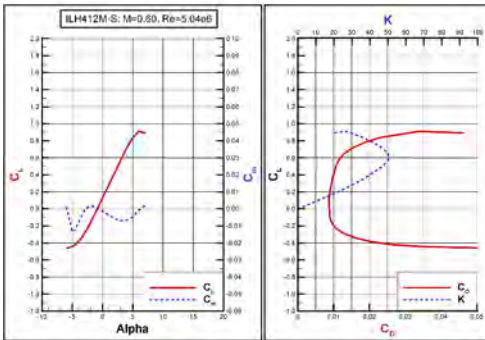


Fig. 1e. Aerodynamic characteristics of ILH412M-S for M = 0.60 (from CFD)

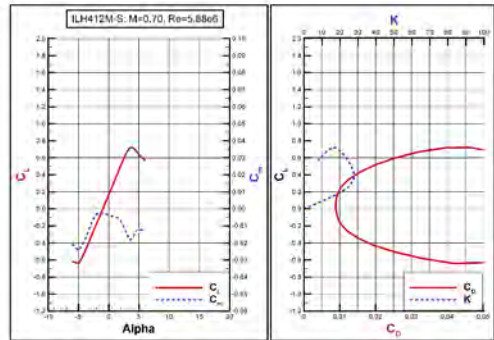


Fig. 1f. Aerodynamic characteristics of ILH412M-S for M = 0.70 (from CFD)

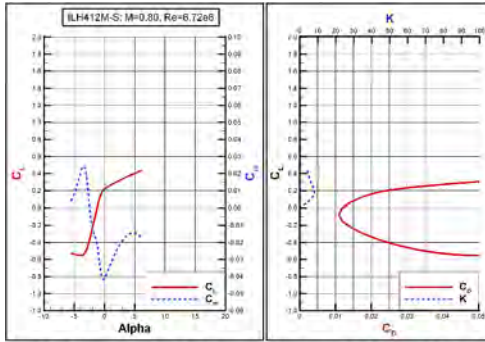


Fig. 1g. Aerodynamic characteristics of ILH412M-S for M = 0.80 (from CFD)

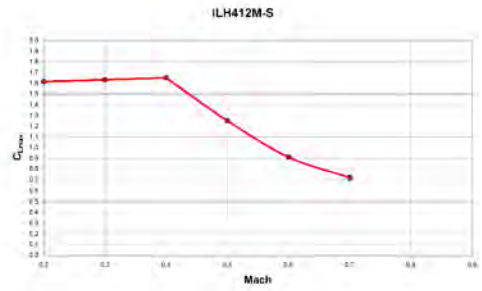


Fig. 2. C<sub>Lmax</sub> for various Mach numbers for ILH412M-S (from CFD)

In the next stage [5, 6] wind tunnel tests of ILH412M-S were made in the N-3 trisonic wind tunnel of the Institute of Aviation (Fig. 3) to prove results of CFD calculations of aerodynamic characteristics made earlier in [4]. For these tests ILH412 airfoil model of chord of 200 mm was prepared (Fig. 4).



Fig. 3. ILH412 airfoil in N-3 wind tunnel

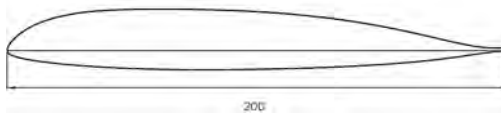


Fig. 4. The geometry of ILH412 airfoil model of chord of 200 mm

Aerodynamic characteristics of ILH412M-S for various Mach numbers are presented in Figures 5 and 6.

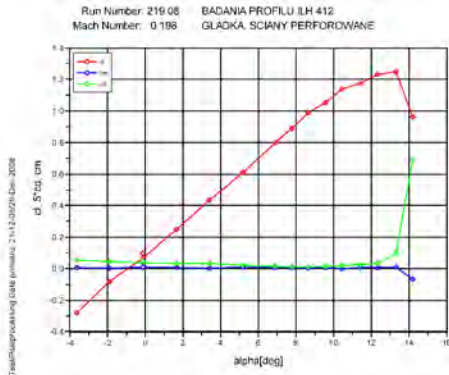


Fig. 5a. Aerodynamic characteristics of ILH412M-S for  $M = 0.20$  (from N-3 wind tunnel tests)

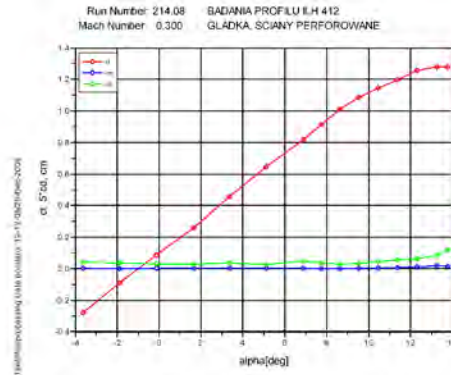


Fig. 5b. Aerodynamic characteristics of ILH412M-S for  $M = 0.30$  (from N-3 wind tunnel tests)

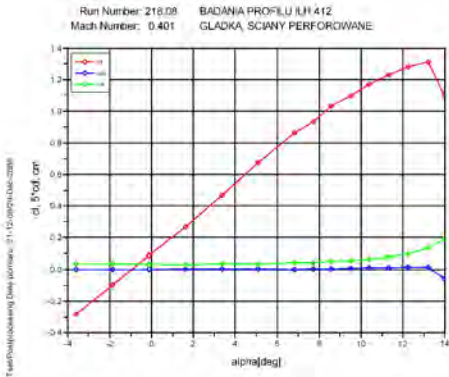


Fig. 5c. Aerodynamic characteristics of ILH412M-S for  $M = 0.40$  (from N-3 wind tunnel tests)

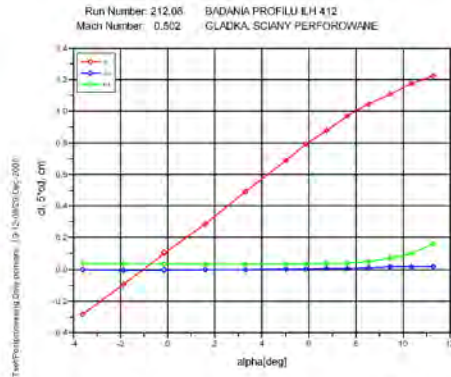


Fig. 5d. Aerodynamic characteristics of ILH412M-S for  $M = 0.50$  (from N-3 wind tunnel tests)

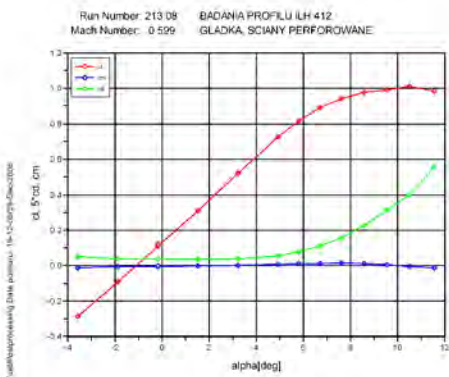


Fig. 5e. Aerodynamic characteristics of ILH412M-S for  $M = 0.60$  (from N-3 wind tunnel tests)

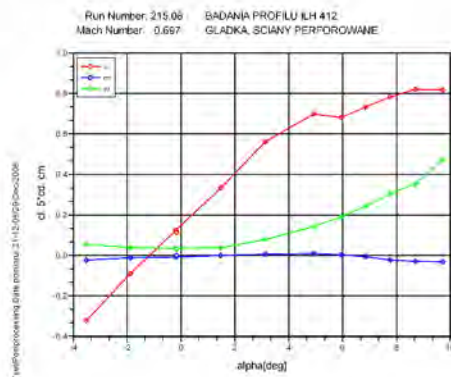


Fig. 5f. Aerodynamic characteristics of ILH412M-S for  $M = 0.70$  (from N-3 wind tunnel tests)

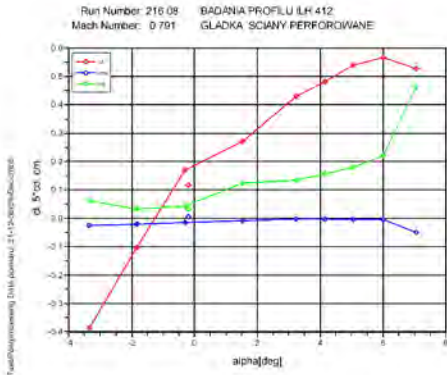


Fig. 5g. Aerodynamic characteristics of ILH412M-S for  $M = 0.80$  (from N-3 wind tunnel tests)

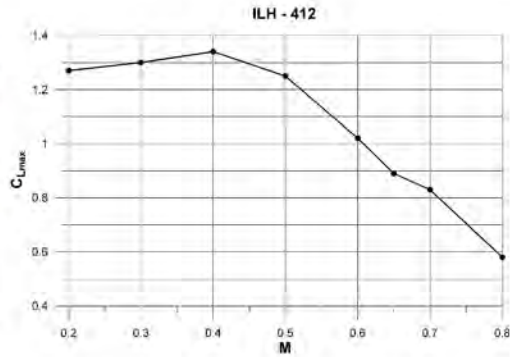


Fig. 6.  $C_{Lmax}$  for various Mach numbers for ILH412M-S (from N-3 wind tunnel tests)

DESIGN PROCESS OF THE ILH412M-S AIRFOIL WITH THE PIEZOACTUATED TEF

In the beginning of the design process of a helicopter rotor blade segment with active control system used to deflections of the TEF, numerical calculations in ANSYS FLUENT flow modelling software were made [7].

In the initial phase it was assumed that the chord of ILH412M-S is 440 mm, a thickness is 12%, an aerodynamic centre (AC) is in 25% of chord from the nose. The pitching axis of the airfoil where the angle of attack is calculated is set in AC.

Three lengths of the TEF were taken into consideration – 10%, 15% (Figure 7) and 20% of the airfoil chord – with hinges at 90%, 85% and 80% of the chord from the nose, respectively.



Fig. 7. ILH412M-S airfoil with 15% TEF

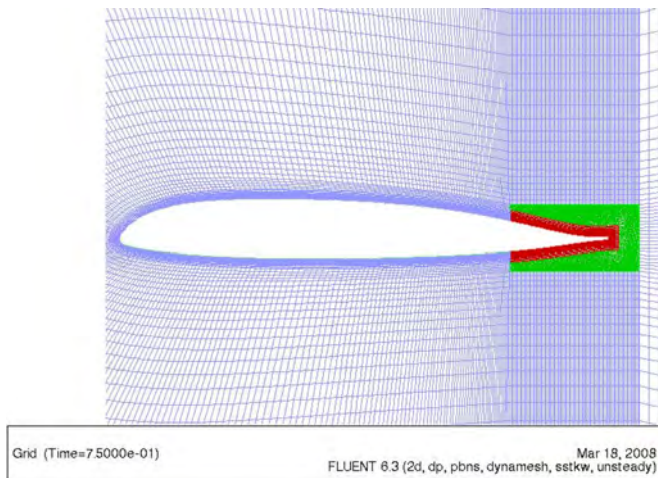


Fig. 8. The grid of ILH412M-S for CFD

In numerical calculations of aerodynamic loads oscillations of the angle of attack of the airfoil, oscillations of the deflection of the TEF and pulsations of the airflow speed resulting from a forward velocity of a helicopter were assumed. The grid for CFD calculations (Figure 8) was designed with the possibility of the modification of the position of the TEF to simulate the oscillation of the TEF.

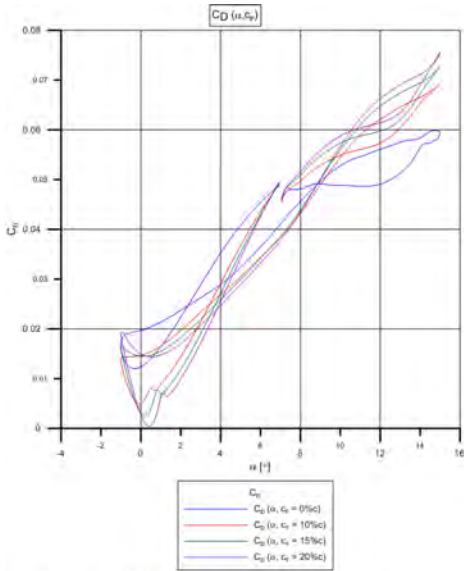


Fig. 9a.  $C_D (\alpha)$  for various chords of TEFs

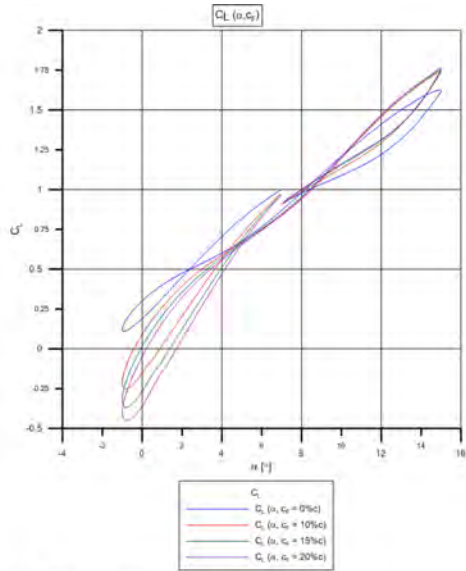


Fig. 9b.  $C_L (\alpha)$  for various chords of TEFs

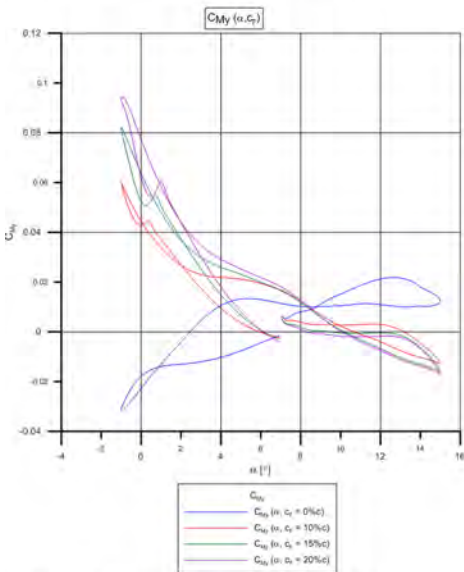


Fig. 9c.  $C_{M_y} (\alpha)$  for various chords of TEFs

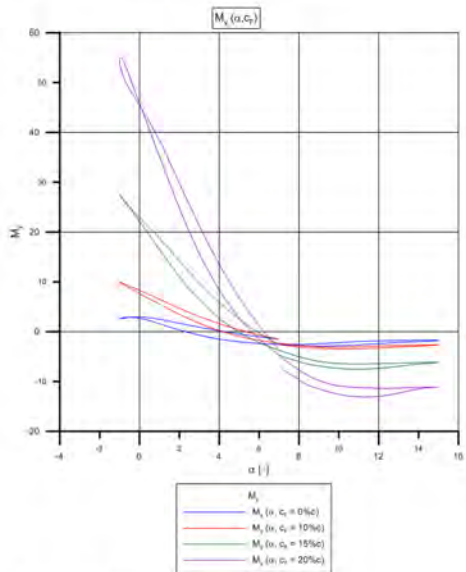


Fig. 9d.  $M_y (\alpha)$  for various chords of TEFs

For numerical calculations it was assumed that the angle of attack oscillates in the range from  $-1^\circ$  to  $15^\circ$  (the amplitude is  $16^\circ$ ). The TEF oscillates in the range from  $-5^\circ$  to  $5^\circ$  (the amplitude is  $10^\circ$ ). The frequency of the cyclic pitch is 4.25 Hz. CFD calculations were made for

Mach number  $Ma = 0.60$  with pulsations of  $\pm 0.15$ . In position where the angle of attack of the airfoil was minimal Mach number was  $Ma = 0.75$  and where the angle of attack of the airfoil was maximal Mach number was  $Ma = 0.45$ . Aerodynamic coefficients  $C_D$ ,  $C_L$ ,  $C_{M_y}$  and moment  $M$  calculated for above parameters are presented in Figure 9.

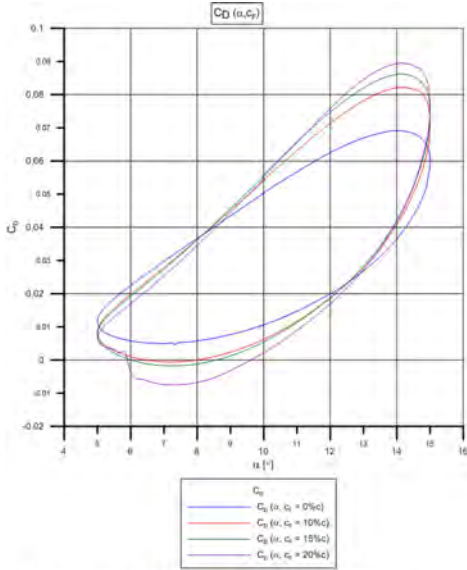


Fig. 10a.  $C_D (\alpha)$  for various chords of TEFs

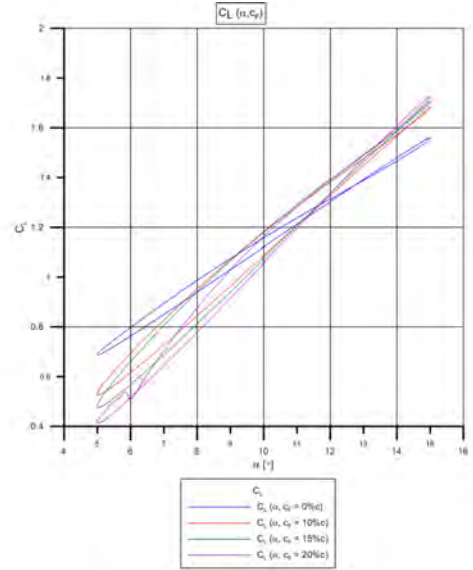


Fig. 10b.  $C_L (\alpha)$  for various chords of TEFs

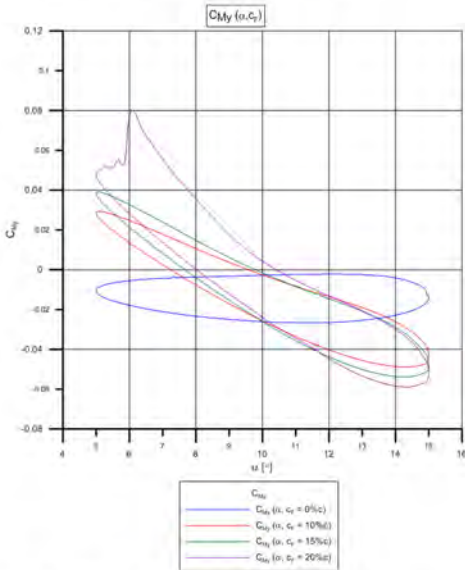


Fig. 10c.  $C_{M_y} (\alpha)$  for various chords of TEFs

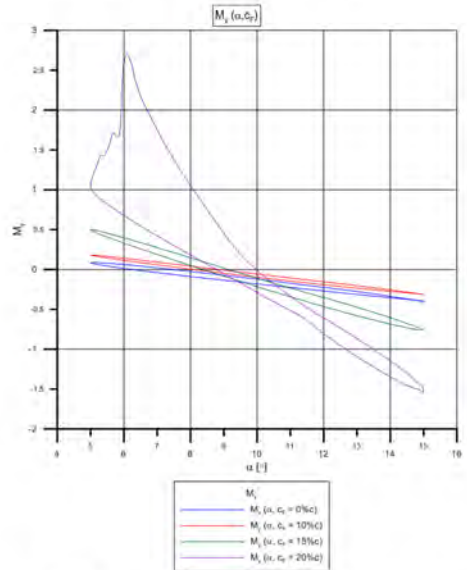


Fig. 10d.  $M_y (\alpha)$  for various chords of TEFs

In further CFD calculations values of the angle of attack were changed. It was assumed that the angle of attack oscillates in the range from  $5^\circ$  to  $15^\circ$  (the amplitude is  $10^\circ$ ). Aerodynamic coefficients  $C_D$ ,  $C_L$ ,  $C_{M_y}$  and moment  $M$  calculated for modified parameters are presented in Figure 10.

Results of CFD calculations obtained from the analysis confirmed the available literature and R&D works of helicopter manufacturers concerning the highest efficiency of 15% chord length the TEF. For this size of the TEF the aerodynamic lift coefficient increases by about 0.1 for flap deflection  $\pm 5^\circ$  to the profile of undeflected flap (for 20% TEF the growth is slightly higher). The aerodynamic coefficient of pitching moment for 15% TEF deflected at  $10^\circ$  is slightly higher in a comparison to the undeflected TEF and is two times smaller than the 20% TEF deflected at the same angle. Forces (approximately 95 N) and moments obtained in CFD calculations in the TEF hinge axis required for TEF deflections could be obtained by APA1000XL-SG piezoactuator by CEDRAT TECHNOLOGIES without any problems at the desired angle of the TEF (the maximum force generated by the actuator is 745N).

## CONCLUSIONS

The designed, 15% of chord, trailing-edge flap on the ILH412M-S rotor blade airfoil will be used to derive aerodynamic loads in a two-dimensional flow in the T-1 low speed wind tunnel, for further numerical analysis of the aerodynamic performance of a helicopter.

## ACKNOWLEDGEMENT

This paper is the result of activities which have been carried out in the research project "Research on the active control of the airflow of helicopter rotor blade with the use of a flap oscillation and a microflap to improve aerodynamic performance of a helicopter" (grant No. N 509 003 31/0251) funded by Polish Ministry of Science and Higher Education.

## REFERENCES

- [1] Miller M. "Rotor Blade Segment with Piezoactuated Trailing-Edge Flap for Dynamic Pressure Measurements", „Transactions of the Institute of Aviation”, ISSN 0509-6669, Vol. 218, pp. 54– 62, Warsaw 2011.
- [2] Miller M., Narkiewicz J., Kania W., Czechyra T., "The Application of Helicopter Rotor Blade Active Control Systems for Noise and Vibration Reduction and Performance Improvement", „Transactions of the Institute of Aviation”, ISSN 0509-6669, Vol. 184 – 185, pp. 164 – 180, Warsaw 2006.
- [3] Miller M. "Research on the active control of the airflow of helicopter rotor blade with the use of a flap oscillation and a microflap to improve aerodynamic performance of a helicopter" (in Polish), Report of the Institute of Aviation No. 10/BA-A1/11/P, Warsaw 2011.
- [4] Stalewski W., "Numerical Analysis of Steady Aerodynamic Characteristics of Helicopter Airfoils of the ILH4xx Family" (in Polish), Report of the Institute of Aviation No. 14/BA/08/P (Appendix A6), Warsaw 2008.
- [5] Krzysiak A., "Experimental Wind Tunnel Tests of Aerodynamic Characteristics of the ILH412 Airfoil in N-3 Wind Tunnel" (in Polish), Report of the Institute of Aviation No. 23/BA1/08/P, Warsaw 2008.
- [6] Krzysiak A., Stalewski W., Czechyra T., "The Experimental Verification of the Numerical Aerodynamic Design of a Helicopter Main Rotor" (in Polish), Report of the Institute of Aviation No. 24/BA-A1/10/A, Warsaw 2010.
- [7] Paluszek Ł., "Numerical Design of Dynamic Flow around the Airfoil of Modifying Geometry" (in Polish), Interim Thesis No.2, Department of Mechanics, Energetics and Aeronautics, Warsaw University of Technology, Warsaw 2008.

MAREK MILLER, WIĘNCZYŚLAW STALEWSKI

## NUMERYCZNA ANALIZA WPŁYWU KLAPKI NA KRAWĘDZI SPŁYWU ŁOPATY WIRNIKA NOŚNEGO ŚMIGŁOWCA O PROFILE ILH412M-S

### Streszczenie

*Dokument ten podsumowuje wstępne działania dotyczące projektowania segmentu łopaty wirnika nośnego śmigłowca z wychylaną klapką na krawędzi spływu sterowaną siłownikiem piezoelektrycznym stosowanego w dynamicznych pomiarach ciśnienia w tunelu aerodynamicznym małej prędkości T-1 Instytutu Lotnictwa.*

*Niniejszy dokument koncentruje się na procesie projektowania kształtu klapki na krawędzi spływu segmentu łopaty wirnika o profilu ILH412M-S.*

*W wyniku działań opisanych w tym dokumencie zostanie zaprojektowany segment łopaty wirnika (w oparciu o profil ILH412M-S), który będzie wykorzystywany w celu wyznaczenia obciążeń aerodynamicznych w przepływie dwuwymiarowym zgodnie z założeniami projektu badawczego "Badania aktywnego sterowania opływem łopaty wirnika nośnego przy pomocy oscylacji kłapy i mikroklapki w celu poprawy osiągnięć aeromechanicznych śmigłowca". [1].*

## VIBRATION TESTING OF A HELICOPTER MAIN ROTOR COMPOSITE BLADE

MACIEJ PARAFINIAK, PAWEŁ SKALSKI

*Institute of Aviation*

### Abstract

*The research presented in this paper focuses on a composite structure test. The object of the investigation is a blade from main rotor of the IS-2 helicopter. The basic methodology which is used is the Experimental Modal Analysis (EMA). The EMA technique is an established tool for the identification of dynamic properties of structure. Based on the experimental data collection, dynamic properties of a research object were estimated. The modal parameters have been estimated using PolyMAX – module of LMS Test.Lab software.*

### INTRODUCTION

There is a need to improve the characteristics of helicopter blades, accompanied by dynamic loads. Application of new methods for testing the dynamic susceptibility can divide a complex system into simpler components, allowing to analyze the impact of changes in susceptibility of individual items on the general characteristics of complex vibration system and the selection parameters of the system during its formation.

Modal analysis is a widely used technique in practice, the study of dynamic properties of the structure. As a result of modal analysis the modal model is obtained as a set of frequencies own form of vibration and damping coefficients. Knowing these parameters allows the prediction of the behaviour of an object due to any imbalances.

Modes are used as a simple and efficient means of characterizing resonant vibration. Resonant vibration is caused by an interaction between the inertial and elastic properties of the materials within a structure.

The research presented in this paper focuses on composite structure tests. The basic methodology which is used is the Experimental Modal Analysis (EMA). The EMA technique is an established tool for the identification of dynamic properties of structures.

As in most practical applications of modal analysis is required for multi-channel experiment and the complex calculations associated with the processing of measured signals and estimation of model parameters. The first application of the method of modal analysis has already been documented in the late 40's, and their rapid development occurred in the 80's, due to the development of computer techniques.

In the present study performed a computer-aided measurement and subsequent analysis were used LMS Test.Lab software. LMS Test.Lab offers a complete portfolio for noise and vibration testing, including solutions for acoustic, rotating machinery, structural testing, environmental testing, vibration control, reporting and data management.

The software naturally follows the test campaign process, guiding for measurement and analysis parameters. It includes a lot of different modules, which are useful in a computer-aided design (CAD), like, LMS Test.Lab Geometry and LMS Test.Lab Modification Prediction. LMS Test.Lab Geometry provides fast wireframe generation and full 3D visualization of test and analysis results. Point coordinates are defined in Excel-like tables, while connections and surfaces are graphically defined in the display. The geometry can be copy/pasted. LMS Test.Lab Modification Prediction evaluates structural modifications (mass, stiffness and damping). Based on the modal model and on the modification element definition, a modal of the structure can be calculated. The effect of such a set of modifications on a modal model can be calculated and compared to the original situation.

## 1. RESEARCH OBJECT

The object of the investigation is a blade from main rotor of the IS-2 helicopter presented in a work stand (Fig. 1). The blade is made of a composite material. Dimensions of the investigated object are: length 3,25 [m], width 0,20 [m]. Approximate weight of the structure is 12,60 [kg].

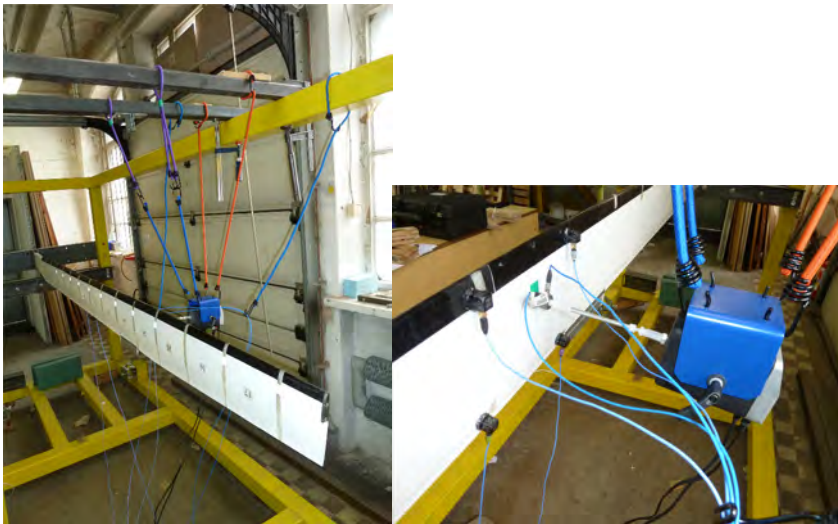


Fig. 1. Test setup of a blade from main rotor of the IS-2 helicopter

In a test campaign the following measurement and analysis tools were used:

- 1 main rotor composite blade of the IS-2 helicopter .
- 1 electromagnetic shaker, with impedance heads incorporating acceleration and force sensor in the same housing to measure reference point FRF's.
- 4 triaxial modal piezoelectric accelerometers PCB.
- 16 channels in fronted LMS SCADAS Mobile with computer a Test.Lab acquisition and analysis suite.
- Bandwidth 128 [Hz], resolution 0,05 [Hz].

The shaker was attached to the structure using a stinger (long slender rod), so that the shaker will only impact force to the structure along the axis of the stringer, the axis of force measurement.

A dense grid of measurement points is defined all over the blade surface, in order to successfully identify the dynamic properties of this structure. Measurement points are set with distance of 0,20 [m] one from each other in the spanwise (X) direction and 0,20 [m] in the edge-wise direction (Z). Geometry definition for blade is presented on Fig. 2. It consists of 39 points, 38 of which are acquisition locations and the remaining 1 is the reference point.

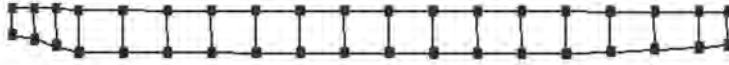


Fig. 2. Cartesian coordinate system for piezoelectric sensors in LMS Test.Lab Geometry

## 2. EXPERIMENTAL RESULTS AND ANALYSIS

The measurement was done in “sets” which means not all the points were measured at the same time. As a consequence a number of partial modal models were estimated for each of the set. Next the partial models were merged into a global model by means of multi-run modal synthesis. Modal models have to be validated to provide confident information about the structural dynamics of a research object.

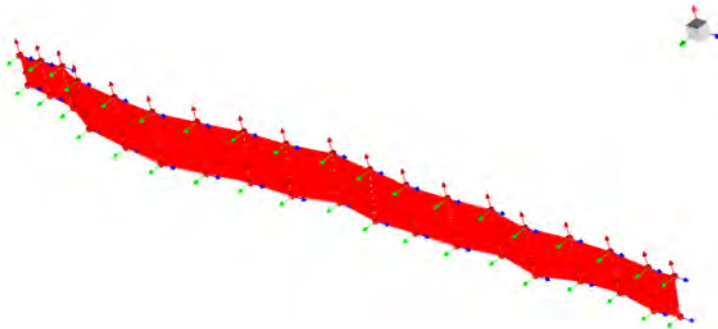


Fig. 3. View of measured blade in LMS Test.Lab Geometry

Due to a high number of measurement points and limited number of piezoelectric sensors applied to the structure (in order to reduce the mass loading phenomena), a large number of test was carried out. Random signal were applied.

Based on the experimental data collection, modal models were estimated. The modal parameters have been estimated using PolyMAX (Polyreference Modal Analysis eXtended) algorithm provided by LMS software. Fig. 4 presents a window of PolyMAX in LMS Test.Lab.

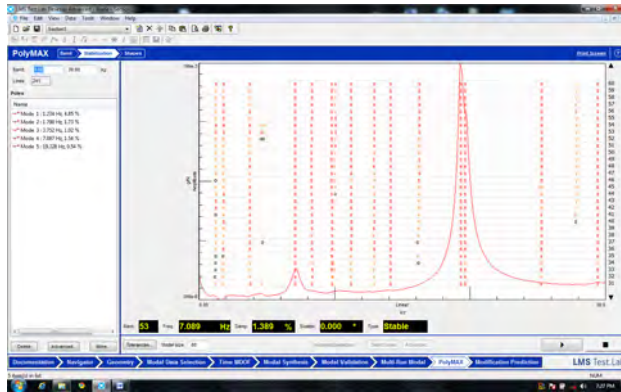


Fig. 4. Window of a stabilization diagram in LMS Test.Lab PolyMAX

PolyMAX is an advanced modal parameter estimation technique that offers superior identification of modal parameters. Its main advantage consists in damped structure identification, where more modes can be identified into a higher frequency range.

During results analysis, the experimental natural modes and damping were estimated: flapwise 2<sup>nd</sup> – frequency 7,0 [Hz] and damping 1,54 %; flapwise 4<sup>th</sup> – frequency 19,0 [Hz] and damping 0,54 %; cordwise 1<sup>st</sup> – frequency 34,4 [Hz] and damping 0,44 %; torsion 1<sup>st</sup> – frequency 43,0 [Hz] and damping 0,60 %.

Visual inspection of the mode shapes is presented on Fig. 5, in this case its present the flapwise 2<sup>nd</sup>.

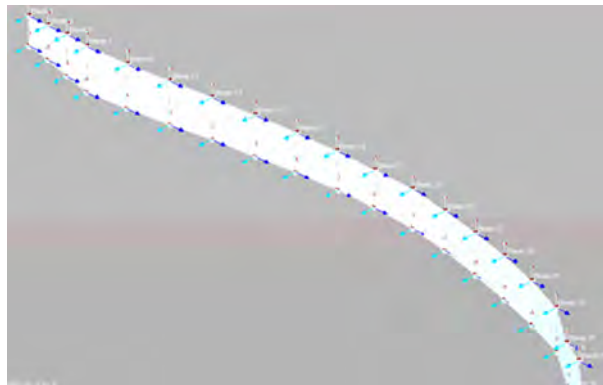


Fig. 5. Identified flapwise 2nd

Using LMS Test.Lab Modification Prediction we can change i.e. a mass of the blade in this case. We change the mass and we change the modal modes. A comparison between blade with additional mass and regular blade mass is presented on Fig. 6.

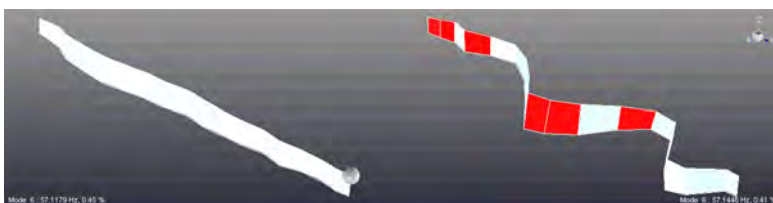


Fig. 6. Mass modification of blade in LMS Test.Lab Modification Prediction

## CONCLUSIONS

This paper presents some aspects of the multidisciplinary and interdisciplinary research oriented for the test data variability. It was presented a test campaign lead on the composite material main rotor helicopter blade. Test setup include measurement technique of contact type. Experimental test data examples are shown and used for modal models estimation.

The dynamic characterization of the blade is particularly complex as the impact of the weight of sensors and instrumentation (cables, mounting of exciters) can distort the results.

Varying mass loading or constraint effects between partial measurements may determine several errors on the final conclusions. Mass loading effect from adding piezoelectric accelerometers and instrumentation should be analysed in next tests, thought a comparison between the mentioned contact and non-contact measurement techniques (i.e. laser vibrometer).

## REFERENCES

- [1] Ewins D.J.: Modal testing: theory, practise, and application, Research Studies Press, Baldock, 2000, pp. xiii, 562.
- [2] Luczak M., Dziedziech K., Vivolo M., Desmet W., Peters B.: Contact versus non-contact of a helicopter main rotor composite blade, AIP Conf. Proc., vol. 1253, 2010, pp. 352-360.
- [3] Heylen W., Lammens S., Sas P.: Modal analysis theory and testing, Katholieke Universiteit Leueven, Department Werktuigkunde, 1998.
- [4] LMS Company – marketing materials.

MACIEJ PARAFINIAK, PAWEŁ SKALSKI

## **PRÓBY WIBRACYJNE KOMPOZYTOWEJ ŁOPATY WIRNIKA ŚMIGŁOWCA**

### *Streszczenie*

*Badania przedstawione w pracy odnoszą się do prób struktury kompozytowej. Badany obiekt to kompozytowa łopata wirnika śmigłowca IS-2. Metoda badawcza jaka została użyta w próbach to eksperymentalna analiza modalna (ang. EMA). Technika ta jest uznanym narzędziem do identyfikacji własności dynamicznych konstrukcji. Na podstawie danych eksperymentalnych, własności dynamiczne zostały wyznaczone, za pomocą PolyMAX – modułu programu LMS Test.Lab.*

## POSSIBILITIES OF IMPROVEMENT OF DIRECTIONAL CONTROL EFFECTIVENESS OF FLIGHT GYROPLANE AT HIGH-ANGLE-OF-ATTACK FLIGHT CONDITIONS

WIĘCZYŚŁAW STALEWSKI, JANUSZ SZNAJDER

*Institut Lotnictwa*

### Summary

Several alternative modifications of original design solution of an inverted "V"-tail control surfaces of a light gyroplane are presented. The aim of the modification is improvement of high-angle-of attack directional controllability of the aircraft. The proposed modifications of the all-flying control surfaces include adjustable symmetric inclination of tail surfaces, split-surface version (stabilizer+rudder), split-surface version with additional, central element and more traditional, "H" configuration with one horizontal and two vertical surfaces. All the proposed modifications retain the second function of the tail surfaces – rear undercarriage. Adjusting the symmetric inclination of the tail surfaces allows for maintaining high values of the yaw control derivative up to the value of the fuselage angle of attack of 30°. Potentially unfavourable side-effect of this solution may be the change of pitching moment during such manoeuvre. For this reason this solution should be applied with the split control surface version (stabilizer+rudder) with additional mechanism adjusting the symmetric rudder deflection to the new elevator inclination in order to keep pitching moment constant. The other two options - additional third control surface in the symmetry plane with rudder and more classical "H" configuration of control surfaces are simpler in operation and safer, particularly the "H" configuration with retains high effectiveness of directional control at high fuselage angle of attack, up to 30°. The version with inverted "V" tailplanes and additional, central control surface has limited effectiveness at high angles of attack, due to geometrical and design constrains, limiting the size of the central control surface.

### INTRODUCTION

In contrast to helicopters, gyroplanes do not have powered tail rotors and for yaw control have to rely on the effectiveness of tail control surfaces. In several situations, such as steep, power-off landing approach, the fuselage may reach angles of attack above 20° and in these conditions efficiency of the control surfaces has to be ensured. This could be difficult, due to low speed, interference of the fuselage or other factors, such as non-optimal arrangement of control surfaces. Such factors seriously degrade the effectiveness of an initial version of a dual-role, inverted-V-shaped empennage of a light gyroplane at high angle of attack. In the basic version the surfaces are all-flying, i.e. each one is a single-element surface rotated around its axis

at 20% chord. It has been determined through numerical flow simulation, that at gyroplane angles of attack exceeding  $10^\circ$  a reverse action of the tail surfaces appears. This phenomenon consists in changing of sign of the yawing moment derivative with respect to deflection angle (yaw control derivative) [1],[2]. The originally designed tail is constrained by its assumed additional function as rear undercarriage, which limits the possibility of modification of the contour and dihedral angle of the control surfaces, so only minor changes are possible, or a complete redesign of the rear fuselage is necessary. Several approaches of solving this problem are presented in this paper.

## 1. ALTERNATIVE VARIANTS OF GYROPLANE TAIL

The second function of the tail surfaces leads to fixed values of its dihedral  $-30^\circ$ , and sweep,  $34^\circ$  in the XZ plane (Figure 1). The airfoil applied for the surfaces was NACA 0012 – typical airfoil for such applications.

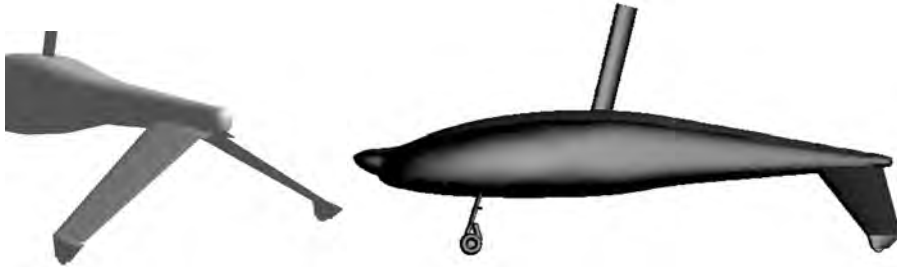


Figure 1. Geometry of the gyroplane fuselage and layout of the all-flying tail surfaces in perspective view

Since the contour of the two control surfaces and their dihedral and sweep angles have been fixed, the allowed modifications of the tail surfaces were as follows:

- introduction of an adjustable symmetrical inclination of the control surfaces (one inclination angle for cruise, another for steep landing approach),
- replacement of the all-flying surfaces by the classic stabilizer-rudder solution,
- addition of another control surface element in the symmetry plane,
- major redesign – application of a classic horizontal and vertical surfaces.

To find out the merits and drawbacks of the proposed modifications numerical flow simulations were performed using the Fluent [3] – (U)RANS solver. The computations were concentrated on determining the values of the yawing moment coefficient derivative due to asymmetric deflection angle  $\partial c_n / \partial \delta_r$ . The range of gyroplane angles of attack was  $0^\circ \div 30^\circ$ . The computations were performed on approximately 2mln-cell meshes using the Spalart-Allmaras turbulence model. The  $y^+$  parameter, defining the height of the nearest to surface cell was equal approximately 30, which is optimal value for the accuracy of viscous flow simulations and total mesh size. The results of the numerical analysis for each geometry variant are presented in the following paragraphs.

## 2. RESULTS OF COMPUTATIONAL ANALYSES

### 2.1 Adjustable symmetric inclination

It was assumed, that the inclination change is performed by the rotation of the basic all-flying control surfaces around an axis in 20% chord (Figure 2). Four values of symmetric inclina-

tion angle were applied:  $0^\circ$  (basic version),  $-20^\circ$ ,  $-25^\circ$  and  $-30^\circ$ . These configurations were the reference configurations for the calculations of yawing moment derivatives. The values of  $\partial c_n / \partial \delta_r$  derivative were computed using the characteristics of the reference configuration and characteristics of configurations with control surfaces deflected by  $+5^\circ$  (nose right – right surface) and  $-5^\circ$  (left surface) from each of the reference configuration. The comparison of the  $\partial c_n / \partial \delta_r$  derivative vs. angle of attack for the investigated configurations is shown in Figure 3.

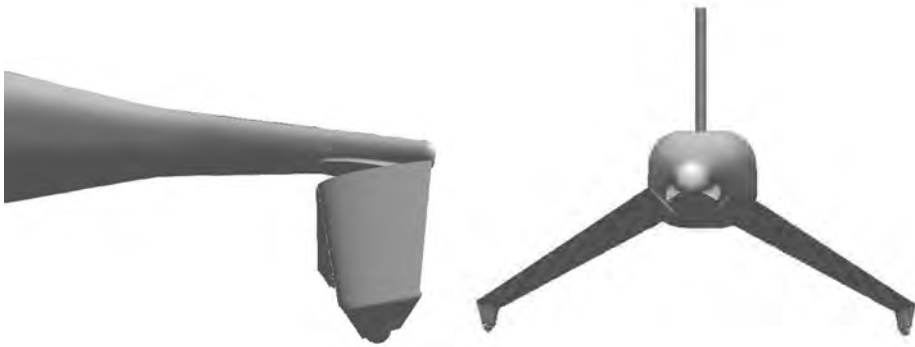


Figure 2. Basic version of all-flying (single-element) tail surfaces with inclination angle set at  $-20^\circ$  - left view and rear view

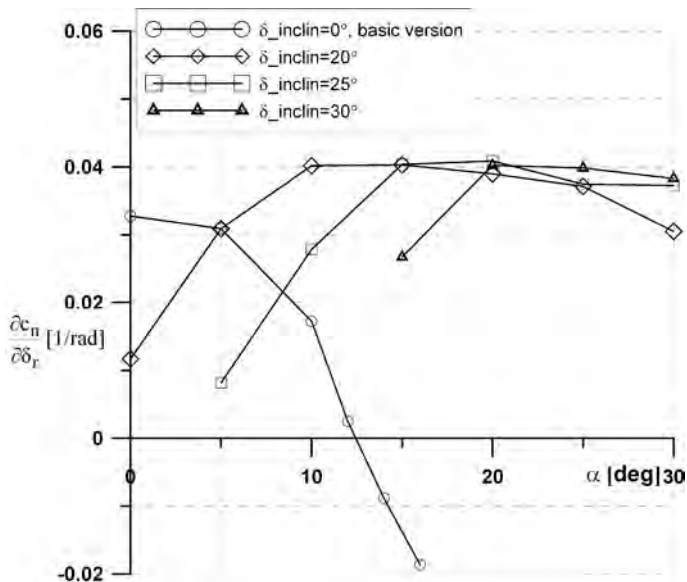


Figure 3. Comparison of  $\partial c_n / \partial \delta_r$  derivative for the basic configuration and configurations with adjustable inclination of tail surfaces

For the basic version of the empennage there occurs a reverse action of the tail surfaces – change of sign of the yaw control derivative  $\partial c_n / \partial \delta_r$ . This is caused by the effect of extensive flow separation on the surface with increasing local angle of attack leading to rapid decrease of local lift force, and relatively lower decrease of local lift or even increase (if the angle of attack of undeflected surface is higher than profile  $\alpha_{CLmax}$ ) on the surface with lower angle of attack. This effect has been explained in detail in [1].

Data presented in Figure 3 show that adjusting the symmetric inclination for manoeuvres such as steep landing approach at high angle of attack allows to retain the necessary directional control during such manoeuvre. There are, however, two drawbacks of this solution if applied to the basic version of all-flying tailplanes. One of them is the necessity of measurement of the fuselage angle of attack in order to change the tailplanes' inclination angle in a proper moment, to avoid the danger of reverse action of the tailplanes, the other is the change of pitching moment caused by the change of the inclination of the tailplanes. This data is shown in Figure 4 for the airspeed of 50 km/h and angle of attack  $10^\circ$ . Change of symmetric inclination of the tailplanes from  $0^\circ$  to  $-10^\circ$  involves change of pitching moment equal 390Nm. This may disturb the longitudinal balance of the gyroplane. For these two reasons the solution of adjustable inclination of the tailplanes is safer to adopt with tailplanes divided into stabilizer and rudder. It is possible to introduce a mechanism of simultaneous change of the stabilizer inclination and rudder deflection in order to keep pitching moment constant during this operation. The characteristics of a split-tailplanes version are shown in the following paragraph.

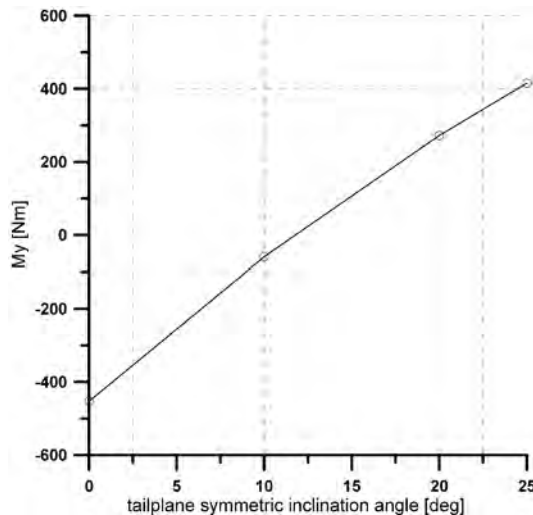


Figure 4. Change of pitching moment due to change of the inclination angle of the tailplanes at fuselage angle of attack of  $10^\circ$  and airspeed of 50 km/h

## 2.2 Split surfaces – stabilizer and rudder

In the Figure 5 the effectiveness of the basic all-flying version of tail surfaces was compared with the results for the split configuration with rudder chord ratio of 70%. The contour of the split surfaces was the same as the contour of the all-flying version. The rudder chord ratio was set based on the results of 2D computations which have shown that maximum value of the lift force for this chord ratio exceeds maximum lift of single-element airfoil, and on structural considerations which allowed for this high value of rudder chord ratio.

As it can be seen in Figure 5, the characteristics of the split control surfaces are safer than characteristics of the basic version, because there is no change of sign of the  $\partial c_n / \partial \delta_r$  derivative at higher fuselage angles of attack, and hence, no reverse action.

The effectiveness of the rudder is, however, at fuselage angle of attack higher than  $16^\circ$  more than three times lower than at angles of attack below  $6^\circ$ . The reason for this is flow separation on upper parts of the tail surfaces which is caused by relatively low absolute value of the dihe-

dral ( $-30^\circ$ ) which forces the tail surfaces to operate at high local angles of attack, above  $\alpha_{CLmax}$ . The reasons of differences in high-angle-of-attack characteristics of these two version have been described more in detail in [1].

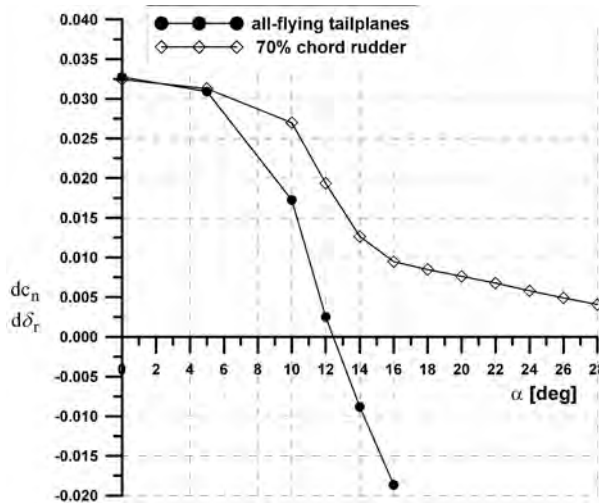


Figure 5. Comparison of the derivative of yawing moment coefficient with respect to rudder deflection for the all-flying tailplanes and the split (stabilizer + rudder) version

### 2.3 Additional vertical, central control surface

With the dihedral of the tail surfaces fixed due to reasons connected with the second function of the tail surfaces, it is possible to add another control surface in the rear fuselage, in the X-Z symmetry plane. This may be an idea worth considering, because in contrast to poor control characteristics at high angles of attack the basic configuration has some advantages at low angles of attack. The inverted "V" surfaces are located in the area of increased flow speed caused by the propeller effect. This improves directional control at low speed and during ground operations. Due to the danger of collision with rotor blades, any additional surface has to be located on the lower side of the fuselage. This, however, restricts its size because the space in this region is limited due to low distance from the rear fuselage to the ground. Taking into account these constraints, such additional control surface has been designed and is shown in Figure 6. The additional surface is designed as a classical vertical tail with rudder rotated around a vertical axis.

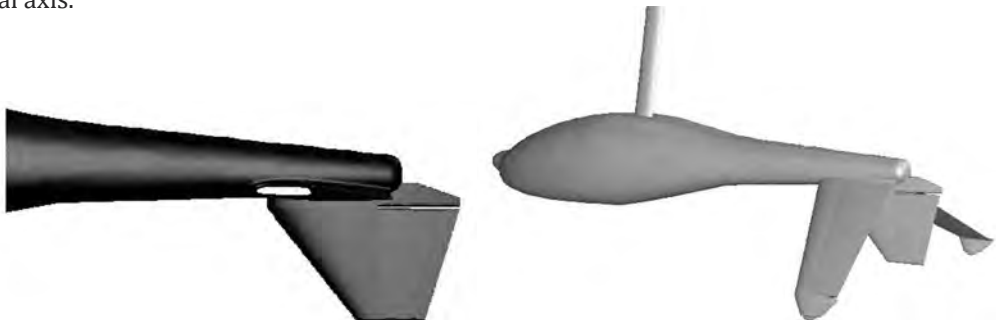


Figure 6 Side view of additional control surface (other two surfaces invisible) and a perspective view of the fuselage version with three control surfaces

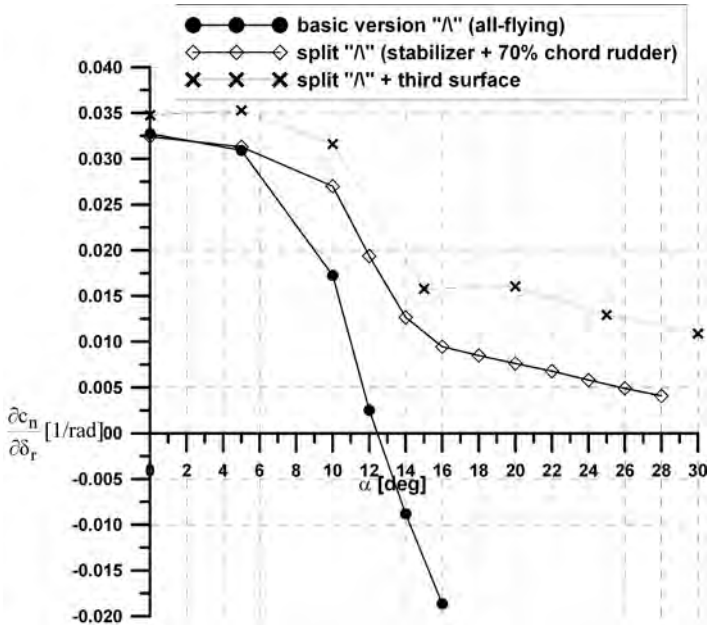


Figure 7 Comparison of the yaw control derivative for the three investigated empennage versions with inverted-V tail surfaces

Data presented in Figure 7 show that the additional tail surface improves the directional control at high fuselage angles of attack. The value of  $\partial c_n / \partial \delta_r$  derivative at  $\alpha_{fus}=20^\circ$  is, however, two times, and at  $\alpha_{fus}=30^\circ$  three times lower than at  $\alpha_{fus}=0^\circ$ . At the same time, the contribution of the third surface to the yaw control derivative at low  $\alpha_{fus}$  is relatively small due probably to the effect of the wake of front part of the fuselage. At higher fuselage angles of attack, above  $20^\circ$ , the central control surface becomes the most effective one. It may be concluded that given the restraints due to the geometry of fuselage and the teetering rotor, the possibilities of significantly improving yaw control effectiveness at high angles of attack by the addition of another surface to the basic version are limited.

#### 2.4. "H-tail" configuration

More significant improvement of directional control at high angles of attack is possible by major redesign of the empennage. Such idea is presented in Figure 8. It consists of the replacement of the two slanted tail surfaces by a more classical configuration, composed of one horizontal and two vertical surfaces. The vertical surfaces are placed in larger part below the horizontal tail, so the second function of the tail surfaces – the rear undercarriage is retained in the design. The span of the horizontal surface is the same as the span of the basic configuration, and so is the distance between the wheels of the rear undercarriage. The surface area of the vertical elements is equal to the surface area of the projections of the slanted "Λ" tail surfaces on the X-Z plane. Rudder chord ratio of the vertical elements is 50%.

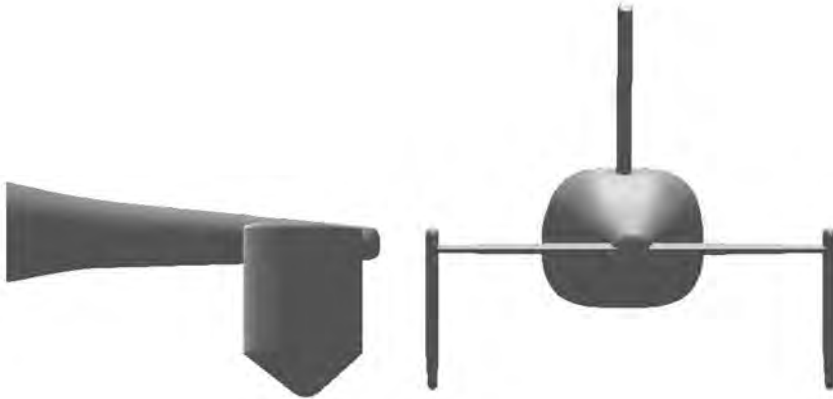


Figure 8. The layout of the proposed "H" configuration of control surfaces

The comparison of the yaw control derivative for the version with fixed “/” tail surfaces and the “H” version is presented in Figure 9. The “H” configuration in comparison with the other versions has very good directional control characteristics at high fuselage angles of attack, the yaw control derivative decreases only by approximately 10% at  $\alpha_{fus}=30^\circ$ . The disadvantages of this version in comparison with the basic one may consist in decreased directional control effectiveness at low speed and on the ground, due to the placement of the vertical elements out of the propeller wake. There is also some increase of drag and mass, because of greater surface area and additional structural connections between elements. However, low fuselage drag in rotorcraft is not as important as in conventional aircraft because of lower flight speeds and another source of drag – rotating blades. The mass increase may also be not much higher in comparison with the other presented modification versions.

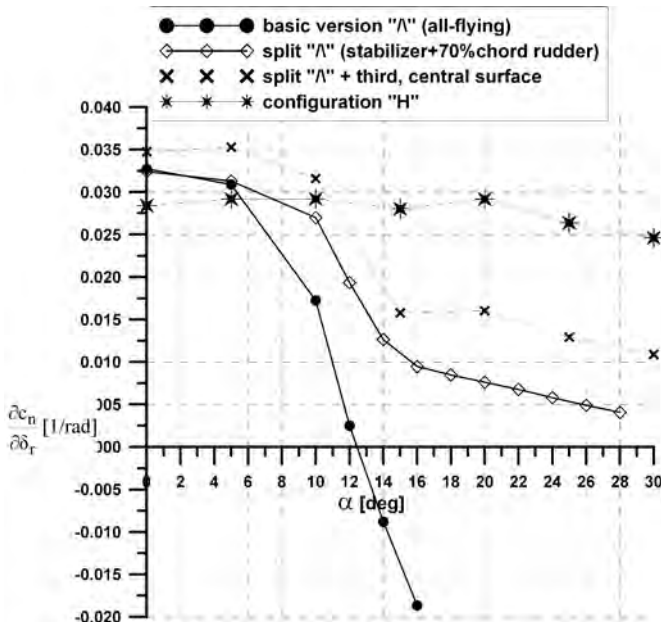


Figure 9. Comparison of the yaw control derivative for the “H” configuration and the three versions with inverted-V tail surfaces

## CONCLUSIONS

The presented modifications of the basic version of the empennage of the light gyroplane were meant to improve unfavourable directional control characteristics of the initial version – sharp decrease and change of sign of the yaw control derivative at high fuselage angles of attack. The most efficient solutions are the introduction of the adjustable symmetrical inclination and redesign replacing the slanted surfaces with classical solution composed of horizontal and vertical surfaces. The first solution seems to be rather complicated due to the change of longitudinal balance during the operation of inclination change. In order to minimise this problem, and to avoid the danger of inverse action at high angles of attack, this solution should be applied with the split tailplane version. For this version an additional mechanism of adjusting the rudder deflection to the inclination angle could be designed, such that would keep the fuselage pitching moment constant. The last solution of replacing the inverted “V” configuration with more classical “H” one seems to be the simplest and most effective, because it ensures high effectiveness of the directional control surfaces over the widest range of angle of attack. The mass increase due to larger surface area and additional structural connections of the “H” configuration may be not higher than for the adjustable inclination of the “V” shaped elevators, if similar safety level should be achieved (high directional control effectiveness, no change of longitudinal balance). The solution with additional control surface is not as effective as the “H” configuration and may require similar mass increase.

## ACKNOWLEDGEMENTS

All computational grids used in calculations presented in this work were created by Adam Dziubiński. The authors of this paper thank him for his effort.

## REFERENCES

- [1] J. Sznajder, Effectiveness of an Inverted-V-Shaped Control Surfaces of a Gyroplane at Low Speed and High Angles of Attack, Transactions of the Institute of Aviation, 2011, Warsaw (in print),
- [2] G. Krysztofiak, Aerodynamic Investigations of a model of fuselage of I-28 gyroplane in 5m-diameter wind-tunnel without propeller effect, Report of Institute of Aviation, Nr 31/BA/1/P/10, Warsaw, 2010 (in Polish)
- [3] Fluent 6.3 User's Guide, Ansys.Inc.

WIEŃCZYŚŁAW STALEWSKI, JANUSZ SZNAJDER

## MOŻLIWOŚCI POPRAWY SKUTECZNOŚCI KONTROLI KIERUNKU LOTU WIATRAKOWCA NA DUŻYCH KĄTACH NATARCIA

### *Streszczenie*

*W pracy przedstawiono kilka alternatywnych modyfikacji wersji wyjściowej usterzenia lekkiego wiatrakowca, płytowego w układzie odwróconego "V". Celem modyfikacji jest poprawa sterowności kierunkowej wiatrakowca na dużych kątach natarcia. Proponowane modyfikacje usterzenia płytowego obejmują przestawialne symetryczne zaklinowanie powierzchni sterowych, wprowadzenie podziału na statecznik i ster, dodanie do wersji usterzenia dzielonego trzeciego, centralnego elementu a także bardziej tradycyjnego układu "H" z jednym, dzielonym usterzeniem poziomym i dwoma dzielonymi powierzchniami pionowymi. Wszystkie proponowane modyfikacje zachowują drugą funkcję usterzenia – funkcję tylnego podwozia.*

*Zmiana symetrycznego zaklinowania powierzchni sterowych pozwala na zachowanie wysokich wartości pochodnej momentu odchylającego względem kąta wychylenia steru do wartości kąta natarcia kadłuba równego  $30^\circ$ . Potencjalnym efektem szkodliwym tego rozwiązania może być zmiana momentu pochylającego w czasie operacji zmiany zaklinowania steru. Z tego powodu takie rozwiązanie powinno być zastosowane z usterzeniem dzielonym na statecznik i ster razem z dodatkowym mechanizmem dopasowującym symetryczne wychylenie steru do nowego kąta zaklinowania statecznika w celu utrzymywania stałego momentu pochylającego. Pozostałe dwa warianty - dodatkowa trzecia powierzchnia sterowa w płaszczyźnie symetrii i klasyczne usterzenie w układzie "H" są prostsze w działaniu i bezpieczniejsze, szczególnie układ "H" który utrzymuje wysoką sterowność kierunkową na dużych kątach natarcia kadłuba, do  $30^\circ$ . Wersja z dwoma powierzchniami w układzie odwróconego "V" i dodatkową, centralną powierzchnią sterową ma ograniczoną skuteczność na dużych kątach natarcia z powodu ograniczeń geometrycznych i konstrukcyjnych, limitujących rozmiar dodatkowej, centralnej powierzchni.*

## EFFECTIVENESS OF AN INVERTED-V-SHAPED CONTROL SURFACES OF A GYROPLANE AT LOW SPEED AND HIGH-ANGLES-OF-ATTACK

JANUSZ SZNAJDER

*Institute of Aviation*

### Abstract

*An inverted-V-shaped control surface configuration has been applied in a design of a light gyroplane. Two variants of the inverted-V-shaped control surfaces have been investigated in the present work: all moving version and stabilizer-rudder solution with 70% chord rudder. The focus of the investigation is on high angle of attack characteristics important for low-speed, short-distance or power-off landing approach.*

### INTRODUCTION

Main benefits of application of a V-shaped tail surface configuration in light aircraft are structural simplicity and savings on manufacture costs. The drawback of this solution is slightly more complicated control system, involving elements making it possible to execute symmetric and asymmetric movements of control surfaces. Similar motivations are important also in application of this type of tail surfaces in the design of a light gyroplane. In a gyroplane the role of the tail surfaces differ slightly from their role in a fixed-wing aircraft. The elevator is no longer the main instrument for longitudinal control, since this action is performed by the deflection of the rotor shaft in the symmetry plane. The elevator may, however, be used for horizontal trim. The horizontal stabilizer plays also an important role in preventing the 'power push-over' phenomenon and damping longitudinal oscillations of the fuselage. The 'power push-over' phenomenon may occur, when rotor angular velocity and lift suddenly decrease and the gyroplane is subject to unbalanced pitching moment from the propeller, if the propeller thrust line is not aligned with the gyroplane C.G (Figure 1). Horizontal tail then significantly reduces pitch velocity, enabling the pilot to react to this situation by deflecting the rotor shaft and changing blade pitch angle, or by supplying the torque to rotor from engine, if possible. The vertical tail is necessary to provide directional stability, as in fixed-wing aircraft. Unlike a fixed-wing aircraft, a gyroplane can safely perform turns without rudder deflection, using instead deflection of rotorhead in the Y-Z plane. The gyroplane then performs a sideslip movement and then the fuselage aligns with the new flight direction due to its directional stability. However, in some phases of flight, such as short-distance landing especially with side-wind, an efficient directional control is necessary for maintaining the direction of flight. Since there is no tail rotor, in contrast

to helicopters, control of the yaw angle must be executed using rudder. For a classical tail-surface system, as well as for the V-shaped tail surfaces the requirements for aircraft controllability at low speed lead to increasing of the control surface area. This is difficult in a gyroplane design, due to the presence of the rotor on a deflectable shaft above the fuselage. One way of dealing with this constraint is the application of an inverted-V-shaped control surfaces. The way of providing high effectiveness of the control surfaces is then the application of all-moving control surfaces, or increasing the rudder surface of a two-element tail surface (elevator + rudder) well above 50 percent of chord. This choice has been investigated in the present work.

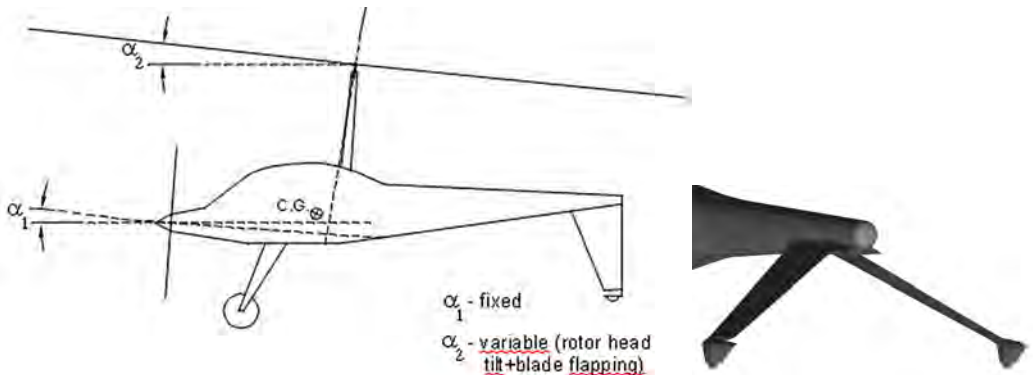


Figure 1. General view of a gyroplane with a tractor-type power system and inverted-V shaped tail surfaces

## Two-dimensional analysis

Two-dimensional analysis was aimed at determination of maximum lift coefficient, and derivatives of lift and hinge moment with respect to angle of rudder deflection for selected configurations which included an all-moving section (single airfoil) and several rudder/airfoil-chord proportions. The airfoil selected was NACA0012 – typical airfoil applied for control surfaces. The airspeed for the test was set at 50km/h, approximately the take-off velocity of a typical light gyroplane. The Reynolds number was set at 608500 which corresponds to tail chord of 0.64m. The detailed proportions of rudder/chord ratio and the positions of the rotation axis of the moving element are shown in Table 1.

Table 1. Geometric data of the investigated rudder-airfoil chord ratios

rudder/chord ratio	$x_{axis}/c$
100% - all moving tail surface	20%
70%	35.926%
60%	45.545%
50%	54.943%

The aerodynamic characteristics of the presented rudder configurations were determined using Fluent solver, using k-omega-SST turbulence model [1,2] on a grid of 24000 elements. The k-omega-SST turbulence model is considered appropriate for modeling of viscous flows at low Reynolds numbers. In the computational grid the main element-rudder junction was sealed. This is a justified procedure for narrow slots in the model, accelerating the convergence of the solution. The computed  $c_L \cdot \delta_{rudder}$  characteristics are shown in Fig. 2.

It follows from Fig. 2 that  $c_{L\max}$  of rudder/airfoil chord ratios greater than 50% are higher than for all-moving control surface. This may be explained by the chordwise distribution of pressure coefficient  $c_p$  over the investigated NACA0012 airfoil. A deflected rudder of rudder/chord ratio more than 50% modifies significantly  $c_p$  distribution in the front part of the airfoil, increasing the length of the low-pressure area (Figures 3 and 4).

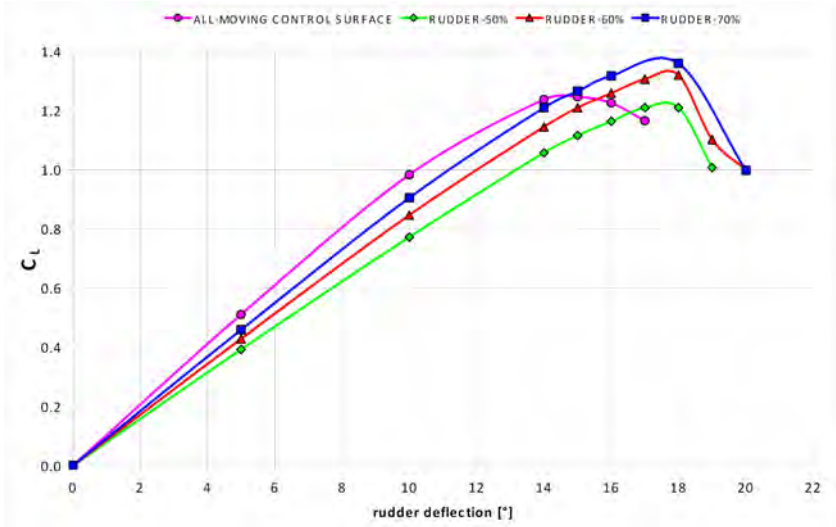


Figure 2.  $C_L - \delta_{\text{rudder}}$  characteristics for different rudder/airfoil chord ratios

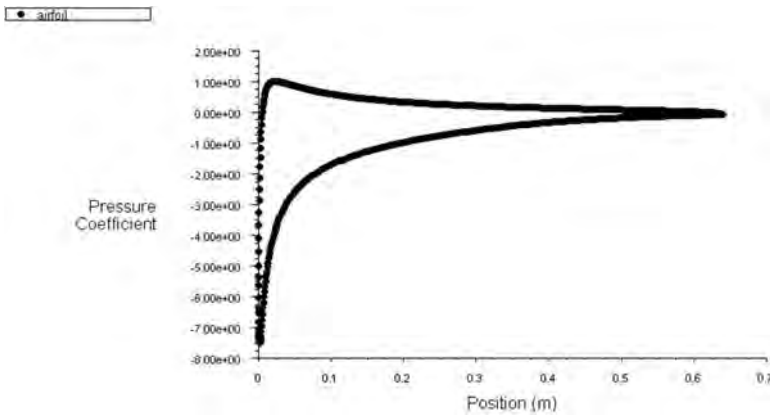


Figure 3. Distribution of pressure coefficient on NACA 0012 airfoil at  $\alpha=14$  deg (near  $\alpha_{CL\max}$ )

As a measure of the effectiveness of a rudder a nondimensional coefficient  $\alpha_\delta$  - angle of attack effectiveness, (ratio of derivatives  $c_{L\alpha}$  and  $c_{L\delta}$ ) is frequently used[3]. This coefficient, determined for the rudder/airfoil chord ratios presented in Table 1 is shown in Fig. 5. The data shows, that rudder/airfoil chord ratios of 60-70% are very effective at generating lift force, producing required lift coefficient at moderately larger deflection angle (10-17%) than all-moving control surface.

This characteristic and others, including  $c_{L\max}$ ,  $\frac{\partial c_{m\text{ hinge}}}{\partial \delta_{\text{rud}}}$ ,  $c_{m\text{ hinge max}}$  are shown in Table 2.

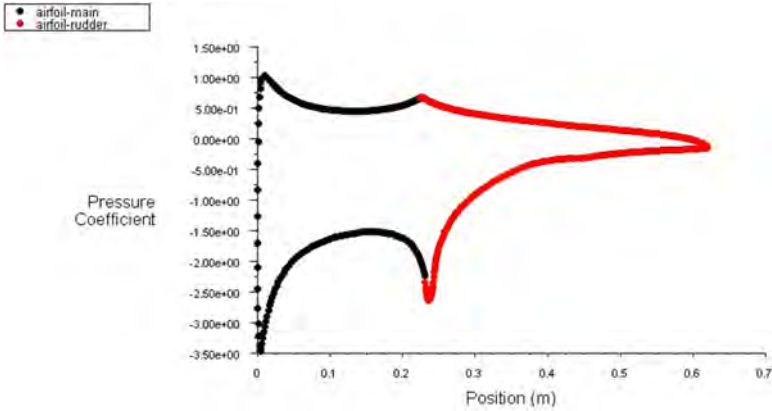


Figure 4. Distribution of pressure coefficient on NACA 0012 airfoil with 70% c rudder at rudder deflection  $\delta_r = 18^\circ$  (near  $\delta_{rCLmax}$ )

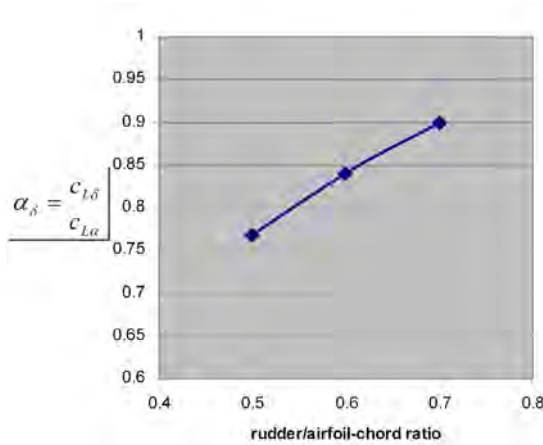


Figure 5. Angle of attack effectiveness for the investigated rudder-airfoil chord ratios

Table 2. Results of two-dimensional flow analysis of the investigated rudder-airfoil chord ratios

rudder/airfoil chord	$x_{axis}/airfoil$ chord	$\delta_{rud/CLmax}$ [°]	$c_{Lmax}$	$\alpha_\delta = \frac{c_{L\alpha}}{c_{L\delta}}$	$\frac{\partial c_{mhinge}}{\partial \delta_{rud}}$	$c_{mhinge max}$
100%	0.20	15	1.242	1.0	-0.275	-0.047
50%	0.549	18	1.218	0.769	-0.147	-0.039
60%	0.455	18	1.321	0.840	-0.234	-0.061
70%	0.359	18	1.360	0.898	-0.357	-0.0898

### THREE-DIMENSIONAL ANALYSIS

#### Low angles of attack, effect of propeller wake

Three-dimensional computations were performed for an all-flying tailplanes with sweep angle in the X-Y plane of  $20^\circ$ , sweep in XZ-plane of  $34^\circ$ , dihedral of  $-30^\circ$ , taper of 0.465, span of 2.94m and surface area of 1.841m<sup>2</sup>. The primary function of the tailpanes is providing direc-

tional stability and controllability in yaw (using antisymmetric deflections with respect to X-Z plane), as well as trim corrections for longitudinal balance (using symmetric deflections with respect to X-Z plane). The secondary function of the tailplanes consists in working as the rear undercarriage.

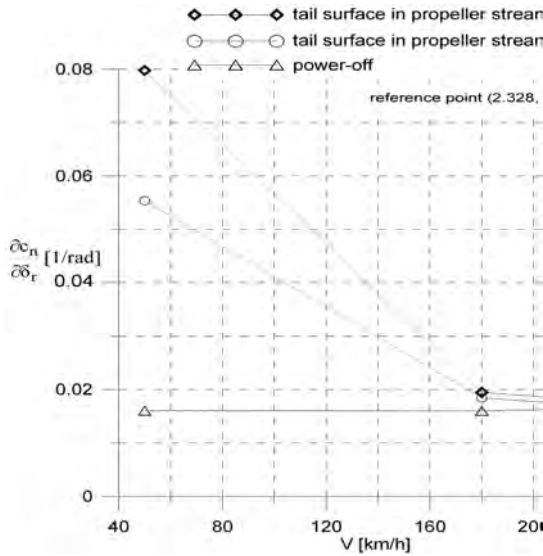


Figure 6. Derivative of yawing moment due to rudder deflection in cruise conditions including effects of propeller stream

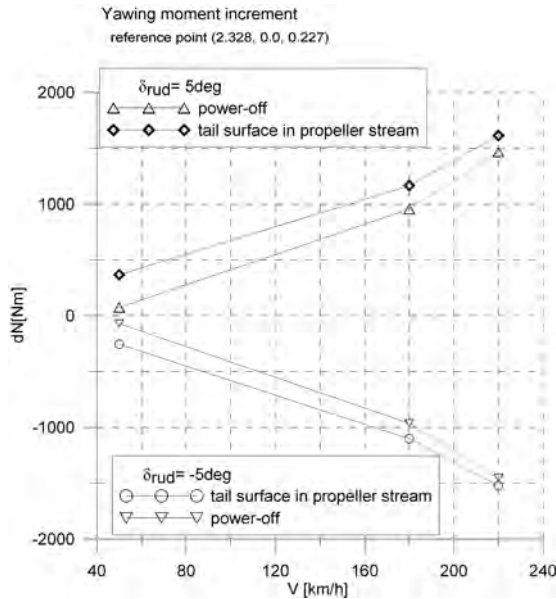


Figure 7. Increment of yawing moment due to rudder deflection in cruise conditions including effects of propeller stream

The basic characteristics expressing the effectiveness of the tail surfaces – derivatives of yawing moment coefficient with respect to the angle of surface deflection and yawing moment

increment due to angle of surface deflection are shown in Figures 6 and 7. The surface deflection angle was  $5^\circ$ . The computations were performed using Fluent solver for cases with and without working propeller. The effect of propeller stream was modeled using the fan boundary condition on the grid zone representing the propeller. The distribution of pressure jump along fan radius and circumferential velocity distribution on the fan surface were set based on simulation of the working propeller using Virtual Blade Model [4]. The propeller thrust was set at 2.2 kN at speed of 50 km/h and 1.47kN at 180 and 220 km/h. It is clearly visible that propeller stream has a favourable effect on the  $c_{n\delta r}$  derivative at low speeds, increasing significantly its value. The large increase of the value of the derivative at low speed is due to the large increase of dynamic pressure in the tail region at low speed. Yawing moment increment in the propeller effect is greater if the rudder is deflected in the direction of the coils of the propeller wake. The distribution of the flow velocity in a vertical plane just ahead of the vertical tail, induced by the propeller for gyroplane standing on the ground, is shown in Figure 8. The distribution is assymmetric, with higher flow velocities around the left element. The propeller thrust was set at 2.2 kN. The aerodynamic coefficients were calculated using as reference the rotor disk surface area and rotor radius equal 4.2m.

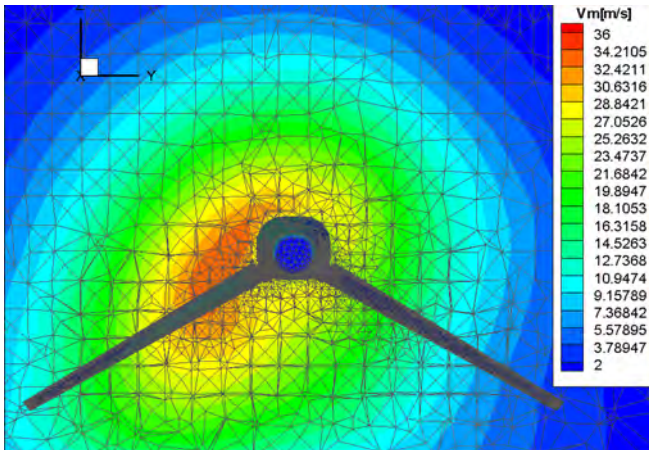


Figure 8. Distribution of propeller axial velocity in a plane just ahead of tail surface root for a gyroplane standing on the ground

### Effectiveness of tail surfaces at high angles of attack

A specific feature of gyroplanes is their ability to perform short-distance landing, executed with steep descent. Such landing is also performed in emergency situations in power-off flight. Because of absence of tail-rotor which ensures directional stability and controllability of helicopters, gyroplanes must rely on the effectiveness of tail control surfaces. Effectiveness of control surfaces must be ensured especially for conditions of low forward speed and high fuselage angles of attack, as these are typical conditions of steep low-speed, power-off landing.

Shown in Figure 9 is the derivative of yawing moment with respect to rudder deflection for the range of fuselage angle of attack from 0 to 16 deg. The computations were performed for the basic design of two all-moving, single-element surfaces. The propeller effect was not included in the computations in order to simulate conditions of power-off landing. The characteristic result for this configuration is its decreasing effectiveness at high angles of attack and change of sign of the  $c_{n\delta r}$  derivative at approximately 12.5 deg angle of attack for the basic

design of all-flying tailplanes. This reverse action of the control surfaces is of course unacceptable. The cause of this phenomenon is flow separation developing at the surface with higher deflection. This is explained in detail in Figures 10 and 11.

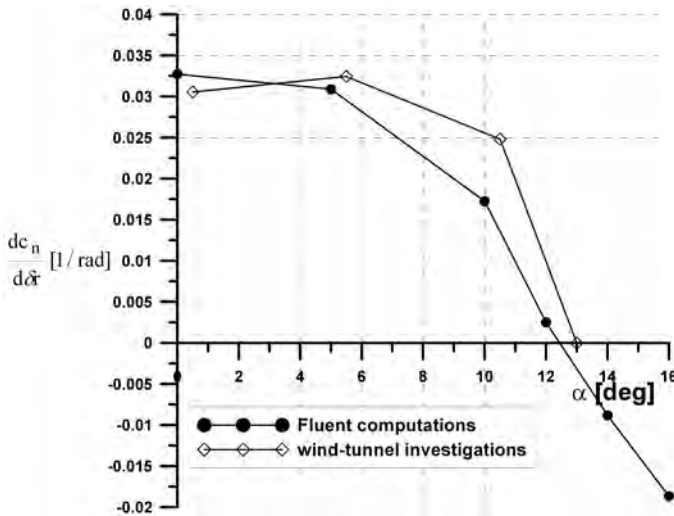


Figure 9. Change of  $c_{n\delta r}$  derivative with angle of attack for all-moving control surfaces

Presented in Figure 10 is the side-force derivative with respect to the rudder deflection  $\frac{\partial c_y}{\partial \delta r}$  versus fuselage angle of attack. Along the curve for the total value (sum over the left and right element) shown are separate curves for the right and left element. The reason for the reverse action of tail surfaces may be found by analyzing the curves for individual elements. The derivative was determined assuming positive deflection of the right element (increasing its angle of attack) and negative deflection of the left element (decreasing its angle of attack).

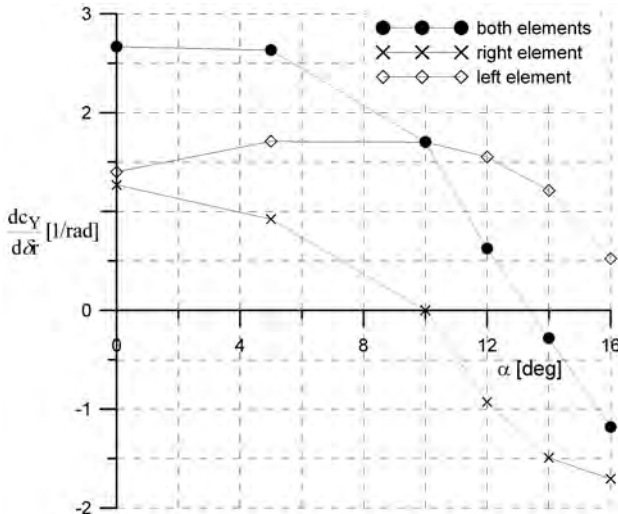


Figure 10. Change of  $c_{y\delta r}$  derivative with angle of attack for complete all-flying surface tail unit and for each element separately

The value of the  $c_{y\delta_r}$  derivative for the right element reaches 0 at approximately  $\alpha=10^\circ$  and becomes negative, while for the left element remains positive. This is explained by the developing flow separation on the right tail surface at angle of attack above  $10^\circ$  (Figure 11). Increasing the angle of attack on the right element above  $\alpha_{crit}$  leads to decreasing of the lift force and the side force on this element. The decrease of lift on the right element, due to flow separation is higher in magnitude than the decrease of lift on left element where the angle of attack was lowered. As a result, the total force changes direction from right to left. The change of the yawing moment is then from positive to negative, as the yawing moment is generated by the side force on the tail surfaces.

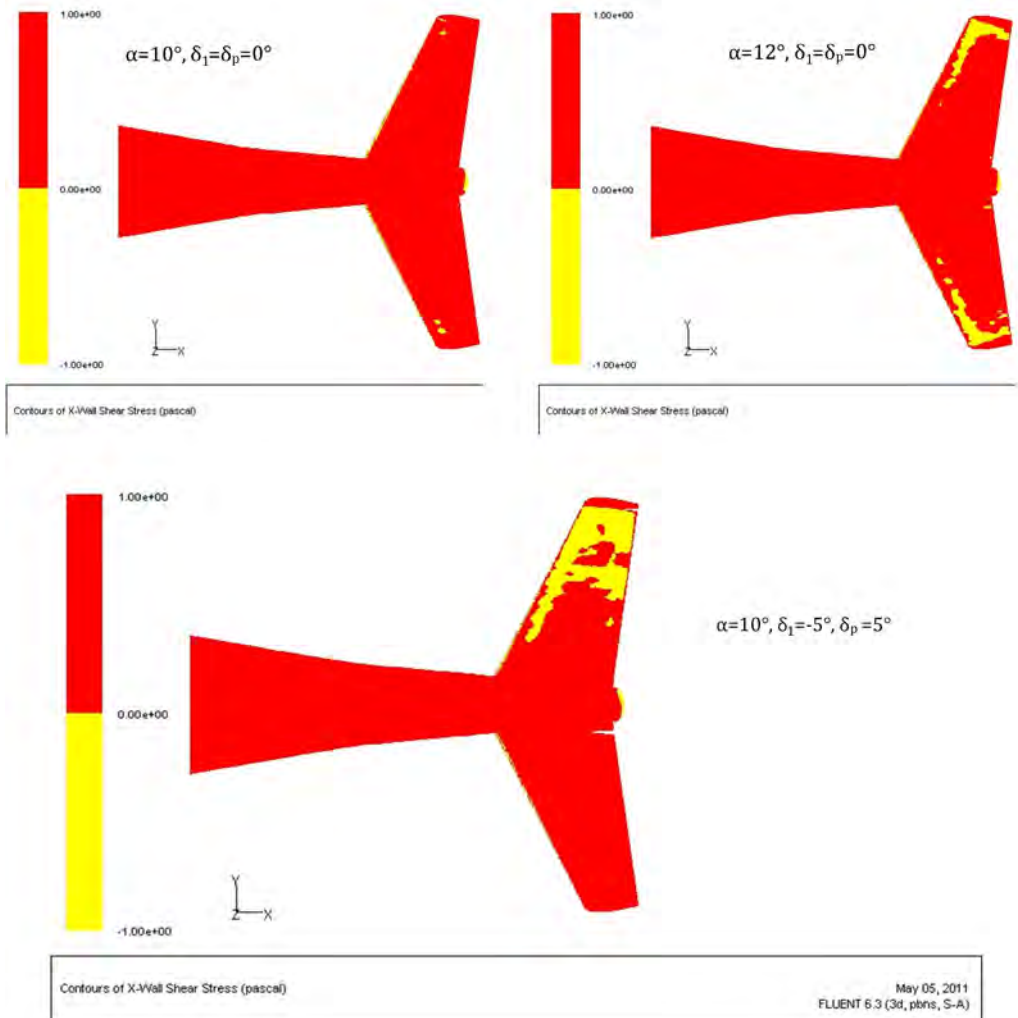


Figure 11. Contours of wall shear stress coefficient in x-direction for the all-moving tail surface configuration. Color maps with two values in order to display the extent of the separated area (positive x-shear stress - red color – area of attached flow, negative x-shear stress - yellow color – area of separation)

Computations of the effectiveness of tail surfaces at high fuselage angles of attack were performed also for the split tailplanes with 70% chord rudder. The results of the computations are presented in Figures 12 and 13. The results show an improvement of the effectiveness of the control surfaces in a sense that the reverse action occurring for all moving variant is eliminated. The value of the  $c_{n\delta r}$  derivative, however, still decreases significantly for fuselage angle of attack higher than  $\alpha=10^\circ$ .

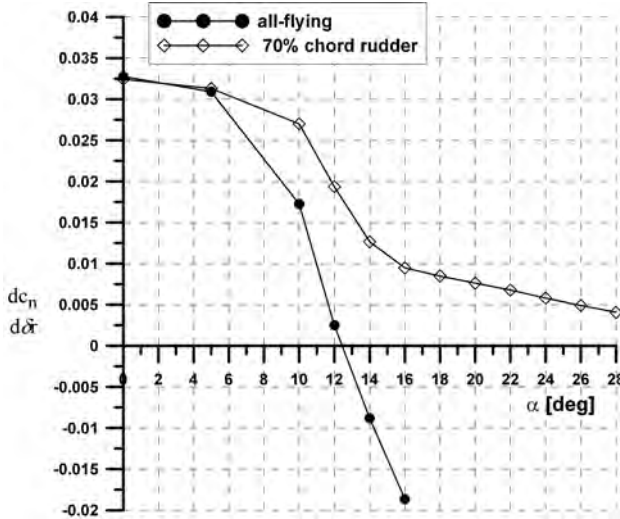


Figure 12. Comparison of the derivative of yawing moment with respect to rudder deflection for a gyroplane with all-moving, single-element tailpanes and stabilizer-rudder configuration

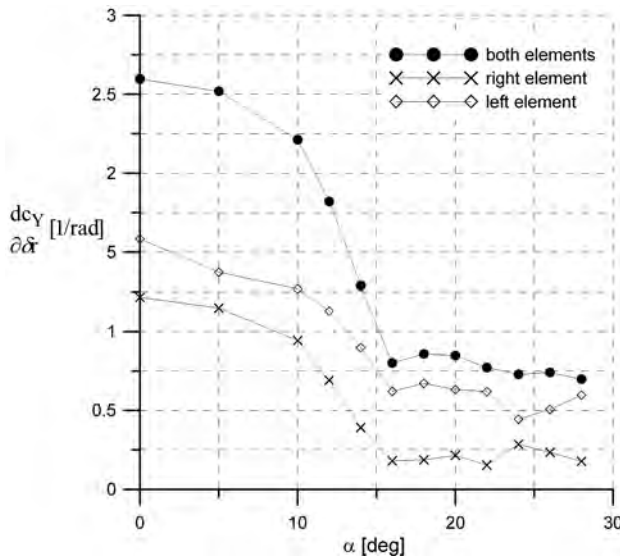


Figure 13. Change of  $c_{Y\delta r}$  derivative with angle of attack for complete tail unit and for each element of the elevator-rudder configuration separately

The change of derivative of side-force coefficient with angle of attack for the split tailplanes, including data for the left and right element separately is shown in Figure 13. In this case the derivative remains positive on both elements. The distribution of X-wall shear stress on both el-

ements for the case with deflected rudders is shown in Figure 14. It can be seen, that with increasing the fuselage angle of attack separation develops on both elements. This explains the drop of effectiveness of the tail unit at fuselage angles of attack over  $10^\circ$  and also indicates that both elements, left and right, are working in similar conditions. It can be seen also, that grater increase of side force occurs on the left element with rudder deflected negative towards the flow (decreasing local angle of attack).

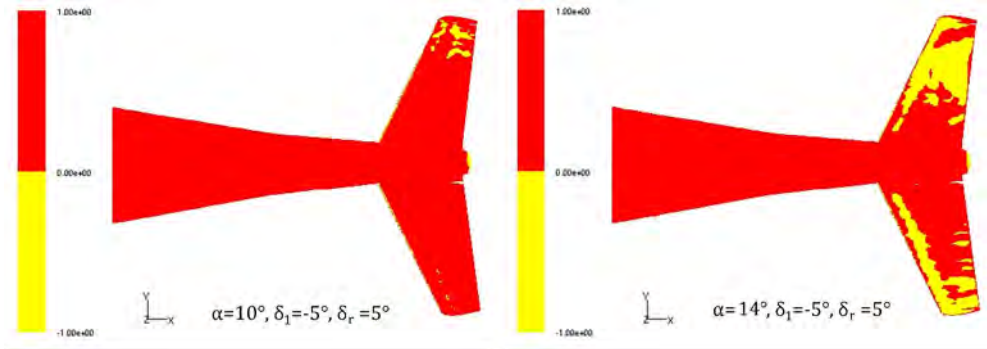


Figure 14. Contours of wall shear stress coefficient in x-direction for the elevator-rudder tail surface configuration

Contributions of each tail component part (fixed and moving) to the value of the derivative at fuselage angle of attack  $\alpha=5^\circ$  and  $14^\circ$  are shown in Table 3. It can be seen, that in the presence of flow separation more effective are elements for which deflection of the rudder decreases local angle of attack (left stabilizer and rudder are both producing increase of side force), and on the right side, with increasing local angle of attack, increase of side force is generated mainly on the rudder. At lower fuselage angle of attack the contributions of the left and right elements are more balanced.

Table 3. Contributions of elements of the split tailplane configuration to the derivative of side-force due to rudder deflection

fuselage angle of attack	$\frac{\partial c_Y}{\partial \delta_r}$ total	left elevator + left rudder	left elevator	left rudder	right elevator + right rudder	right elevator	right rudder
5	2.5193	1.3713	0.7877	0.5836	1.1480	0.7517	0.3963
14	1.2889	0.8978	0.4133	0.4845	0.3911	0.0617	0.3294

## CONCLUSIONS

- The original solution of all-flying tailpanes is effective only within a limited range of the fuselage angle of attack, above which acts in a reverse way, due to extensive flow separation on the element at higher local angle of attack,
- The split version of the tail surfaces is safer than the all-flying version (no reverse action), however its effectiveness also decreases rapidly above  $\alpha=15^\circ$ ,
- Effectiveness of tailpanes at high angles of attack may be improved by changing inclination angle for manouvers at low speed, high fuselage angle of attack, such as power-off landing approach. This option is safer with the split version (stabilizer, rudder) because of the danger of reverse action of the all-flying version.

## REFERENCES

- [1] Fluent 6.3 User's Guide, Ansys.Inc.
- [2] Menter, F. R. (1993), "Zonal Two Equation  $k-\omega$  Turbulence Models for Aerodynamic Flows", AIAA Paper 93-2906.
- [3] Roskam J "Airplane Flight Dynamics and Automatic Flight Controls", DARCorporation, Lawrence, Kansas 6604, USA, 1995.
- [4] Stalewski W., Zalewski W. „Analysis of aerodynamic properties of the lifting rotor and the range of attainable load factors in operational conditions of a gyroplane”, Report of Institute of Aviation nr R13003\_BA2-038/11 (in Polish), 2011.

JANUSZ SZNAJDER

## **SKUTECZNOŚĆ USTERZENIA WIATRAKOWCA W KSZTAŁCIE ODWRÓCONEGO "V" PRZY MAŁEJ PRĘDKOŚCI I NA DUŻYCH KĄTACH NATARCIA**

### Streszczenie

*Usterzenie w układzie „V” posiada pewne zalety wobec usterzenia klasycznego, polegające głównie na prostszej konstrukcji struktury i niższych kosztach wytwarzania, przy nieco bardziej skomplikowanym mechanizmie sterowania. Z podobnych powodów ten układ jest również atrakcyjny w projektowaniu wiatrakowców. Jednak rozważając ten układ usterzenia w projekcie wiatrakowca należy uwzględnić niektóre specyficzne czynniki dla mechaniki lotu tego typu statków powietrznych. Jednym z nich są wahania łopat wirnika, stąd bezpieczniejszym rozwiązaniem dla wiatrakowca jest układ odwróconego „V”. Innym czynnikiem który należy brać pod uwagę jest zakres kątów natarcia kadłuba dla którego usterzenie musi pracować skutecznie. Jest to istotne szczególnie dla sterowania kątem odchylenia. Sterowność kierunkowa powinna być zapewniona dla warunków stromego podejścia do lądowania bez napędu przy kątach natarcia przekraczających  $20^\circ$  i dla warunków lądowania na niewielkiej powierzchni z wyhamowaniem prędkości postępowej przez wychylenie głowicy wirnika w tył. W pracy badano przy pomocy numerycznych symulacji opływu skuteczność dwóch alternatywnych wariantów usterzenia w układzie odwróconego „V”. Analizę przeprowadzono dla opływu dwu- i trójwymiarowego. Jednym z rozwiązań było usterzenie płytowe a drugim usterzenie dzielone na statecznik i ster mające ten sam obrys co usterzenie płytowe. W obliczeniach opływu dwuwymiarowego wykazano że dla usterzenia dzielonego o cięciwie steru równej 60-70% cięciwy profilu w warunkach startu i lądowania maksymalna wartość siły nośnej jest wyższa niż dla usterzenia płytowego przy wartości pochodnej współczynnika siły nośnej względem kąta wychylenia steru tylko o 10% mniejszej od usterzenia płytowego. W obliczeniach opływu trójwymiarowego wykazano, że układ odwróconego usterzenia „V” pracuje skutecznie tylko w ograniczonym zakresie kątów natarcia, w przybliżeniu  $\pm 10-15^\circ$ . Poza tym zakresem jego skuteczność raptownie spada, szczególnie w przypadku usterzenia płytowego. Dla tej konfiguracji pochodna współczynnika momentu odchylającego względem kąta wychylenia steru zmienia znak dla kątów natarcia kadłuba przekraczających  $12^\circ$  z powodu rozległego oderwania opływu na elemencie usterzenia zwiększającym kąt natarcia. Usterzenie dzielone nie wykazuje odwrotnego działania, jednak jego skuteczność również szybko spada na dużych kątach natarcia. Proponowanym rozwiązaniem jest wprowadzenie mechanizmu przestawiania kąta zaklinowania usterzenia dla manewrów przeprowadzanych na dużych kątach natarcia kadłuba, np. dla stromego podejścia do lądowania bez napędu. Rozwiązanie to jest bezpieczniejsze w zastosowaniu z usterzeniem dzielonym z powodu braku odwrotnego działania które mogłoby wystąpić w przypadku usterzenia płytowego.*